Development of a photovoltaic power prediction system for forecast horizons of several hours

Von der Fakultät für Mathematik und Naturwissenschaften
der Carl von Ossietzky Universität Oldenburg
zur Erlangung des Grades und Titels eines
Doktors der Naturwissenschaften (Dr. rer. nat.)
angenommene

Dissertation

von Herrn Jan Kühnert
geboren am 25.09.1983 in Bochum

Erstgutachter:	Prof. Dr. Jürgen Parisi
Zweitgutachter:	Prof. Dr. Ulrike Feudel

Tag der Disputation:	19. Januar 2016

Diese Arbeit wurde durch das Stipendienprogramm der Deutschen Bundesstiftung Umwelt (DBU) gefördert.

Kurzfassung

Vorhersagen der Einspeisung aus Photovoltaik-Anlagen (PV) sind von fundamentaler Bedeutung für die Steuerung von Stromnetzen mit hohen PV-Anteilen. Die Entwicklung und Verbesserung von regionalen Kurzzeit-Vorhersagen für die Anwendung am Energiemarkt sind Ziel dieser Arbeit. Vorhersagen für Horizonte von bis zu 5 Stunden im Voraus für Deutschland und die Regelzonen der Übertragungsnetzbetreiber stehen dabei im Mittelpunkt. In dieser Arbeit werden umfangreiche Datensätze aus gemessener PV-Leistung und meteorologischen Parametern wie Einstrahlung und Temperatur genutzt. Es werden darauf aufbauend robuste und transferierbare Ergebnisse präsentiert, die ein durchgängiges Verständnis der beteiligten Prozesse ermöglichen. Regionale Vorhersagen basieren auf Vorhersagen der Globalhorizontalstrahlung an den Standorten von einzelnen PV-Anlagen. Diese Strahlungsvorhersagen werden aus bereits etablierten numerischen Wetterprognosen (NWP) gewonnen und durch ein Satelliten-basiertes Verfahren ergänzt. Dieses Verfahren nutzt Satellitenbilder im sichtbaren Spektralbereich zur Erkennung und Vorhersage der Wolkenbewegung mit Hilfe von Wolkenzugsvektoren (cloud motion vectors, CMV). Ein Schwerpunkt dieser Arbeit ist die Bewertung des Potentials und die Weiterentwicklung dieser Satelliten-basierten Methode. Die Anwendung eines physikalischen Ansatzes zur PV-Leistungsmodellierung und ein Hochrechnungsverfahren (Upscaling) ermöglichen die Ableitung von regionalen PV-Leistungsvorhersagen aus Strahlungsvorhersagen. Eine detaillierte Analyse der beteiligten Modelle, der genutzten Eingangsdaten und deren Auswirkung auf regionale Vorhersagen wird im Rahmen dieser Arbeit durchgeführt. Die Berechnung von regionalen Prognosen erfolgt auf Basis einzelner repräsentativer Anlagen unter Berücksichtigung der räumlichen Verteilung unterschiedlich dimensionierter PV-Anlagen in Deutschland. Die so erstellten regionalen PV-Leistungsvorhersagen auf Basis von NWP- und CMV-Strahlungsvorhersagen werden mit regionalen Hochrechnungen der eingespeisten PV-Leistung auf Basis hoch aufgelöster aktueller Messungen einer Vielzahl überwachter Anlagen kombiniert. Das in dieser Arbeit entwickelte Verfahren zur Kombination und die damit verbundende Integration der CMV- und Messwert-basierten Vorhersagen tragen zu einer deutlichen Steigerung der Vorhersagegenauigkeit bei. Für zwei Stunden im Voraus wird dadurch eine Reduzierung des Vorhersagefehlers um über 50% *zu entsprechenden Vorhersagen rein aus NWP-Modellen erreicht.*

Abstract

Forecasts of photovoltaic (PV) power feed-in are essential for energy supply systems with a high penetration of PV power. In this thesis, the focus is on short-term regional PV power forecasts for the application at the German energy market. This comprises forecasts for a few hours ahead for Germany and the control areas of the German Transmission System Operators. Throughout this thesis large datasets of measured PV power and meteorological parameters such as irradiance and temperature are used, leading to high robustness and transferability of the findings presented. Regional PV power forecasts here are based on predictions of global horizontal irradiance at specific sites. Irradiance forecasts are derived from established numerical weather prediction (NWP) models and a newly integrated satellite-based forecasting approach using cloud motion vectors (CMV). A further analysis and development of this CMV approach is one subject of this thesis. In a next step, an irradiance-to-power conversion model and an upscaling approach are applied to derive regional PV power forecasts. PV power is modeled using explicit physical modeling followed by a statistical post-processing on historical data. An in-depth analysis of all processes involved in PV power modeling is performed with respect to models applied, input data used and with respect to their impact on the overall forecast accuracy. Regional forecasts are derived by applying an upscaling approach based on single representative sites, considering the spatial distribution of differently sized PV power plants in Germany. PV power forecasts based on NWP irradiance forecasts are combined with CMV-based forecasts and with online measured PV power from a large dataset of single sites monitored. Short-term forecasts significantly improve by including satellite information and online measured PV power with the combination approach developed in this thesis: For two hours ahead-forecasts, the error of regional forecasts for Germany is reduced by over fifty percent compared to NWP forecasts.

Contents

Glossary

VRE	variable renewable energy sources (solar and wind)
PV	photovoltaic
TSO	transmission system operator
NWP	numerical weather predictions
ECMWF	European Centre for Medium Range Weather Forecasts
DWD	German Weather Service (Deutscher Wetterdienst)
CMV	cloud motion vector
RES / EEG	renewable energy sources act / Erneuerbare Energien Gesetz
CI	cloud index image
MSG	Meteosat second generation satellites
I	global horizontal irradiance $[W/m^2]$
I_d	diffuse horizontal irradiance $[W/m^2]$
I_b	beam/direct irradiance $[W/m^2]$
I_{POA}	tilted irradiance/irradiance on plane-of-array (POA)$[W/m^2]$
$I_{POA,d}$	diffuse irradiance on plane-of-array (POA)$[W/m^2]$
$I_{POA,b}$	beam/direct irradiance on plane-of-array (POA)$[W/m^2]$
$I_{POA,g}$	ground reflected irradiance on plane-of-array (POA)$[W/m^2]$
I_{ext}	extraterrestrial irradiance $[W/m^2]$
I_0	solar constant $I_0 = 1367W/m^2$
n	cloud index
k^*, k^*_{PV}	clear sky index for irradiance / PV
k	clearness index
ρ	reflectivity / surface albedo
P	PV power $[W]$
P_{inst}	installed PV capacity $[W]$
P^{lr}	PV power with linear regression applied $[W]$
P_{scale}	regional PV power by upscaling approach $[W]$
I_{meas}, P_{meas}	measured irradiance/PV power
I_{clear}, P_{clear}	clear sky irradiance/PV power
I_{sat}, P_{sat}	satellite-based irradiance/PV power
I_{CMV}, P_{CMV}	irradiance/PV power forecast from cloud motion vectors (CMV)
I_{NWP}, P_{NWP}	irradiance/PV power from numerical weather predictions (NWP)
I_{pers}, P_{pers}	irradiance/PV power from persistence forecasts
T	temperature $[°C]$
T_a	ambient temperature $[°C]$
T_m	PV modules' temperature $[°C]$
β	tilt/plane-of-array (POA) angle of PV modules $[°]$
ϕ	azimuth angle $[°]$
Θ	angle of incidence $[°]$
θ_z	solar zenith angle $[°]$
h	sun elevation $[°]$
φ	latitude $[°]$
λ	longitude $[°]$

1. Introduction

With a substantial share of solar and wind power feed-in in an energy supply system, the fluctuating power production increases the complexity of grid operation. These variable renewable energy sources (VRE) show fundamentally different characteristics of power generation than conventional power plants. Conventional power plants based on e.g. fossil fuels are widely adaptable to the actual power need, whereas VRE power generation contributes a strong weather dependent component: The temporal and spatial availability of solar and wind power generation is determined by the weather conditions. Consequently, forecasts of solar and wind power are an integral and invaluable part of grid operation and management.

The electricity supply system in Germany is a prime example of a system with a high penetration of VRE. By the end of 2014, 38.5 GW of photovoltaic (PV) and around 39 GW of onshore and offshore wind power capacities were installed, contributing around 18% of the nationwide annual power consumption in 2014. VRE power generation is strongly decentralized with over 1.5 million PV power plants and 25.000 wind power generators, with a high share of solar in southern and eastern parts of the country and of wind in the northern parts [1, 2]. The current legislation aims at a preferential treatment of solar and wind power with respect to the feed-in priority and provides incentives for the extension of renewable energy capacities. The integration of VRE power leads to the development of new approaches or the adaptation of existing methods for balancing energy supply and demand, aiming at different levels within the energy supply system: Market-based balancing of power supply and demand enables an adaption of power generation to available resources; shifting loads to periods with high availability of VRE power by so-called demand-side-management systems leads to an efficient use of available power; decentralized and flexible storage capacities are capable of compensating for temporal fluctuations of power feed-in.

A main instrument for balancing energy supply and demand are electricity markets: Here, electricity contingents are traded prioritizing renewable energy sources. For this, forecasts of available and required power are essential. These forecasts of power feed-in are required for the 'day-ahead' and the 'intraday' market: First allocation of expected power feed-in is done on the day-ahead market, updates of feed-in forecasts can be placed on the intraday market up to 45 minutes before delivery. Different market participants use power forecasts: Transmission System Operators (TSOs) are responsible for the prioritized feed-in of renewable energy contingents and use forecasts for their control area and nationwide. With current revisions of the legal basis, direct marketing for single or virtually aggregated power plants is getting more and more important, requiring localized forecasts of power feed-in. Similar structures and regulations also exist in other countries, but here the focus is on the situation in Germany.

Costs of the energy supply system rise with inaccuracies of power forecasts, as predicted power contingents determine pricing at the day-ahead and intraday markets [3]. Remaining discrepancies between traded electricity and actual physical supply and demand can only be compensated by the costly use of balancing energy. Improvements of forecast quality contribute to reduce the need for control energy and hereby the costs for the energy supply system [4]. Besides, in hard-to-predict situations, forecast uncertainties can get as high as the amount of available balancing energy, potentially affecting the grid's stability [5, 6]. The development of forecasting methods thus has to address the reduction of overall uncertainty, but also focuses on events of exceptional high forecast uncertainties.

Wind power forecasting has been established in energy market operations for a number of years, see e.g. [7]. Forecasting of photovoltaic (PV) power feed-in has undergone a rapid development in recent years, due to the significant increase in PV power capacities and thus an increased demand for forecasting. In this thesis, PV power forecasts for energy market application are addressed. PV power feed-in is directly dependent on solar irradiance, follows distinct diurnal and annual variations, and is subject to strong weather dependent fluctuations. Temporarily, the share of PV in overall net load in Germany can reach up to 35% on sunny weekdays or even 50% on weekend days [1]. In single control areas, shares of even 100% and above were observed on rare occasions [5].

PV power forecasting approaches are based on predictions of solar irradiance. Various approaches for solar irradiance forecasting exist, addressing different spatial and temporal scales. For an overview on state-of-the-art solar power forecasting, see e.g. [8, 9]. Numerical weather prediction models (NWP) are well established and available in different spatial and temporal resolutions. For short-term forecast horizons satellite-based approaches have been recently investigated [10, 11, 12]. Other short-term forecasting methods are based on in-situ irradiance measurements from pyranometers or ground-based sky imagers [13]. Research on PV power forecasting is so far less present in the literature than irradiance forecasting and often based on evaluations for a few sites or single systems only. PV power output simulation is usually done using explicit physical modeling or statistical methods or a combination of both [8]. In explicit physical approaches, the PV power is simulated taking irradiance and temperature forecasts as well as system-specific information into account [14]. This includes the conversion of global horizontal irradiance to irradiance on the tilted modules' plane and PV efficiency models [15, 16]. Statistical methods utilize historic PV power measurements, modeling the power feed-in according to global horizontal irradiance forecasts or other auxiliary data, see e.g. [17, 18]. Other forecasting approaches are based on measurements from close-by PV sites [19]. To obtain regional forecasts, approaches to derive regional feed-in based on site specific power forecasts exist [20].

This thesis aims at the improvement of forecast accuracy for regional short-term PV power forecasts. 'Regional' refers to the control areas of the German TSOs and all of Germany, 'short-term' to forecast horizons of up to five hours ahead. All steps in forecast processing are addressed: From solar surface irradiance and temperature forecasts via a PV power simulation model through to an upscaling algorithm to derive regional power feed-in forecasts. By this, new approaches for PV power forecasting are found, the accuracy of existing methods is increased, and a better understanding of the processes involved is achieved. In contrast to existing studies, a large amount of distributed sites are considered and methods adapted accordingly: The dataset used contains over 1000 PV sites, distributed across Germany and received from the monitoring database of *meteocontrol GmbH*. These PV power measurements in 15-minute intervals allow for a precise assessment of forecast accuracy and the impact of models developed. They are complemented by meteorological measurements of irradiance and temperature.

Research presented in this thesis is based on an existing and operational PV power forecasting system, operated by the University of Oldenburg and *meteocontrol GmbH* [21]. This system utilizes model output statistics (MOS) for solar irradiance forecasts, based on NWP models by different forecast providers as well as satellite information and ground-based irradiance measurements. PV power modeling is done by explicit physical modeling and regional forecasts are derived using an upscaling approach [20, 22, 23]. According to these components, following aspects are highlighted in this thesis:

- Irradiance forecast accuracy of a satellite-based forecasting approach using cloud motion vectors (CMV) is addressed and compared to established numerical weather prediction (NWP) models in a first step. Potential and limitations of this satellite-based approach are assessed and further developments initiated.
- PV power simulation for PV power sites with limited knowledge of individual system parameters is performed in a second step with focus on the application in regional forecasting. An in-depth analysis of the datasets and model components used in power modeling is provided and strategies are developed to handle a large amount of PV systems.
- PV power forecasts based on satellite data and NWP models are enhanced by predictions based on online measured PV power. These measurements allow for a better description of the actual systems' state and are integrated by an approach combining individual forecasting methods.
- Regional forecasts are focused on in accordance to the requirements of the German energy market and to information on the energy system available. An upscaling approach is introduced with an optimized description of the PV sites' distribution.

This thesis is organized as following. In chapter 2 background information on requirements for PV power forecasting systems is provided, focusing on the integration of VRE in the electricity supply system by market mechanisms. The forecasting systems' design analyzed in this thesis is introduced and metrics for forecast accuracy assessment are given. In chapter 3, a satellite-based approach for short-term irradiance forecasting, using cloud motion vectors (CMV), is introduced. A comprehensive evaluation of two years' CMV forecasts compared to NWP forecasts is provided and improvements of the CMV method are addressed. The PV power modeling for application in forecasting is addressed in chapter 4. Models and parameters for the conversion from global horizontal to plane-of-array irradiance and for conversion to PV power are described and rated with respect to their impact on the overall forecast accuracy. An evaluation of PV power forecasts for a one-year dataset is given. In chapter 5, forecasts based on NWP models, CMVs and measured PV are combined for an optimized PV power forecasting on short-term scales. The upscaling algorithm for regional forecasts is addressed in chapter 6. Here, the best configuration for projecting regional forecasts from single-site forecasts is discussed and applied to a one year dataset of measured and predicted PV power. A summary of the results obtained in this thesis is given in chapter 7 and discussed conclusively. Results and passages which are already published elsewhere in context of the thesis are denoted accordingly in the corresponding sections.

2. Background

This thesis addresses the complete processing chain of PV power forecasting, from irradiance forecasts via PV power simulation through to upscaling to regional forecasts. This chapter provides background information on the framework of PV power forecasting. First, in section 2.1 an introduction to the energy market design and requirements for the PV power forecasting system is given. In section 2.2, the characteristics of PV power feed-in and the design of the PV power forecasting system is presented. Metrics and terminology when dealing with forecast accuracy assessment are displayed in section 2.3. Further background information on the models used throughout the thesis are provided more detailed in the introductory sections of the corresponding chapters.

2.1. Forecast requirements for the German Energy Market

In this section, an overview on the energy market mechanisms and the resulting requirements for forecasts of electricity production by VRE sources is given. As an instrument for balancing electricity production and consumption in Germany and Europe, markets for energy and control reserve are established. The description given here is focused on the German energy market, but similar market structures exist e.g. in Europe and the US [24]. An overview of the market mechanisms is given in fig. 2.1.

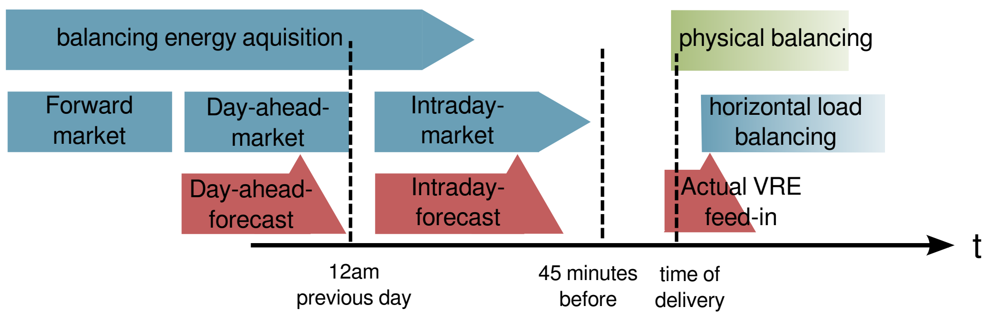

Figure 2.1.: Overview on the process of energy marketing and the resulting need for VRE power production forecasts and assessment with respect to the time horizons relative to the delivery time. Blue fields show the energy market related processes, power forecasting and assessment utilized is displayed in red; based on [25].

2.1.1. Energy market design and participants

Electricity trading is basically organized in three submarkets (see blue fields in fig. 2.1): On the **forward market** (dt. 'Terminmarkt') at the European Energy Exchange [26], energy deliveries are traded for months up to several years in advance. The spot market, for Germany at the European Energy Exchange EPEX SPOT [27], houses the markets focusing on much shorter time spans: On the **day-ahead market** electricity offerings and bids in hourly contingents for the next day are placed, closing trades at 12 am. By this, a first allocation of available and required electricity contingents is carried out based on estimations of feed-in and consumption. Updates of these first allocations are then possible on the **intraday market**, starting three hours after the closure of the day-ahead market and ending on the settlement day, 45 minutes before electricity delivery in 15 minutes contingents. On the intraday market, being much closer to the time of delivery, these updates allow for a much better estimation of real feed-in and consumption. [24, 25, 28]

This organization of the electricity market aims at a high cost-efficiency when balancing demand and supply. Generation units with lowest variable costs are first placed to satisfy demand, followed in order of increasing costs ('merit-order'). For the VRE sources, these costs are lowest as no fuel costs are considered. Consequently, wind and solar power are placed first in the 'merit-order', followed by nuclear power plants, lignite and hard coal powered plants [25]. The resulting cost of the electricity is usually based on the cost of power plants in use with the highest variable cost ('marginal cost price'). The marginal cost price is usually specified by the expected power feed-in and demand at the day-ahead market [29]. Thus, an expected high power production by VRE can lead to a significant reduction in power generation costs ('merit-order effect'), as plants with high variable costs are banished and the marginal cost price reduces [30, 31]. The prices at the intraday market are highly dependent on these day-ahead market prices but respond to the updates of expected power feed-in and consumption [29].

The market participants at the Energy Exchange are utility and supply companies, transmission system operators (TSOs) and direct marketers of power generation units, but also energy intensive industries [27]. One focus in this study is on TSOs, being responsible for the integration of renewable energy sources and grid balancing. Transmission System Operators in Germany currently are 50hertz, Tennet TSO, Amprion and TransnetBW (see fig. 2.2)[32].

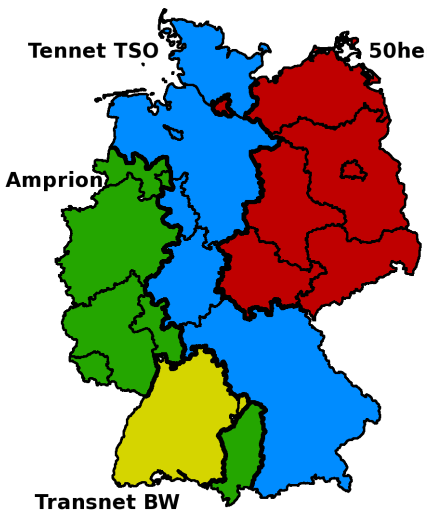

Figure 2.2.: Transmission system operators (TSOs) and their control areas in Germany.

The TSOs are obliged to purchase all electricity produced by RE source produced in their control area from plant operators or distribution network operator, in accordance to the regulations defined by the RES act [33]. These electricity contingents have to be sold at the EPEX by the TSOs, normally earning lower revenues than they were paid to the plant operators regulated by the feed-in tariffs of the RES acht. Financial losses are compensated for through the so called RES apportionment ('EEG-Umlage'). A central process here is the equalization of the burden of this process among the TSOs by the horizontal load balancing ('Horizontaler Belastungsausgleich'). VRE feed-in is pooled by all TSOs for Germany: TSOs with a comparatively high penetration of VRE in their control area are compensated by TSOs with below average penetration. The compensation is proportional with respect to the load consumption for each individual TSO and is based on the estimation on the actual power feed-in (see fig. 2.1). [33, 34, 35]

Another focus is on direct marketers. These typically are single or affiliated power generation unit operators who participate at the energy market without involvement of the TSOs. Direct marketers then act self-responsible at the energy market [36]. Based on new regulations of the RES act from 2014, all operators of newly established power generation facilities with nominal power over 500 kWp (from 2016 over 100 kWp) are obliged to act as direct marketer [33, 37].

2.1.2. Balancing energy

As the energy market balancing is done based on forecasts of supply and demand, care has to be taken that the physical generation and consumption is matched temporally and spatially. Reasons for differences in market-based and physical balancing are based on uncertainties in i) wind and solar power forecasts and in ii) forecasts of electricity demand as well as on iii) unforeseen power plant shutdowns. To compensate for these deviations in assigned and actual power generation and consumption, fast-dispatchable control energy contingents have to be available at any time. Control energy has to be able to compensate for both, surplus and shortages of electricity ('negative' and 'positive control energy') [24, 38, 39, 40]

Physical balancing is done on different temporal scales by i) primary control reserve, ii) secondary control reserve to and iii) minute reserve or tertiary control reserve (see green fields in fig. 2.1). These groups are differentiated by the time of activation (from 30 seconds for primary control reserve to several minutes for secondary and minute reserve) and by the time span of control power usage (maximum 15 minutes for primary and up to one hour for minute reserve) [25, 41]. For control reserve, fast-reacting systems are especially suitable, as gas turbine plants or pumped storage hydro power stations, but also thermal power plants (e.g. coal power plants) as 'spinning reserve' for primary control reserve. Up to today wind or solar power are only suitable as negative control reserve by curtailment of power generation capacities [42]. In future energy grid design, decentralized storage facilities are also expected to act as valuable provider of control energy [43].

In addition to the energy markets for electricity balancing, the control energy market is also an important instrument for grid operation. Providers of control energy are compensated for holding capacities available and with an additional allowance for actually providing the control energy when needed. Both prices for holding capacities and actually providing control energy are subject to partially high fluctuations in market prices and usually are significantly higher than the energy prices at the day-ahead or intraday markets [24, 31, 44]. By June 2015, around 4.8 GW of positive control reserve (sum of secondary and tertiary) and 4.1 GW of negative control reserve are tendered, as published on the joint portal for control reserve statistics by the TSOs [45]. For special situations, available control reserve is adapted to the expected needs. This for example was done for the solar eclipse in March 2015 [46], with overall 8.0 GW positive and 7.3 GW negative control reserve, due to uncertainties of PV power feed-in. Increased balancing energy capacities also are tendered for christmas days on a regular basis, with e.g. up to 25% balancing reserves in 2014 [45], due to uncertainties in load forecasts.

In the long run, capacities of control energy have to be dimensioned including consideration of VRE expansion and expected accuracies of feed-in and load forecasts. According Hirth and Ziegenhagen (2013) each GW of VRE added leads to a 30-70 MW increase in demand for control energy, depending among other things on the quality of power feed-in forecasts [4]. However, despite the significant increase in VRE capacities, the trend shows an actual decline in control energy capacities of 20% from 2008 to 2012, mainly due to reorganization of the control energy market but also to increased forecast quality. As the beneficial effect of reorganization is limited, improvement of forecast quality significantly influences the need for control energy and thus the costs for the energy supply system [**deutsche˙energieagenture˙dena˙dena˙2010**, 4]. Quality of intraday forecasts of VRE power feed-in thus has a direct impact on the need for control energy and the cost of the energy supply system with a high share of VRE [47].

2.1.3. Prediction and assessment of VRE power feed-in

Fitting into the market design presented in the previous section, forecasts of power feed-in from RE contribute to a cost-efficient and reliable energy supply. The demand for PV power forecasting and assessment is oriented at the market requirements (see red fields in fig. 2.1):

- **Day-ahead forecasts** are most important for a first allocation of available wind or solar power resources for the day-ahead market. These forecasts are especially relevant for defining the marginal cost price (see section above) and thus the pricing of electricity at the spot market. The accuracies of day-ahead forecasts essentially determine the costs of electricity at the energy exchange [29, 48].
- **Intraday forecasts** are used to update the day-ahead trades according to the newest forecast available. This enables a much better estimation of power feed-in because forecasts improve with reduced forecast lead time. These forecasts are especially relevant for balancing supply and demand: Remaining forecast errors can only be compensated for by the use of control energy, leading to high costs of the energy supply system [24, 48]. For the interaction of intraday market and control reserves, forecast lead times of few (usually two) hours ahead before delivery are especially important: This is a consequence of i) the gate-closure of the intraday market 45 minutes before delivery and ii) the need for additional time reserves for forecast processing and decision making.

- **Regional forecasts** are utilized by TSOs and other participants as utility companies for estimating the feed-in for Germany or for the corresponding area of interest. These forecasts are essential for their participation at the energy exchange. Areas of interest are usually of several hundred kilometers' extent for the control areas of the TSOs, but can also be much smaller as for utility companies.
- **Site specific forecasts** are most relevant to direct marketers participating at the energy exchange. Here, localized forecasts for single plants or small regions of affiliated power generation units are required. This segment gains more and more importance as direct marketing is focused on. Same is valid for operators of demand side management systems or self-consumers including storage management.
- The **temporal resolution** of forecasts according to the energy market demands is 1 hour for the day-ahead market and 15 minutes for the intraday market.
- For the balancing processes and horizontal burden sharing, **estimations of real power feed-in** of the VRE are needed [49]. Due to the limited feed-in metering, procedures to estimate the total power feed-in for a region are applied based on monitored VRE generation units.

These requirements define the environment for power feed-in forecasts. Due to the energy market design, errors in feed-in forecasts significantly influence the costs of electricity. Studies on the impact of forecast errors on energy prices are mainly focusing on wind power forecasts, see e.g. [29, 40, 50, 51], others on PV and wind power forecasts, e.g. [3]. All state a negative impact of forecast errors on energy pricing but to different extents. The importance of high forecast quality can also be seen at events with extraordinary forecast errors: For example due to a hardly predictable event of persistent high fog on several days in April 2013, forecast errors of 8.8 GW for day-ahead occurred: This was leading to the usage of all available control energy contingents available for multiple hours and to a significant increase peak prices on the intraday market [52]. Besides the forecast quality also the assessment of forecast uncertainty is addressed in forecasting, see e.g. [53, 54]. Besides the mentioned requirements, other application areas for PV power forecasting exists, as e.g. regional forecasts for congestion management, or localized forecasts for demand-side or storage-management.

2.2. PV power forecasting

In this section, the PV power forecasting scheme used for research in this thesis is introduced. This PV power forecasting system responds to the requirements of the energy market as introduced in section 2.1.3 above and accounts for the characteristics of PV power feed-in as briefly summarized in the following section 2.2.1.

2.2.1. Characteristics of PV power feed-in

The (regional) feed-in of PV power shows specific deterministic and weather dependent features that have to be represented by PV power forecasting algorithms. Fig. 2.3, left panel, shows typical diurnal PV power feed-in for three days with different feed-in characteristics. On the 16th January and 2nd August 2013, the power feed-in for a typical clear sky day shows underlying deterministic behavior of the PV power feed-in with a maximum at noon, but to very different extents in summer and winter. The annual trend of PV power feed-in is displayed in the right panel of fig. 2.3 with high feed-in in summer months and lower feed-in for winter. Both the diurnal and annual trends are direct consequence of changing solar geometry.

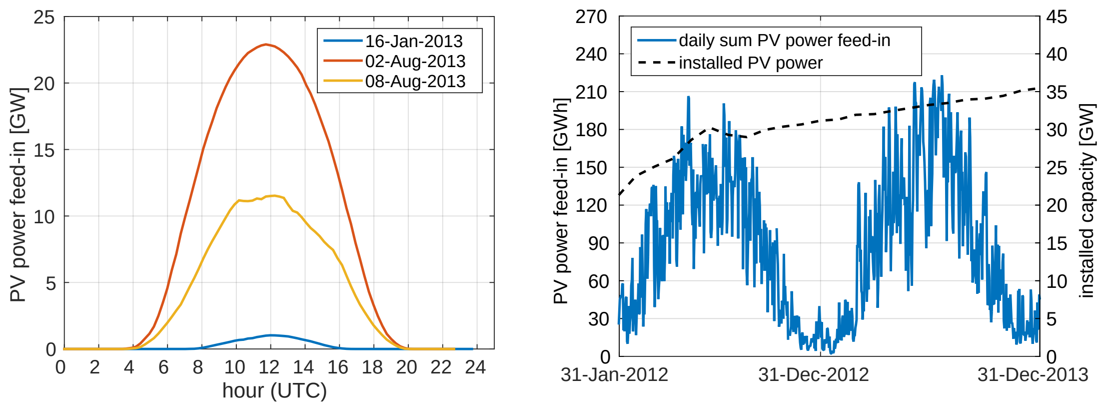

Figure 2.3.: Left: Daily pattern of PV power feed-in for Germany for different feed-in situations. Right: Daily sum of PV power feed-in for Germany for two years (2012 and 2013) and development of installed PV power capacity in Germany. Data sources: RES dataset ([55, 56, 57, 58]) and EEX transparency platform [59].

In addition to these deterministic trends the weather dependency have to be considered and is the biggest challenge in PV power forecasting. A typical day with changing weather conditions is displayed (8th August 2013), showing much lower power feed-in as for the shown clear sky day (left panel in fig. 2.3). Mainly clouds lead to temporal and spatial fluctuations of solar irradiance at the ground. In addition to the impact of solar irradiance, ambient temperature is considered, like heating or cooling of PV power modules leads to a reduction or enhancement of the efficiency of PV power systems. Thus, highest PV power feed-in over the course of a year are typically observed in spring months, with lower average solar irradiance than in summer but also generally lower average ambient temperatures. Considering the overall PV feed-in for a larger region, the overall capacities and characteristics of installed PV power units in this region are important information. Naturally, with installed PV capacities (see right panel in fig. 2.3) as well as the absolute PV power feed-in increases.

2.2.2. PV power forecasting scheme

Research for this thesis is performed in the context of the existing PV power prediction system, operated and developed by the University of Oldenburg and *meteocontrol GmbH*. This section provides an overview on the forecasting scheme and recent and ongoing developments in this context. An outline of the forecasting scheme is displayed in fig. 4.1. Following main steps are involved, details on the applied methods and configuration can be found in the corresponding chapters:

1. Site-specific forecasts of surface global horizontal irradiance are derived, using different data sources, such as numerical weather predictions or satellite data. Recent developments are described e.g. in [23, 60, 61]. The various forecasting approaches applied are introduced and discussed in chapter 3.

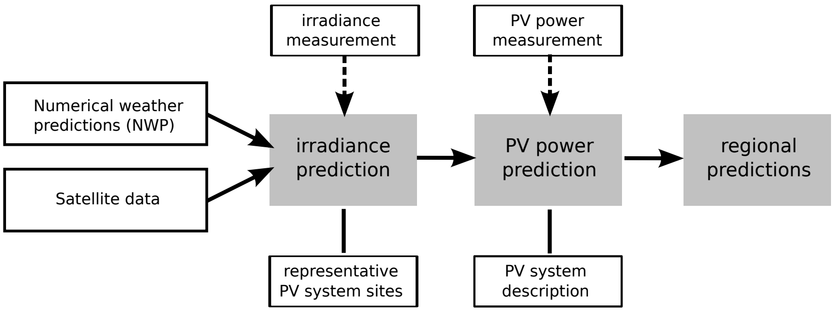

Figure 2.4.: Regional PV power prediction system: Forecasts of global horizontal irradiance are processed via a PV power simulation tool. An upscaling approach derives regional PV power forecasts from site specific PV power forecasts for a representative set of systems; from [60].

2. Based on these irradiance forecasts and additional temperature forecasts, PV power simulation is performed. The approach includes conversion from horizontal irradiance to horizontal direct and diffuse and then to tilted irradiance, taking into account plant specifications such as installed capacity, tilt and orientation. PV power is modeled by applying a parametric PV efficiency model [14, 20, 22]. This PV power simulation algorithm is addressed in chapter 4.
3. The so derived single-site PV power forecasts are used for a regional upscaling algorithm. Here, single-site forecasts for a representative set of PV systems are used to derive the regional PV power feed-in for regions like the control areas or the whole of Germany [14, 20, 22]. Details on the upscaling method are described in chapter 6.

2.3. Evaluation of forecasts

The terminology for evaluating and comparing different forecasts is introduced in the first part of this section. In the following, metrics used for forecast error quantification are presented.

2.3.1. Terminology

The PV power and meteorological forecasts here are evaluated on different spatial levels to emphasize deviating behavior for different applications. Throughout the analysis done in this thesis, different regional classifications are referred to as summarized in the first part of table 2.1. **Single site forecasts** are localized forecasts computed for specific sites individually. These are of high interest for the application in direct marketing of single PV power plants or for demand-side-management systems. For the assessment of forecasts accumulated for differently sized areas, **spatially averaged forecasts** are derived by averaging forecasts for single sites within a specific area. Commonly, in the context of this thesis, spatial averages for all single sites in the dataset are evaluated, representing the area of Germany and referred to as *all sites' averages*. Forecasts derived by the upscaling approach representing the modeled power feed-in for e.g. the control areas or all of Germany are denoted as **regional forecasts**.

Dealing with temporal classification of forecasts, different terms for points or periods of time are relevant (second part of table 2.1). **Forecast valid times** here are points or periods of time the forecasts are valid for. For the energy market application, this denotes the time the power availability has to be scheduled for. At the **delivery time** forecasts are made available to the user; **forecast lead times** or **horizons** describe the time lag between forecast delivery and forecast valid time. **Forecast base time** describes the time a forecast run is initialized, especially relevant for numerical weather predictions: For example, base times of NWP forecasts (see section 3.4) are every six or twelve hours, marking the start of a forecast computation; delivery times are usually several hours later, due to computation time required.

The forecast horizon is a central term throughout this thesis and typically determined by the application: For the day-ahead market, forecast horizons are at least 18 hours to 48 hours. In intraday energy markets' context, delivery times usually are set to 45 minutes before the forecast valid time ('gate closure'), determining the minimal required forecast horizon. For processing and decision making by the forecast user, an additional time span is required: Thus, in the context of this thesis, focus is on forecast horizons of around two hours ahead.

The properties of the forecast dataset evaluated have a high degree of influence on the outcome of forecast quality assessment, especially when comparing different forecast models. For the given evaluations, only daytime values are considered, as during night-time all models would perfectly predict zero irradiance or power production respectively. To maintain comparability of different models, datasets are selected according to the availability of forecast data, and consistency among the datasets evaluated is maintained. For example, CMV forecasts are currently only computed as soon as daytime satellite images are available: For required forecast horizons of several hours, forecasts are possible several hours after sunrise at the earliest. In evaluations and comparisons presented, the evaluated datasets are reduced to hours all forecast models compared have data available.

Table 2.1.: Glossary of relevant terms used in forecasting

single site **forecast**	forecasts computed for single locations and systems
(spatially) averaged ...	single site forecasts averaged over differently sized regions
regional ...	forecasts derived by the upscaling approach for larger regions
forecast valid time	periods or point of time while/for which the forecast is valid
... delivery time/origin	point of time a forecast is delivered
... lead time/horizon	time interval between delivery and valid time
... base time	point of time a forecast run is started

2.3.2. Metrics

For assessing forecast accuracies, various measures are introduced e.g. in [8, 62, 63, 64]. The metrics applied here are described in this section, based on a similar introduction in Kühnert et al. (2015) [65]. The forecast error of quantity x, e.g. irradiance I, PV power P, or temperature T is given as:

$$\epsilon = x_{pred} - x_{meas} \tag{2.1}$$

with x_{pred} the predicted and x_{meas} the measured value. As standard measures to assess forecast accuracy, the root mean square error (rmse) and the bias error are used:

$$rmse \quad = \quad \sqrt{\frac{1}{N}\sum \epsilon^2}, \quad bias = \frac{1}{N}\sum \epsilon. \tag{2.2}$$

Due to the quadratic error weighting in the rmse, large forecast errors have a larger impact than smaller deviations. This behavior reflects the impact and importance of large errors for costs and stability of the energy supply system. Systematic deviations of the forecasts are reflected by the bias. A general overestimation of the predicted value is indicated by a positive bias, underestimation by a negative bias.

Additionally, the nrmse and nbias are used, both normalized to the average measured quantity x_{meas} :

$$nrmse = rmse/\ \overline{x}_{meas}, \ nbias = bias/\ \overline{x}_{meas} \tag{2.3}$$

The evaluation of *single site* forecasts is realized by considering ϵ for each of N time steps i and for M single systems k equally, using single site measurements as a reference:

$$rmse = \frac{1}{\sqrt{N \cdot M}}\sqrt{\sum_{i,k}^{N,M} \epsilon_{i,k}^2}, \quad bias = \frac{1}{N \cdot M}\sum_{i,k}^{N,M} \epsilon_{i,k}. \tag{2.4}$$

For spatially averaged forecasts, all single PV systems or meteorological stations in the corresponding area are averaged for each time step and accuracy measures are applied to these values. The reference is defined as the average of all single stations in the dataset:

$$x_{area,i} = \frac{1}{M}\sum_{k}^{M} x_{i,k} \tag{2.5}$$

Often the interest lies in the improvement in rmse of a forecast model with respect to a reference forecast model, which can easily be quantified via the rmse dependent Improvement Score IS, defined as:

$$IS_{rmse}(forecast, reference) = 1 - \frac{rmse_{forecast}}{rmse_{reference}} \tag{2.6}$$

With this definition, $IS_{rmse} = 0$ indicates no difference between the models, positive IS values an improvement of the model, negative a decline in forecast quality, as expressed by the rmse. Below, the IS_{rmse} is shortly notated as IS.

3. Short-term irradiance forecasting

Forecasts of global horizontal irradiance are fundamental for PV power forecasting and introduced in this chapter. Focus here is on forecast horizons of up to five hours ahead as required for intraday trading. A satellite based forecasting approach using cloud motions vectors (CMV) is presented and evaluated in comparison to forecasts based on numerical weather predictions (NWP) and a persistence model. By this, potential and limitations of this satellite-based approach are assessed.

The physical quantities global horizontal and clear sky irradiance, as well as the clearness and clear sky index are introduced in section 3.1. Irradiance assessment based Meteosat Second Generation satellite images and the Heliosat method is described in section 3.2. Based on this Heliosat method, a cloud motion vector (CMV) forecast approach is introduced in section 3.3. In section 3.4 and section 3.5 irradiance forecasts based on numerical weather predictions (NWP) and on a persistence model are presented. The forecast quality based on the approaches introduced is evaluated subsequently, describing the dataset used in section 3.6 and giving a thorough analysis of forecast errors in section 3.7. A new CMV forecasting approach for the morning hours based on infrared images is introduced in section 3.8. Section 3.2, 3.3 and 3.7 are partially based on evaluations presented in Kühnert et al. (2013) [60], section 3.8 refers to Hammer et al. (2015) [66]. Both were published in the context of research done for this thesis.

3.1. Global horizontal and clear sky irradiance

Global horizontal irradiance is of main interest when referring to PV power assessment and forecasting. The irradiance at a specific site on earth's surface is subject to deterministic and non-deterministic processes. Outside the atmosphere, the extraterrestrial solar irradiance I_{ext} received by a surface perpendicular to sun is determined by the solar constant I_0 (as defined $I_0 = 1367$ W/m^2 by the WMO[1]) and by the annual variation of the eccentricity ϵ of the earth's orbit around the sun. Deterministic variation of solar irradiance is added on an annual and diurnal basis when referring to a fixed surface on top of the atmosphere. Here, the solar zenith angle θ_Z and the azimuth angle ϕ determine the irradiance received. When considering irradiance on the earths' surface, extinction processes in the atmosphere have to be considered additionally. These processes are induced by air molecules, water vapor, particles and aerosols in the atmosphere and to a high extent by clouds. A detailed description of the processes involved can be found e.g. in Liou (1980) [67] or Iqbal (1983) [68]. Scattering of light in the atmosphere causes an splitting of irradiance in a diffuse and direct component I_d and I_b with the global horizontal irradiance defined as the sum

$$I = I_d + I_b. \tag{3.1}$$

[1] World Meteorological Organisation

Besides the deterministic trends, the processes influencing global horizontal irradiance I can be separated into two categories: The irradiance in case of clear sky with absorption processes only by the atmospheric constituents on the one hand and the absorption of irradiance by clouds on the other.

The clear sky irradiance I_{clear} includes atmospheric extinction of irradiance in case of no clouds by water vapor, ozone and aerosols. To give a quantification of the clear sky irradiance, different models exist, such as the model of Dumortier [69] or the SOLIS clear sky model [70]. In this thesis, calculations of clear sky are based on the Dumortier (1995) [69] model according to Fontoynont et al. (1998) [71] with information on turbidity from Remund (2009) [72] or from Bourges (1992) [73]. The diurnal and annual variation are mainly dependent on the sun-earth geometry and corresponding to the incident angles on the horizontal surface. The diurnal and annual dependency of clear sky irradiance is displayed in fig. 3.1, exemplarily shown for one location in Germany and the 21st June and the 21st of December. Minimum clear sky irradiance is observed for the 21st of December (winter solstice), highest on the 21st of June (summer solstice).

Based on the global horizontal irradiance I, the extraterrestrial irradiance I_{ext} and the clear sky irradiance I_{clear}, the clearness and clear sky index are defined. The clearness index relates the irradiance at the surface to the irradiance outside the atmosphere, without extinction processes by the atmosphere or clouds considered. It is defined as

$$k_t = \frac{I}{I_{ext}} \tag{3.2}$$

Similar to that, the clear sky index k^*, defined as ratio between global and clear sky irradiance at the surface, is defined as:

$$k^* = \frac{I}{I_{clear}} \tag{3.3}$$

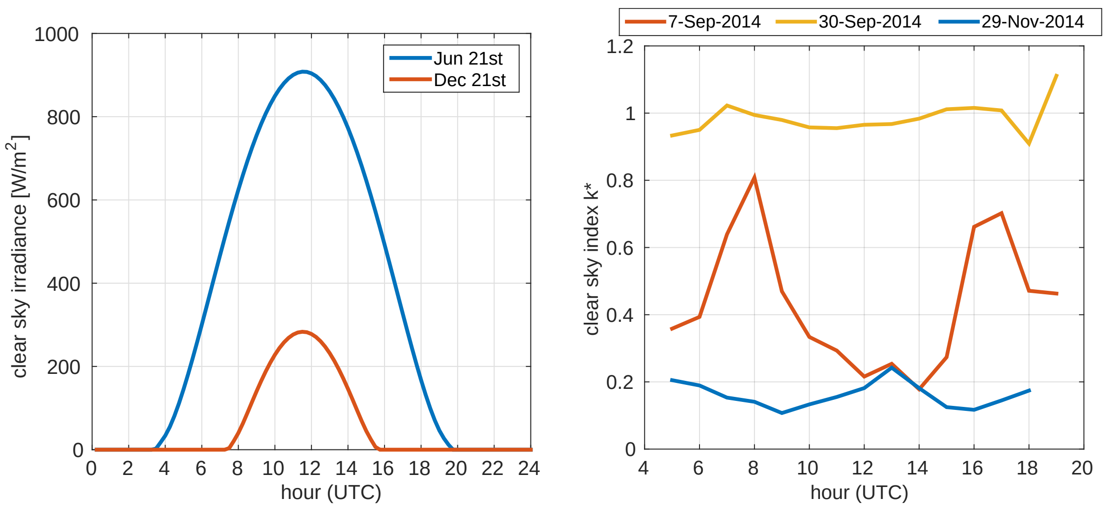

Figure 3.1.: Left: Clear sky irradiance for 15 minute values for an exemplarily chosen site (N 53.17°, E 8.23°) Germany at the 21st of June and 21st of December. Right: Clear sky index k^* for three days with different characteristics of k^*, based on ground measured irradiance with 1 hour resolution.

By this definition, a measure of the transmissivity of clouds is given, taking absorption processes in the clear sky atmosphere into account. The course of k^* for three typical weather situations is shown in the right panel of fig. 3.1: For clear sky days (see 30-Sep-2014, yellow line, in fig. 3.1), the k^* is constantly equal or close to 1; values above 1 are possible due to inaccuracies in the clear sky model or turbidity information, due to limited accuracy at low irradiance values especially for zenith angles, or also in situations of irradiance enhancement by reflection at cloud ceilings. In overcast situations (see 29-Sep-2014, blue line, in fig. 3.1) the clear sky index reaches values as low as around $k^* \approx 0.1$, whereas $k^* = 0$ is never reached as even on overcast days, since diffuse irradiance is always $> 0 \frac{\mathrm{W}}{\mathrm{m}^2}$. At days of variable cloud cover (see 7-Sep-2014, orange line, in fig. 3.1) due to broken cloud situations or passing cloud field, k^* changes significantly over the day. When deriving k^* from irradiance averaged over a period of time, in broken cloud situations the average k^* can be composed of situations of clear sky and overcast and is not distinguished from constant cloud cover at the same level of k^*.

3.2. Irradiance from satellite data (Heliosat method)

Global surface irradiance information is retrieved from Meteosat satellite (MSG) images operated by the EUMETSAT[2]. The MSG satellites are geostationary positioned in orbit at 0° longitude and latitude. The satellites' sensors receive reflected or emitted radiation from earth's surface in 11 spectral channels (from long-wavelength infrared to visible) with a spatial resolution of 3 km × 3 km at the sub-satellite point. The area of Europe, Africa and the Atlantic Ocean, as well as parts of Asia and South America are within the field of view. In addition, a high resolution channel provides visible broadband irradiance (600 to 900 nm) with a resolution of 1 km × 1 km at the sub-satellite point. This channel however is restricted to Europe and parts of Africa [74]. Using MSG images for other than sub-satellite pixels, the lower and non-uniform resolution of the image pixels according to their longitude and latitude has to be considered. E.g. for sites in Germany, the size of one image pixel corresponds to approximately 1.2 km in east-west and 1.8 km in north-south direction for the HRV channel and around 3.6 km × 5.4 km for the channels with lower resolution. By the MSG satellites, data close to real time is available with a 15 minutes resolution [75].

Irradiance incident on the earth's surface is determined from Meteosat satellite images by using the Heliosat method. This method, first published by Cano et al. (1986) [76] and further developed and improved for solar energy applications by Beyer et al. (1996) [77] and Hammer et al. (2003) [78], uses the backscattered irradiance measured by the satellite to gain cloud information. The intensity of reflected irradiance from clouds in the visible spectral channel is higher than the irradiance intensity reflected by land and water, except for snow-covered land areas. Therefore, the solar irradiance scattered back by the earth's surface and by clouds is proportional to the cloud cover. Based on this cloud information, the transmission of radiation through the atmosphere and the resulting global surface irradiance can be derived.

Intensity information from satellite images, i.e. the amount of digital counts c for each image pixel reduced by a constant value c_0 to account for the sensor offset and normalized

[2] European Organisation for the Exploitation of Meteorological Satellites

by the solar zenith angle θ_Z, is used to derive the reflectivity

$$\rho = \frac{c - c_0}{cos(\theta_Z)}. \tag{3.4}$$

The reflection of an individual pixel is assumed to be emanating from ground surface ρ_{gr} and from clouds ρ_{cl}:

$$\rho = n\ \rho_{cl} + (1-n)\ \rho_{gr} \tag{3.5}$$

The dimensionless cloud index n contains information on the cloud cover and transmissivity for each pixel and can be calculated using eq. 3.5. Ground clouds reflectivity ρ_{gr} and ρ_{cl} are derived from sequences of satellite images. The ground reflectivity ρ_{gr} describes the combined reflectivity from ground surface and the clear atmosphere. It is a function of the surface type, such as the sea surface or land surface with or without vegetation, of seasonal changes in vegetation, and of diurnal variations caused by anisotropical reflection depending on the solar zenith angles. Creating ground reflectivity maps using the mean of the lowest reflectivity values for each pixel per time slot in the preceding 30 days leads to accurate and robust ρ_{gr} values. The cloud reflectivity ρ_{cl} is empirically determined by analyzing pixel intensity histograms [79].

The clear sky index k^* (see definition 3.3) can be derived from the cloud index n with an approximately linear relationship [66]:

$$k^* = \begin{cases} 1.2 & \text{for } n \leq \text{-0.2} \\ 1 - n & \text{for -0.2} < n \leq 0.8 \\ 1.661 - 1.7814n + 0.7250n^2 & \text{for } 0.8 < n \leq 1.05 \\ 0.09 & \text{for } 1.05 < n. \end{cases} \tag{3.6}$$

Global horizontal irradiance I can be derived from Eq. (3.3), using this k^* derived from satellite images and clear sky irradiance I_{clear}. Here, we use the clear sky model by Dumortier [69, 71], with information on the atmospheric components from the Bourges (1992) [73] model.

The issue of snow-covered land surfaces is addressed in Heinicke (2006) [80]: Clouds and snow show similar reflectivity in the visible channel and thus can be confused with each other. Snow can be detected from satellite images at the visible channels at 0.6μm and the near-infrared channel at 1.6μm for each pixel and be distinguished from clouds [80, 66]. However, for the evaluated irradiance calculation and forecasting, this approach was not implemented so far and is subject of ongoing development.

3.3. Cloud Motion Vector (CMV) forecasts

The development of global horizontal irradiance up to some hours ahead is strongly dependent on the movement of cloud structures. Based on MSG satellite high resolution visible (HRV) images and the Heliosat method, a short-term irradiance forecast approach using cloud motion vectors (CMV) is used. This approach was first proposed by Beyer et al. (1994) [81] and further investigated in Lorenz et al. (2004) [12] and Hammer et al. (1999) [82]. In the context of this thesis, in Kühnert et al. (2013) [60] an in-depth evaluation of the CMV forecast accuracy using a one-year dataset is published. A newly developed nighttime cloud index retrieval was introduced in Hammer et al. (2015) [66].

An overview of the CMV forecast approach is provided in fig. 3.2:

1. Cloud index (CI) images are derived from MSG images by the Heliosat method,
2. cloud motion vectors (CMV) are computed and future CI images extrapolated,
3. irradiance forecasts are derived by based on the extrapolated CI images.

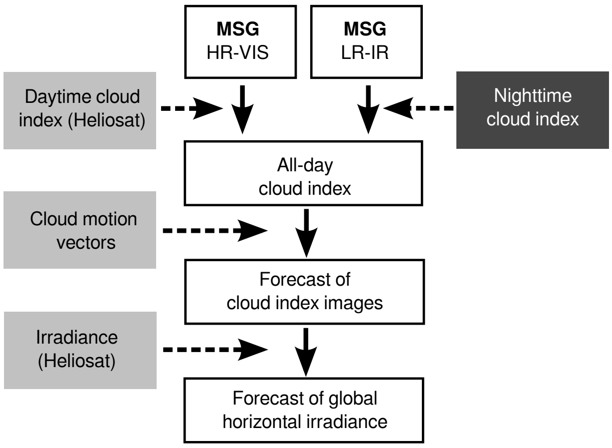

Figure 3.2.: Processing of CMV forecasts from daytime cloud index images based on MSG satellite data from HRV channel and the Heliosat method, being the basis for the following evaluations (section 3.7). Nighttime cloud index images based on the MSG infrared channels are newly introduced in Hammer et al. [66] and described in section 3.8. Based on these cloud index images, cloud motion vectors (CMV) are derived, future cloud index images extrapolated and thus forecasts of irradiance derived. From [66], based on [60].

In this section, an overview on the forecasting algorithm is given, based on the description in Küphnert et al. (2013) [60]. For more details on the approach please refer to this source or to Lorenz et al. (2004) [12]. CMV forecasts are calculated based on the following steps:

1. Cloud motion vectors are derived comparing two consecutive cloud index images,
2. cloud movement is extrapolated to the next hours based on the latest CI image,
3. a smoothing post-processing is applied to the predicted cloud index images,
4. irradiance forecasts are derived from predicted CI images with the Heliosat method.

Cloud motion vectors (CMV) are determined by comparing consecutive cloud index images derived from MSG high resolution visible range channel (HRV) images, see fig. 3.3. The most recent cloud index image n_0 at time t_0 is compared with the preceding cloud index image n_{-1} at time $t_{-1} = t_0 - \Delta t$, where Δt represents the time step between two consecutive images (Δt = 15min for MSG images). Deriving cloud movement by comparing cloud structures in images n_0 and n_{-1} is performed by assuming i) constant pixel intensities for cloud structures in both images and ii) smooth wind fields which usually exist at typical cloud heights. These assumptions allow for detecting cloud motion by matching the same cloud pattern in consecutive images: Rectangular areas in image n_{-1} ('target areas') around the origin of each motion vector are compared to equally sized areas within their neighborhood ('search area') in image n_0 to detect the movement of cloud patterns between these images. The detection of cloud patterns of image n_{-1} in the subsequent image n_0 is performed by minimizing the mean square pixel differences for these target areas, defined as

$$mse = \frac{1}{N} \sum_{i=1}^{N} (n_0(x_i + d) - n_{-1}(x_i))^2 \tag{3.7}$$

where d is the shift vector of all pixels x_i in the respective area. For each target area in the search area, the mse is calculated and the area with the minimal error is selected, defining the motion vector for this area.

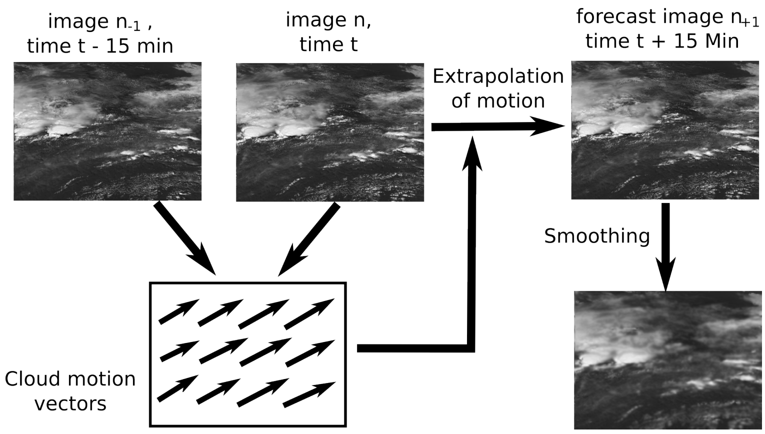

Figure 3.3.: CMV forecast approach: (i) detection of motion for existing cloud structures evaluating the most recent cloud index images, (ii) application of the derived motion vector field to the most recent cloud index image to extrapolate the movement of cloud structures and (iii) smoothing of extrapolated images.

The extrapolation of cloud index images is done by segmentally moving the existing cloud structures along the motion vectors of each area. Assuming persistent cloud patterns and wind fields, this method allows the prediction of cloud index images for the next hours: The subsequent cloud index image n_{+1} is created by applying motion vectors to the most recent cloud index image n_0 to extrapolate the cloud movement. Iterating this extrapolation on n_{+1} to gather n_{+2} up to n_n provides extrapolated cloud index images up to time step t_n. The extrapolation of each image step is performed using the same $\Delta t = 15$min time step. The step-wise iteration of extrapolation, rather than extrapolating to n_n using a single scaled vector, has the advantage of capturing changes in movement of the clouds in other areas of the image. Thus the change of clouds' movement in space is captured. However, changes in time with onward forecast horizons are not considered by this approach. Also, the extrapolation of cloud movement does not consider the formation and dissolution of clouds.

The extrapolated cloud index images are post-processed using a smoothing filter. This step reduces the impact of inaccuracies in the extrapolated images which mainly occur due to spatial differences between the predicted and the actual position of clouds. These deviations are caused by undetected changes in cloud motion direction and speed, and by propagation of fine cloud structures which are likely reshaping during cloud movement and therefore are not predictable. Applying a smoothing filter leads to a considerable reduction of rmse by reducing this 'noise' [60, 12]. As the extrapolation of cloud structures leads to an increasing propagation of forecast errors with forecast horizon, the optimal size of the smoothing area a is changing with each time step of extrapolation. For larger time scales, favoring larger forecast errors, a more extensive smoothing is favorable. As a last step, forecasts of irradiance are derived using the Heliosat method introduced in section 3.2, applied to the extrapolated and smoothed cloud index images.

3.4. Numerical weather predictions (NWP)

Numerical weather predictions (NWP) models are used for predicting the state of the atmosphere for several days ahead. These predictions are based on the assessment of the initial state of various parameters from measured data or reanalysis of previous forecast runs. The development of the atmospheric state is predicted using a parametrization of atmospheric conditions and the application of numerically solved differential equations, describing the physical laws involved. A spatial and temporal discretization with fixed resolution is commonly used.

Numerical weather predictions are available from several forecast providers, such as e.g. the ECMWF[3] or the DWD[4]. In this thesis, ECMWF global model forecasts from the integrated forecast system (IFS) are applied. They are used with time steps of 3 hours and a spatial resolution of $0.25° \times 0.25°$, corresponding to areas resolved of around 12.5 km × 12.5 km. Forecasts are run by the ECMWF twice a day at 00UTC and 12UTC, with delivery times usually about 5 to 6 hours later due to large and time-consuming computational efforts. Besides, NWP from the COSMO-EU model operated by the German Weather Service DWD are also utilized in the PV power prediction system of the University of Oldenburg and *meteocontrol GmbH*. For the COSMO-EU model forecasts in hourly resolution and a spatial resolution of 7 km × 7 km are provided.

For the application in the PV power forecasting model, several post-processing steps are applied in order to achieve an optimization of temporal and spatial resolution for site specific irradiance forecasts [14, 23]. First, a spatial averaging procedure is performed leading to an rmse reduction as described in Lorenz et al. [23]. As a second step, temporal interpolation procedures are implemented using a linear interpolation of the clear-sky index k^*. From 3-hour mean irradiance $I_{NWP,3h}$ values, an average 3 hours clear-sky index $k^*_{3h} = I_{NWP,3h}/I_{clear,3h}$ is calculated. These k^*_{3h} values are interpolated linearly to obtain clear-sky indices $k^*_{t_{res}}$ with the required temporal resolution t_{res}. The irradiance forecast in the required resolution is gained by $I_{NWP,t_{res}} = k^*_{t_{res}} \cdot I_{clear,t_{res}}$. Depending on the field of application, t_{res} here is usually 1 hour or 15 minutes. For the COSMO-EU model, the same interpolation is performed as for the ECMWF IFS forecasts but adapted to the corresponding model resolutions.

In Lorenz et al. [61] an approach is presented, combining irradiance forecasts from the ECMWF IFS and DWD COSMO-EU model, and optionally including CMV forecasts (section 3.3). A significant improvement of forecast accuracy especially for regional forecasts is achieved by this, as displayed in [61].

[3] European Centre of Medium Range Weather Forecasts [27]
[4] Deutscher Wetterdienst, German Weather Service [83]

3.5. Persistence forecasts

As a simple reference forecast the persistence approach is introduced in this section. With this approach, i) the cloud cover is assumed to be constant for the hours after forecast calculation and ii) the deterministic diurnal pattern of irradiance is considered. Irradiance measurements I_{meas} at the time t_0 the forecast is calculated are used to derive the clear sky index $k^*_{meas}(t_0)$ (see section 3.2) using the clear sky irradiance $I_{clear}(t_0)$ at a specific site. To obtain future irradiance values, the clear sky index $k^*(t) \equiv k^*_{meas}(t_0)$ at time $t = t_0 + \Delta t$ is assumed to be constant for the next hours. The persistence forecast of irradiance $I_{pers}(t)$ at time $t = t_0 + \Delta t$ is calculated as

$$I_{pers,\Delta t}(t) = k^*_{meas}(t_0) \cdot I_{clear}(t).$$

3.6. Datasets for forecast evaluation

Evaluations of forecast accuracy are performed based on measurements at a total of 217 stations (fig. 3.4 left and table 3.1), with different sets of sites distinguished. 'Set 1' contains all sites in the dataset with measurements of global horizontal irradiance I. Sets '2' and '3' are subsets of 'set 1', with either an additional measurement period ('set 2', with Sep 2014 to Feb 2015) or additional parameters measured ('set 3', with additionally measured diffuse irradiance I_d and ambient temperature T_a). The different sets are assigned to evaluations performed in different sections of this thesis, as indicated in the last column of table 3.1. A quality control of the meteorological measurements is performed, containing a check for availability and consistency of data. Measurements of $I < 0$ and $I > 1500$ W/m^2 are not considered in evaluations. Temperature measurements of T_a are limited to $-40°\text{C} \leq T_a \leq +60°\text{C}$.

Table 3.1.: Datasets of meteorological sites with measured parameters and time periods.

ID	**measured parameter**	**period**	**section**
Set 1 (217 sites)	global horizontal irradiance I	01/2012–12/2013	sec. 3.7
Set 2 (116 sites)	global horizontal irradiance I	09/2014–02/2015	sec. 3.8
Set 3 (32 sites)	ambient temperature T_a	01/2012–12/2012	sec. 4.3
	diffuse irradiance I_d	01/2012–12/2012	sec. 4.2.1

The temporal resolution for all measurements is 1 hour. Forecasts evaluated are interpolated or averaged to the same temporal resolution: For NWP models, the resolution is increased from 3 hours forecast resolution to 1 hour in accordance with the interpolation procedure introduced in section 3.4. For CMV forecasts, with a model resolution of 15 minutes, 1 hour averages are built. This leads to a grouping of sub-hourly forecast horizons: Forecasts e.g. 15 minutes to 1 hour ahead are averaged to hourly values and in the following designated as the '1 hour' forecast horizon. Forecast horizon '0' here denotes the point of time the satellite image is available earliest, neglecting the time needed for computing forecasts of typically several minutes.

In the following evaluation, irradiance forecasts from different models introduced in the previous sections are compared. Focus is on the CMV-based irradiance forecasts. In accordance with the definition of the forecast horizon given above, forecast horizons of 1 to 5 hours are evaluated. These CMV forecasts are compared to:

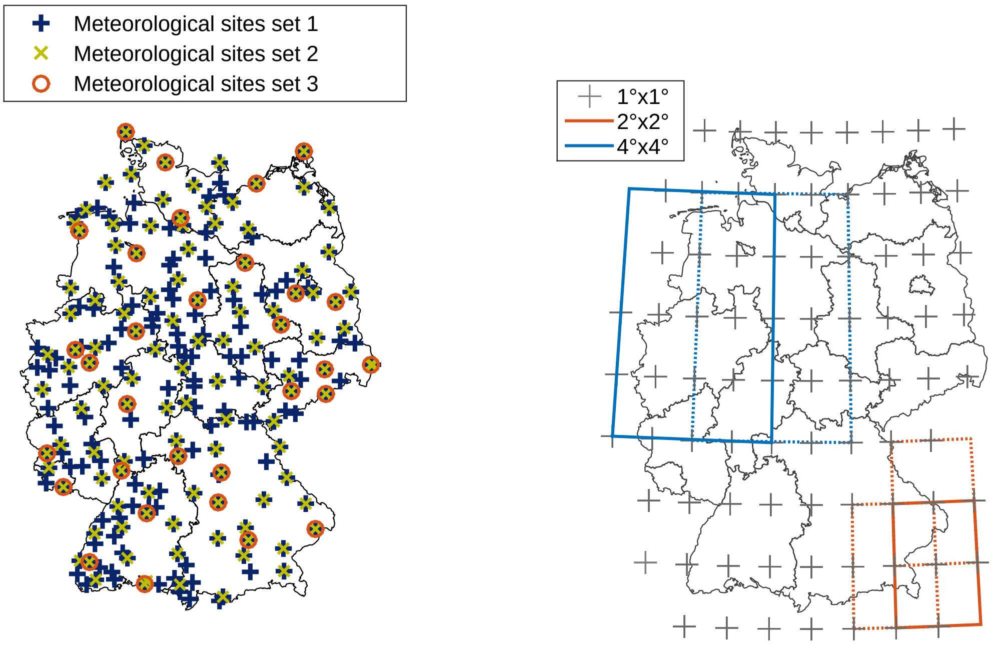

Figure 3.4.: Left: Meteorological sites with measured irradiance and temperature, grouped into different datasets. Right: Division of areas averaged for evaluation, exemplarily for $1^\circ \times 1^\circ$, $2^\circ \times 2^\circ$ and $4^\circ \times 4^\circ$, with overlap of the areas by their half width and height (except for $1^\circ \times 1^\circ$ with no overlap).

- NWP irradiance forecasts by the ECMWF of the 12UTC-run of the respective previous day: Here, the forecast horizon is not defined on an hourly scale but composed to the intraday forecast horizon. Depending on the forecast valid and delivery time, this comprises forecast horizons between 6 and 30 hours ahead.
- Persistence forecasts, based on irradiance measurements at the point of time the forecast is generated ('horizon 0'). The same forecast horizon terminology as for CMV-based forecasts is used here.
- Irradiance from satellite data, being the accuracy of the Heliosat method applied to non-predicted satellite images and thus corresponding to forecast horizon '0'.

Another focus in the evaluations presented is the comparison of single sites' and spatially averaged forecasts. Single site forecasts are most relevant to PV plant owners for direct marketing or for demand side management, as introduced in section 2.1. Based on single sites' forecasts, spatial averages are computed, being of interest to the TSOs and the balancing process at the energy market. The impact of the size of areas averaged on the forecast rmse is considered: To do so, areas of same size for $1^\circ \times 1^\circ$, $2^\circ \times 2^\circ$, $4^\circ \times 4^\circ$ and $6^\circ \times 6^\circ$ are used with an overlap of their half width, as exemplarily shown in the right panel of fig. 3.4. These spatial averages are concatenated and statistical measures are applied as for single sites.

3.7. Evaluation of short-term irradiance forecasts

In this section, an evaluation of a two-years dataset of CMV-based irradiance forecasts is given, compared to the accuracy of NWP-based and persistence forecasts, and to the accuracy of the Heliosat method as a reference. Focus is on i) the differences in forecast errors for single sites' and spatial averages, on ii) the dependence of forecast error on the forecast horizon and iii) the dependence of forecast error on different parameters as solar zenith angle, time of day or season.

A qualitative evaluation of forecast quality and the differences for single site and averaged forecasts are visualized by frequency scatter plots (fig. 3.5). Here, cloud motion vector (CMV) 2 hours-forecasts are compared to measured irradiance. For single sites, a relatively large scatter is observed, with an increased amount of pairs of values at low irradiance levels. The scatter for all sites' averages is significantly lower, as smoothing effects reduce the error for spatially averaged forecasts: Small-scale fluctuations are smoothed and mainly the overall weather situation has an impact on the spatially averaged forecasts. From both scatter plots, no significant over- or underestimation can be deduced.

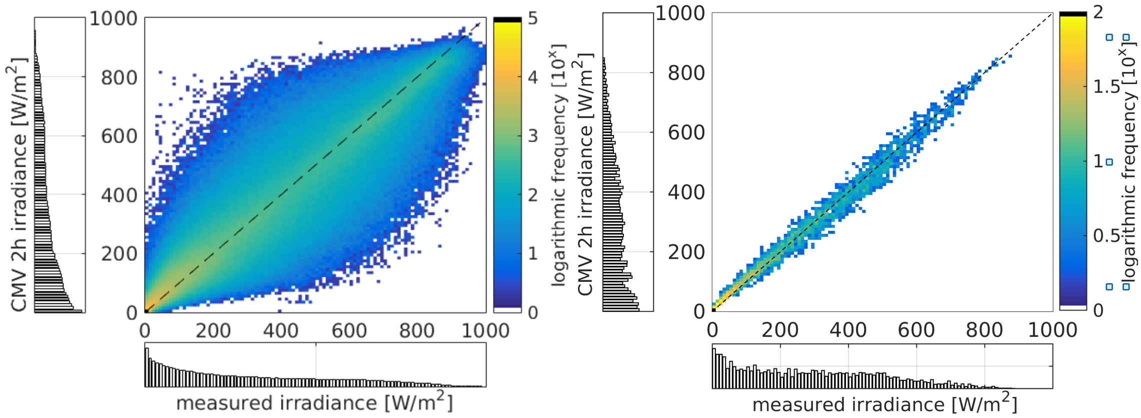

Figure 3.5.: Frequency distribution scatter plots for single site forecasts (left) and all sites' averages (right). The color code provides information on the frequency of the displayed pairs of values. Dataset: Jan 2012–Dec 2013, 217 sites, 1 hour resolution, $\theta_Z < 80°$.

The impact of spatial averaging can also be found in the quantitative evaluation in terms of rmse and bias. These are given in dependence on the forecast horizon from 1 to 5 hours ahead in fig. 3.6. As stated above, the level of rmse is significantly smaller for spatially averaged forecasts (note different scales of fig. 3.6 left and right). For single sites, the rmse of CMV forecast ranges from around 52 W/m^2 to 108 W/m^2, for all sites' averaged CMV forecasts only from 17 W/m^2 to 42 W/m^2. CMV and persistence forecasts show a strong dependence of the rmse on the forecast horizon, whereas the NWP forecast rmse displayed basically is independent of the horizon. The rmse of satellite-based irradiance ('sat') includes no forecasting but displays the accuracy of irradiance derived from satellite images: This serves as a reference for the minimum rmse (around 50 W/m^2 for single sites and 15 W/m^2 for all sites' averages) of the CMV forecasts. For one hour CMV forecasts, the rmse is similar to this minimum rmse of the Heliosat method, as cloud movement usually does not have a high impact for this short lead time.

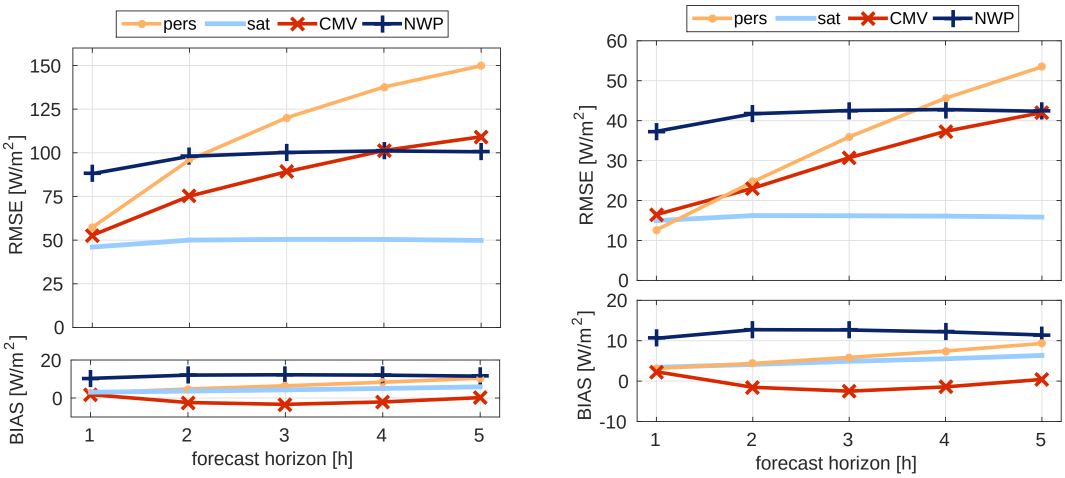

Figure 3.6.: Evaluation of forecasts for single site (left) and averaged over all sites for forecast horizons from 1 to 5 hours. Comparison of persistence, CMV and NWP forecasts and irradiance derived from satellite images (no forecast). Dataset: Jan 2012–Dec 2013, 217 sites, 1 hour resolution, $\theta_Z < 80°$.

From that level the CMV forecasts' rmse increases with forecast horizon. At around 4 hours ahead for single sites, and 5 hours ahead for all sites' averages, the CMV forecast rmse reaches a similar level as the NWP intraday forecasts. In both cases, CMV forecasts shows lower rmse values than the persistence forecasts from around one hour onward for single sites and from around 2 hours for averaged forecasts.

The bias error measure shows systematic deviations for all forecast approaches. An overestimation is visible for the NWP-based forecasts by around $+10$ W/m^2, regardless the forecast horizon. The Heliosat method shows a slight systematic overestimation of around 5 W/m^2. For the CMV forecasts, the bias changes between $+5$ W/m^2 for 1 hour and -5 W/m^2 for 3 hours ahead.

In the evaluation presented, only forecasts generated at solar zenith angles of $\theta_Z < 80°$ at the time of forecast calculation are considered. This is a result of low forecast quality of the CMV approach for high zenith angles, as displayed in fig. 3.7 (left). There the dependency of CMV 2h ahead forecasts' rmse on the solar zenith angle at time of forecast computation is displayed for all sites' averages. Forecasts generated at $\theta_Z \geq 80°$ show a significantly higher rmse: The Heliosat method used to derive cloud index images and surface irradiance is so far restricted to satellite images in the visible spectral range and shows low performance in the twilight zone (see [60]). This issue is addressed in the following section 3.8.

The diurnal dependency of forecast rmse for single sites is shown in fig. 3.7 (right), exemplarily for the months May to July of both years 2012 and 2013. It follows the same trend as the irradiance incident on ground surface, with highest irradiance and thus absolute rmse at noon. The limitation of forecast generation by the $\theta_Z < 80°$-threshold leads to an unavailability of CMV forecasts for the morning hours. In winter months, with a higher share of high solar zenith angles, this can lead to a first availability of CMV forecasts only at noon hours.

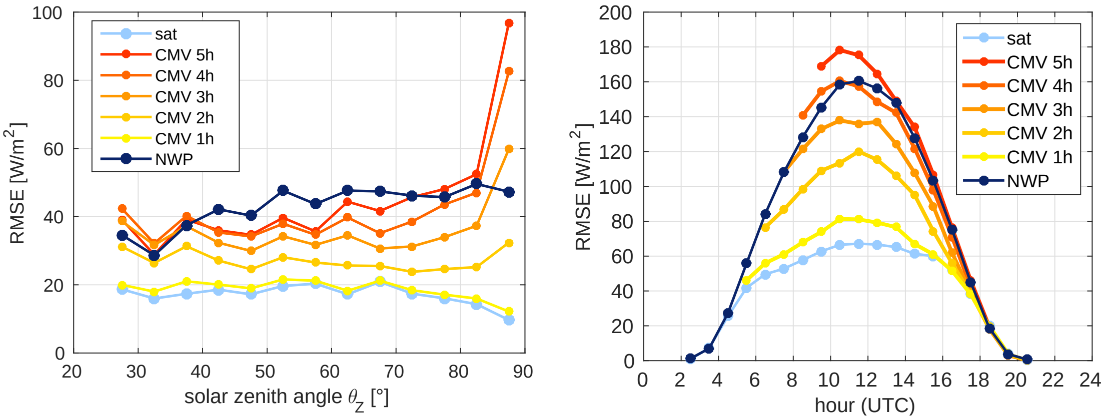

Figure 3.7.: Left: Dependency of the rmse for CMV 1-5 hour and NWP forecasts and of the Heliosat method on the solar zenith angle θ_Z at forecast calculation time for all sites' averages. Dataset: Jan 2012–Dec 2013, 217 sites, 1 hour resolution. Right: Diurnal dependency of forecast rmse for CMV 1-5 hours and NWP forecasts, and the Heliosat method. Dataset: May–Jul 2012/2013, 217 sites, 1 hour resolution, $\theta_Z < 80°$.

The impact of spatial averaging on the forecast rmse is displayed in fig. 3.8: Spatial averages are evaluated for multiple differently sized areas, as displayed in fig. 3.4. Rmse and bias are normalized to the single sites' NWP forecast error. The rmse decreases with increasing area averaged. For areas of size $4° \times 4°$, e.g., the error of CMV 2h forecasts is already less than half of the single sites' rmse; for all sites' averages less than 30% compared to single sites. However, the benefit of spatial averaging is smaller for NWP-based forecasts: Here the rmse decreases to around 40% for all sites' averages compared to single sites. On the one hand, this is a consequence of the higher bias of NWP forecasts, which is not reduced by spatial averaging as systematic deviations persist (see lower box in fig. 3.8). On the other hand, CMV forecasts show higher temporal variability than the NWP forecasts: Spatial averaging has a higher impact on the overall variability of forecasts and thus shows high potential for a rmse reduction as for the NWP forecasts with lower temporal model resolution.

The annual dependency of single sites' absolute rmse, bias and the normalized rmse are displayed in fig. 3.9 for the months January 2012 to December 2013, compared to the average measured irradiance for these months. Both, the absolute and relative rmse reveal a clear annual trend of all forecasting approaches displayed. Like for mean irradiance, higher absolute rmse values are observed in summer months than in winter. In summer months May to July the rmse reaches up to 125 W/m^2, but only up to 50 W/m^2 in December to February. An inverse behavior is visible for the relative rmse, showing much higher values in winter than in summer. For these months, the average relative rmse for NWP and CMV forecasts, and the Heliosat method is above 50% whereas in the summer months it only reaches up to 30% to 50%. This is a result of different aspects: In winter months, the mean irradiance is lower than in summer and same absolute rmse values have higher impact here. Also, the high occurrence of large solar zenith angles and of snow in the satellite images is relevant here, see Kühnert et al. (2013) [60]. The bias error of CMV forecasts is mostly independent of seasonal fluctuations. Only for NWP it shows a significant overestimation in the months January to March of both years.

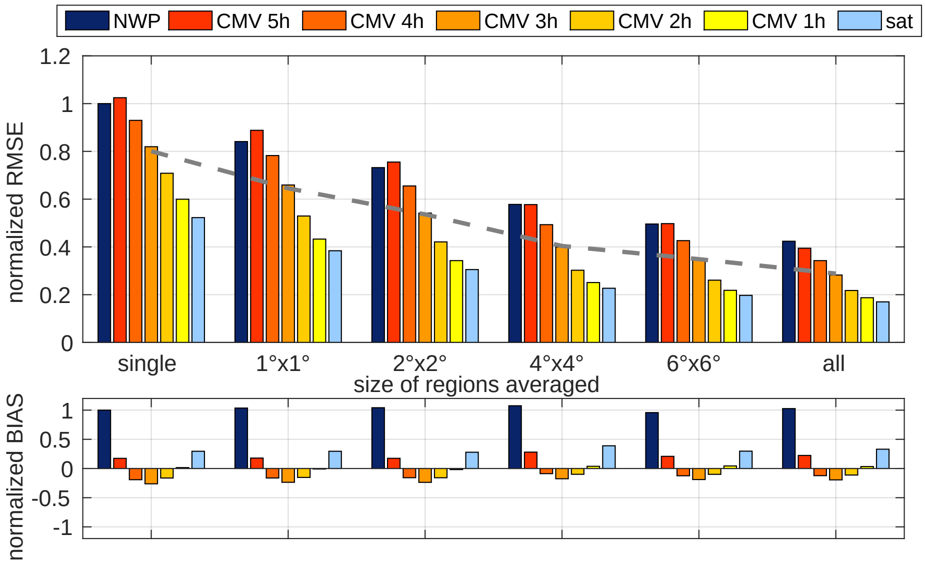

Figure 3.8.: Rmse for different forecast horizons and spatial averages according to fig. 3.4 (right), for CMV 1-5 hour and NWP forecasts and the Heliosat method. Rmse and bias are each normalized to the NWP single sites forecast error. Dataset: Jan 2012–Dec 2013, 217 sites, 1 hour resolution, $\theta_Z < 80°$.

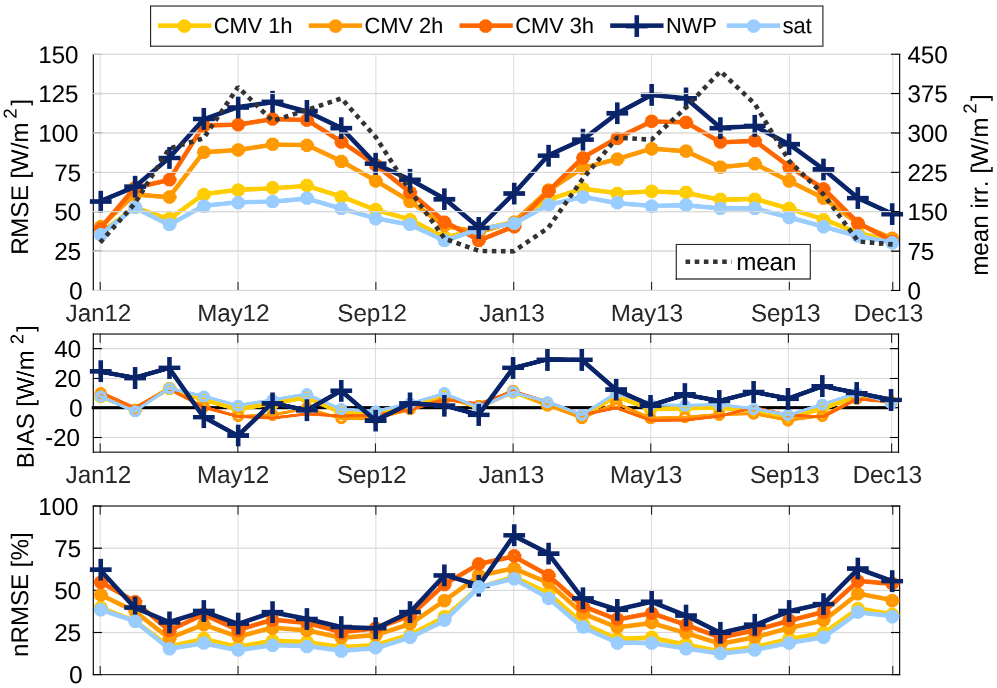

Figure 3.9.: Annual dependency of the absolute rmse and bias, and the normalized rmse for CMV 1-3 hour and NWP forecasts, as well as for the Heliosat method. Dataset: Jan 2012–Dec 2013, 217 sites, 1 hour resolution, $\theta_Z < 80°$.

3.8. CMV forecasts based on all-day cloud index

Forecasts based on the cloud motion vector approach using satellite images of the high resolution visible channel (HRV, fig. 3.10 left) are limited by the availability of satellite images at daytime only. In Hammer et al. [66], a new approach to generate nighttime cloud index (CI) images based on MSG infrared channels is developed and examined. The evaluation of the newly developed method by applying the CMV forecast algorithm is done in context of this thesis. Main findings of the approach presented are briefly summarized in this section.

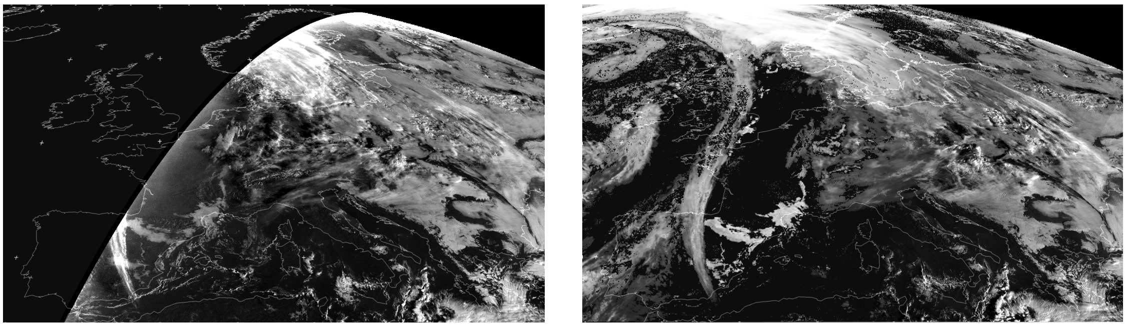

Figure 3.10.: Comparison of a visible channel only cloud index image (left, 01-Nov-2014, 0645 UTC) to an all-day cloud index image (right, 01-Nov-2014, 0600 UTC) with mixed daytime and nighttime cloud index information; from Hammer et al. (2015) [66].

The limitations of the HRV channel-based forecasts as described above become apparent in the left panel of fig. 3.10 and in evaluations presented in section 3.7: Forecasts are not available for early hours at all and show a significantly higher absolute rmse at high solar zenith angles than compared to e.g. NWP forecasts (fig. 3.7, left). To improve forecast quality for these hours, an approach for deriving all-day cloud index images (right panel of fig. 3.10) is developed. The approach presented aims at following innovations of the cloud index retrieval [66]:

1. Better description of the air mass for the twilight zone by introducing the air-mass function of Rozenberg (1966) [84],
2. calculation of CI images from infrared images of the channels at 3.9 μm and 10.8 μm using the brightness temperature differences (BTD) : $BTD = T_{3.9} - T_{10.8}$,
3. composition of an all-day cloud index image n by combining nighttime and daytime cloud index images n_{night} and n_{day}: $n = \omega \cdot n_{night} + (1 - \omega) \cdot n_{day}$, with $\omega = f(\theta)$.

A direct evaluation of the all-day cloud index images with ground measurements as it was done in the previous sections for the daytime cloud index is not possible here. The evaluation of the presented approach thus is performed by applying CMV forecasts to the all-day cloud index images and by deriving the rmse and bias for irradiance forecasts compared to ground measurements. CMV forecasts based on all-day cloud index images are compared to the established daytime cloud index-based CMV forecasts. An evaluation of 3 hours CMV forecasts with hourly measurements of global horizontal irradiance I is performed. The period for evaluation is from September 2014 to February 2015, representing a period dominated by high solar zenith angles. Snow cover in Germany was rarely occurring in these months and is not considered in the presented evaluation.

The benefit of including a better description of the air mass for the twilight zone is visualized in the left panel of fig. 3.11. Here, for one exemplarily chosen site, the daytime-only and the all-day CI-based CMV 3h-forecasts are compared, both evaluations restricted to solar zenith angles $80° \leq \theta \leq 90°$ at the time of forecast calculation. For the all-day CI-based forecasts, the scatter reduces significantly and indicates a better forecast performance. The effect of using the all-day cloud index images on the availability of forecasts is displayed in the right panel of fig. 3.11: Forecasts can now be computed at solar zenith angles $90° < \theta_Z$, leading to a much higher forecast availability for the morning hours. However, the scatter of forecasts calculated at $90° < \theta_Z$ is larger than for forecasts computed at solar zenith angles $80° \leq \theta_Z \leq 90°$.

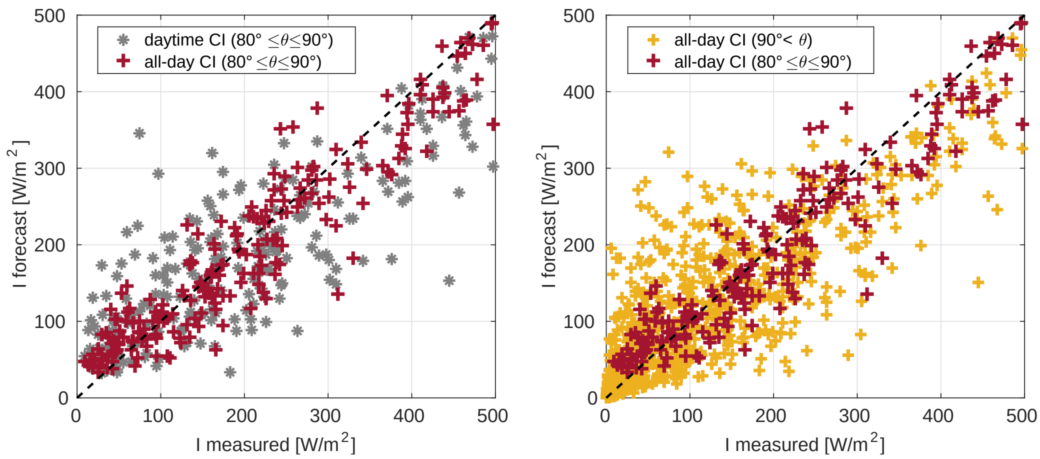

Figure 3.11.: Scatter plot of 3 hour CMV forecasts versus measured I for a single station. Left: Forecasts based on daytime only and all-day cloud index, with solar zenith angle $80° \leq \theta_Z \leq 90°$ at the time of forecast calculation. Right: Forecasts based on all-day cloud index with $90° < \theta_Z$ or $80° \leq \theta_Z \leq 90°$ at the time of forecast calculation. Dataset: Sep 2014–Feb 2015, 1 site (N 51.50°, E 7.78°), 1 hour resolution; based on [66].

A quantitative evaluation is provided in fig. 3.12, showing the diurnal dependency of the forecast rmse evaluated at a total of 116 sites ('Meteorological sites set 2', see sec. 3.6). The error of the Heliosat method, applied to the visible spectral ranges' images only, and of the NWP-intraday forecasts, using the approach combining models by the ECMWF and the DWD (see section 3.4), are displayed as a reference. For the daytime CI-based forecasts, the limited availability and low performance in the early hours (07 to 09 UTC) is visible here. At the same hours, all-day CI-based forecasts show significant lower rmse. Also, forecasts are available at earlier hours and show rmse values comparable to the NWP-based forecasts. Still, NWP forecasts show a slight advantage here. The bias error of the all-day CI-based CMV forecasts is highest for all forecasts displayed.

With the all-day cloud index images, forecasts now are available already at sunrise and show lower rmse values for the twilight zone. But, limitations of this method still are present: The spatial resolution of infrared images utilized is much lower (with subsatellite pixels' resolution is 3 km × 3 km instead of 1 km × 1 km for the HRV channel). Furthermore, the approach applied to the infrared images relates pixel information only indirectly to the transmissivity of the cloud [66]). This is in contrast to daytime CI images, for which a direct correlation of pixel information and clouds transmissivity is

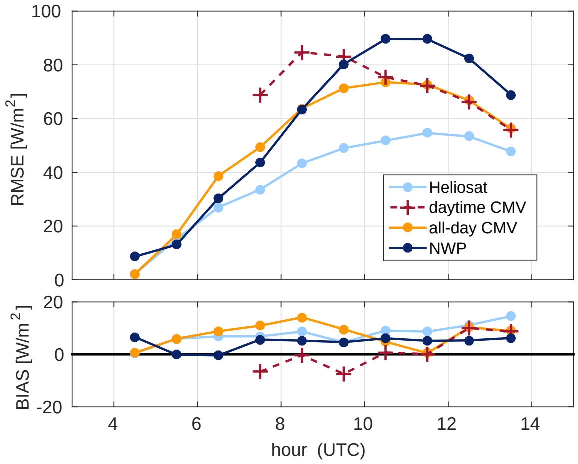

Figure 3.12.: Diurnal dependency of the forecast rmse and bias for the newly developed all-day cloud index and the established daytime only-based CMV forecasts. The accuracy of the Heliosat method is given for reference ('Heliosat'). Dataset: Sep 2014–Feb 2015, 116 sites, 1 hour resolution, forecasts calculated before noon only; based on [66].

derived. Potential for improvement is seen by integrating all-day CI-based forecasts into the combined CMV-NWP forecasting approach, leading to a reduction of bias error and thus a further improvement of overall forecast accuracy.

3.9. Conclusion

In this chapter an introduction to short-term irradiance forecasts for horizons of several hours ahead is given. Forecast accuracy of a cloud motion vector (CMV) forecasting approach is evaluated and compared to numerical weather predictions (NWP) and forecasts based on the assumption of persistence of the clear sky index k^*. Generally, CMV forecasts show better performance for forecast horizons from one or two hours ahead (for single sites or regional averages) than persistence forecasts and up to four or five hours compared to NWP forecasts. Regional forecasts, as most relevant for this application, benefit from spatial averaging effects and show significantly lower rmse than for single site evaluations. The CMV forecasting approach evaluated so far is limited by the availability of images in the visible spectral range. For high solar zenith angles at forecast calculation time, the CMV approach shows significant high rmse. A new approach using infrared images for allowing CMV forecasts computation all-day is introduced. The improvement by this approach of forecast quality and availability for the morning hours is verified.

4. PV power simulation

In this chapter irradiance-to-power conversion using explicit physical modeling is addressed. Figure 4.1 shows an outline of the forecasting scheme, with a focus on PV power simulation. The power output for PV plants is simulated based on the predicted irradiance and ambient temperature, taking into account plant specifications such as installed capacity, tilt and orientation. This includes conversion from horizontal irradiance to horizontal diffuse and direct irradiance, and to tilted plane of array (POA) irradiance in a first step. PV power efficiency is modeled by applying a parametric efficiency model, considering the irradiance and temperature dependency of power production. The PV power simulation is applied to CMV irradiance forecasts, as introduced in chapter 3.3 and to NWP-based forecasts, as described in section 3.4. The so derived site specific power forecasts are then used as input for regional PV power forecasting. One main focus in this chapter is the analysis of the simulation process and the contribution of each simulation step to the overall PV power simulation accuracy. Another focus is on evaluations of single site and regionally averaged forecasts.

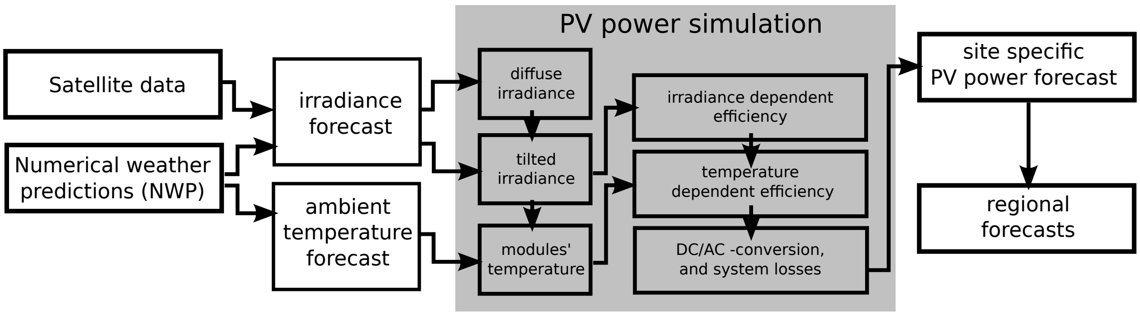

Figure 4.1.: Forecasts of global horizontal irradiance based on satellite data or numerical weather predictions are processed by a PV power simulation model. This includes the conversion from global horizontal to plane of array (POA) irradiance by conversion into diffuse and direct horizontal irradiance and the application of a tilt-conversion model. Based on this POA irradiance and ambient temperature, the PV power efficiency is modeled. Additional losses by DC to AC-conversion and other effects are considered in a last step. This PV power simulation is done on single site basis to gather regional forecasts afterwards; from [65]

First, the dataset of measured PV power used for the evaluations in this and the following chapters is introduced in section 4.1. This is followed by an introduction to the PV power simulation model in section 4.2. Temperature forecasts are focused on in section 4.3. In section 4.4 an impact analysis of the simulation steps on the overall PV power simulation accuracy is given. Section 4.5 and 4.6 provide an evaluation of PV power forecasts and a comparison to irradiance forecasts. Section 4.2.2 and 4.4 are cited from a Kühnert et al. (2015) [65].

4.1. Dataset of PV power measurements

Measured PV power for a huge dataset of more than 1300 sites is used for evaluations. The measurements were received from the monitoring database of *meteocontrol GmbH* [21]. AC power of PV power systems distributed across Germany is logged in 15 minute intervals. Meta information is provided for each system, like position (longitude λ, latitude φ), installed capacity P_{inst}, system tilt β and azimuth angle ϕ. The dataset available for evaluations here contains two years, from January 2012 to December 2013. PV systems within the dataset cover a wide range of system sizes with respect to the installed capacity, from rooftop-mounted system of several kWp up to huge commercial PV power plants with several MWp. In this section, a characterization of the dataset is given and the quality control applied on the measured data is described.

The regional distribution of sites is shown in left panel of figure 4.2. A high share of PV sites are found in southern Germany, with several areas of high PV sites density especially in south-western areas.

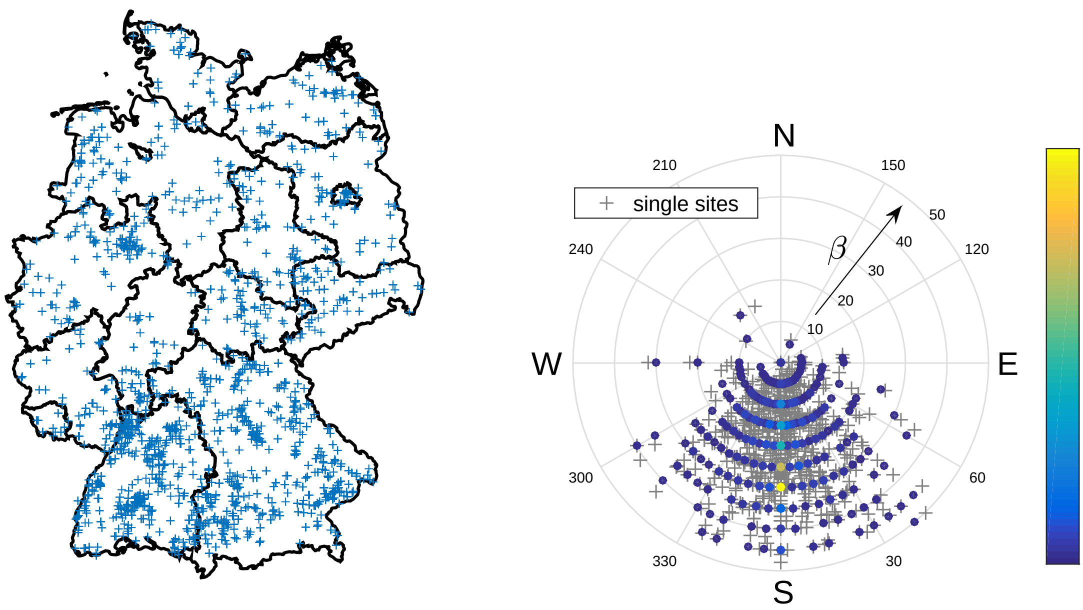

Figure 4.2.: Left: Regional distribution of PV sites. Right: Distribution of systems' tilt and orientation for dataset 'B'. The azimuth angle ϕ is displayed as polar angle ($\phi = 0°$ is South), the tilt angle β is represented by the radius (horizontally aligned corresponds to $\beta = 0$).

The dataset covers a high variation of tilt and azimuth angles (right panel of figure 4.2). Almost all stations are orientated in the range of azimuth angles ϕ from $\phi = 0$ to $\phi = \pm 90°$ with over 75% showing a south-faced orientation, within $\phi = \pm 30°$. Tilt angles vary between $\beta = 0$ and $50°$, with a high share at around $30°$. Sites with $\phi = 0$ and intermediate tilt angles β have a significant large share within the dataset.

An automatic quality control is applied to the measurement data in order to verify time stamps and information on the systems configuration, as well as to detect measurement failures. This involves several steps:

- **Adjustment of time stamp**: Time stamps are adjusted from local time to the UTC time system. To correct time information of measurements, a quality control approach as described in Lorenz (2012) [85] was applied.
- **Verification of meta data and physical plausibility**: The time series for each station is analyzed considering the range of measurements normalized to its given installed capacities. If its normalized measured power feed-in for clear sky days is constantly above 1.5 or below 0.5, this site is rejected in the following evaluations. Additionally, single measured values outside the range $0 < P_{meas}/P_{inst} < 1.5$ are also flagged as invalid.
- **Data availability**: If single values of a stations time series are detected to be outside a physical range or feature invalid values they are flagged and rejected from further evaluation. Sites with low data availability were completely rejected from evaluations.

After the quality control scheme applied, different datasets for evaluation are compiled, satisfying different requirements:

A 1348 stations: fulfilling the minimum requirements as mentioned above, with at least 90% availability of measured data considering the periods 2012 and 2013; used for upscaling evaluation in chapter 6.

B 1196 stations: Stations with more than 95% data availability and normalized $nrmse \leq 50\%$ of satellite-based PV power simulation P_{sat}; used for evaluating the physical PV power simulation approach and impact analysis (section 4.4).

C 921 stations: availability close to 95%, passing a stricter manual inspection focusing on gaps in datasets to fit requirements of statistical methods (see section 5 and Wolff et al. (2015) [86]).

4.2. PV power modeling

In this section, the approach of PV power modeling is described. The reference PV power simulation originally was presented e.g. in Lorenz et al. (2011) [20] and consists of the following steps:

1. modeling the irradiance on plane-of-array I_{POA} of the PV modules, using a global-to-diffuse irradiance and a tilt conversion model,
2. simulating the PV power efficiency based on I_{POA} and the modules' temperature T_m using an empirical model,
3. considering losses in PV power generation by the inverter and other loss mechanisms.

4.2.1. Tilted irradiance modeling

The tilt and orientation of PV modules is fundamental for the irradiance on the plane-of-array I_{POA}. Various models are available to compute I_{POA} (see e.g. [15, 16] for an overview) from global horizontal irradiance I.

In these approaches, the tilt converted beam and diffuse irradiance $I_{POA,b}$ and $I_{POA,d}$ are derived separately. The overall I_{POA} is composed of their contributions and the ground-reflected irradiance $I_{POA,g}$:

$$I_{POA} = I_{POA,b} + I_{POA,d} + I_{POA,g}. \tag{4.1}$$

In a first step, the horizontal diffuse I_d and direct irradiance I_b are modeled from global horizontal irradiance I, using a global horizontal to diffuse or -direct irradiance conversion model. In the analysis presented here, four different state-of-the-art models (see table 4.1) were chosen for comparison. These models derive either the diffuse ratio d of diffuse irradiance I_d and global horizontal irradiance I, defined as

$$d = \frac{I_d}{I} \tag{4.2}$$

or the direct irradiance ratio $(1 - d)$. All models depend on a parametrization of the conversion process and utilize different parameters, as listed in table 4.1. All models listed utilize the clearness index k_t and sun elevation h for parameterization. Additionally, other parameters are used to a varying extent, e.g. the pressure at surface p or the clear sky index k^*. Also, in current models, information on the variability var of k_t is included. This enables to derive statistical information on the characteristics of clouds in the PV systems' field of view, having an influence on the diffuse ratio.

Modeling the tilted diffuse irradiance $I_{POA,d}$ is a rather complex process due to anisotropic effects in the atmosphere. This conversion is a major subject of several POA conversion models. See for example [15, 16] for thorough comparisons of different models. In following evaluations, two state-of-the-art models and a basic reference model (see table 4.1) are compared. These models also include the conversion of the direct horizontal irradiance to direct irradiance on the plane-of-array $I_{POA,dir}$, with the geometric equation:

$$I_{POA,dir} = \frac{cos\Theta}{cos\theta_z} I_b \tag{4.3}$$

with the solar zenith angle θ_z and the angle of incidence Θ. The irradiance $I_{POA,r}$ reflected by the ground is calculated determined by the ground albedo ρ and the tilt angle β:

Table 4.1.: Diffuse irradiance conversion and tilt conversion models. Parameterizations for the diffuse conversion models are based on the clearness index k_t, sun elevation h, pressure p, clear sky index k^*, or the variability of k_t.

Diffuse irradiance model	**parameters**
Skartveit-Olseth 1987 (SkO187) [87]	k_t, h
Skartveit-Olseth-Tuft 1998 (SkOlT98) [88]	k_t, h, var(k_t)
Perez et al.1992 (Perez92) [89]	k_t, h, p, var(k_t)
Perez et al.2002 (Perez02) [90]	k_t, h, p, k^*, var(k_t)

Tilt conversion model
Klucher 1979 [91]
Perez 1987 [92]
isotropic model [93]

$$I_{POA,r} = \frac{1}{2} I \rho (1 - cos\beta) \tag{4.4}$$

In this case, $\rho = 0.2$ (dark-colored surface) is chosen constant, as no further information is available and the impact of changes in ground surfaces on $I_{POA,r}$ is rather small except for snow-covered areas [94].

Comparison of diffuse models

In order to identify a suitable diffuse model for application in PV power forecasting for Germany, a selection of state-of-the-art models (table 4.1) are compared in this section. Here, an evaluation is given based on measurements of I_d at stations of the meteorological sites set 3 (fig. 3.4 of section 3.6). An comparable analysis of the POA-conversion models was not realized, as measurements of I_{POA} were not available in same density and quality as for diffuse irradiance.

The diffuse irradiance models are applied to two sources of global horizontal irradiance data: i) measurements I_{meas} at each station and ii) satellite derived irradiances I_{sat}. The dataset comprises measurements from January to December 2012, with a temporal resolution of 1 hour. A quality check of the measurements for data availability and for consistency of I_{meas} and $I_{meas,d}$ was performed.

Results of the evaluation are shown in figure 4.3 for the nrmse and nbias of diffuse irradiance I_d for single site evaluations. The normalized rmse values vary in a comparatively small range from 25% to 31% for measurement-based diffuse modeling, with Skartveit-Olseth-Tuft'98 showing best results. Differences between the diffuse models' performance are even less noticeable in the I_{sat} dataset, with rmse values spanning 29.5% to 32%. Here, the bias of the satellite derived global horizontal irradiance compensates partially the diffuse models' bias.

The error for modeling the diffuse ratio d based on measured irradiance I, compared to measured $d = I_{meas,d}/I_{meas}$ are shown in the left panel of fig. 4.4: The rmse of the

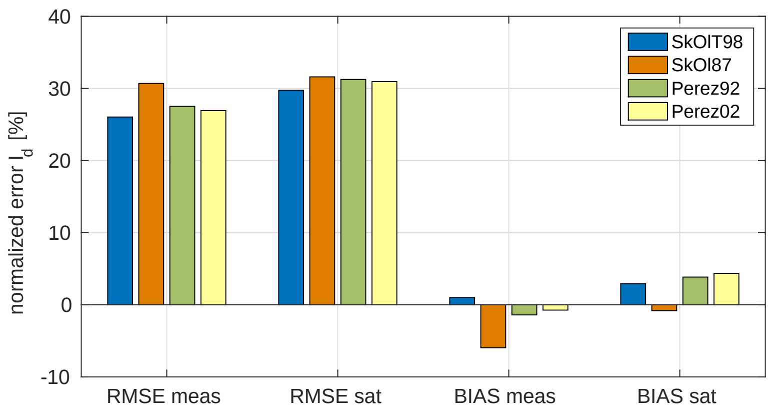

Figure 4.3.: Evaluation of diffuse models of table 4.1 in terms of rmse and bias for the year 2012 with respect to the diffuse irradiance I_d. The diffuse models were applied to I_{meas} and satellite derived irradiance I_{sat}. Dataset: Jan–Dec 2012, 32 sites, 1 hour resolution.

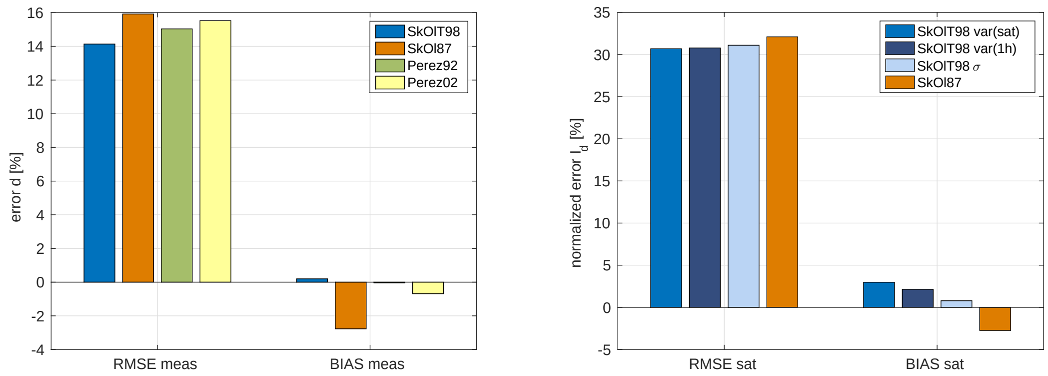

Figure 4.4.: Left: Evaluation of different diffuse models of table 4.1 in terms of rmse and bias with respect to the diffuse ratio d, based on measured irradiance. Right: Comparison of different realizations of variability information derived from satellite data on the rmse and bias of modeled diffuse irradiance I_d. Dataset: Jan–Dec 2012, 32 sites, 1 hour resolution.

different models applied is between 14% and 16%. The relative differences of the error for the models compared are similar to the differences in fig. 4.3. Only the Perez92 shows better performance than Perez02, opposite to results of the evaluation of I_d. This opposing behavior for evaluations of d to evaluations of I_d is caused by a dependency of the modeling error for d on different levels of irradiance. While the models are optimized to describe the diffuse ratio d accurately, the error of I_d is of higher interest for the application in forecasting.

In general, models utilizing a description of the variability (all except the 'SkOl87' model) show better results in this evaluation. For measurement-based I_d, the variability information can also be gained directly from measurements. In fig. 4.4 different approaches for assessing the variability information from satellite data are compared for the 'SkOlT98' model, with i) $var(sat) = std(k_t^{3\times 2px})$: using the standard deviation of k_t for a 3×2 pixels area around the sites' pixel, ii) $var(1h) = std(k_t^{t\pm 1})$ the temporal variability of k_t of $\Delta t = \pm 1 hour$ or iii) variability index $\sigma = |k_t - k_t^{\pm 1}|$, according to the definition in Skartveit, Olseth and Tuft (1998) [88], with $k_t^{\pm 1}$ a modified clearness index of the preceding and following hour. The errors of modeling I_d based on satellite derived irradiance for the 'SkOlT98'-model are displayed. The rmse of the 'SkOl87'-model without variability information included is displayed for reference purpose. Best results with only slight difference are observed for case i), with an nrmse of 30.8% and a nbias of 3%. This configuration is used for the comparison in fig. 4.3. Using less accurate variability information, as for case iii) or when being derived from forecasts, can lead to a compensation of the advantage towards over models not considering the variability (see the 'SkOl87'-model in fig. 4.4).

By this analysis, the influence of the choice of the diffuse model on PV power simulation is expected to be small, when based on satellite derived irradiance or forecasts. In section 4.4 a sensitivity study is presented, showing the impact of diffuse model selection on the accuracy of the overall PV power simulation, also in combination with different POA-conversion models.

4.2.2. PV efficiency model

The simulation of PV power efficiency is done using the model of Beyer et al. (2004) [95], taking plane-of-array irradiance I_{POA} and ambient temperature T_a into account. First, the irradiance dependent efficiency with an assumed constant module temperature of $T_m = 25°C$ is calculated using a three-parameter model:

$$\eta_{MPP}(I_t, T = 25°C) = a_1 + a_2\ I_{POA} + a_3\ log\ I_{POA} \tag{4.5}$$

with $a_{1,2,3}$ empirical device specific parameters. The temperature dependent efficiency at temperatures deviating from $T_m = 25°C$ is considered in a second step:

$$\eta_{MPP}(I_t, T_m) = \eta_{MPP}(I_t, T_m = 25°C)(1 + \alpha(T_m - 25°C)) \tag{4.6}$$

where α the module type dependent temperature coefficient. The modules' temperature T_m is calculated as follows:

$$T_m = T_a + \gamma\ I_{POA} \tag{4.7}$$

with T_a the ambient temperature. The parameter γ is determined by the mounting type of the PV system: E.g. roof integrated PV modules show a different temperature behavior than standalone PV systems.

The overall DC power output then is calculated via:

$$P_{DC} = \frac{\eta_{MPP}(I_t, T_m)}{\eta_{STC}} \frac{I_{POA}}{1000\frac{W}{m^2}} P_{inst} \tag{4.8}$$

The efficiency η_{STC} at Standard Test Conditions (STC) is directly derived from equation 4.5 with $I_t = 1000\frac{W}{m^2}$. I_{POA} and T_m are derived from the corresponding irradiance or temperature forecasts or measurements.

To include the losses by DC to AC conversion and by other loss mechanisms, the AC power output P_{AC} is given by

$$P_{AC} = P_{DC}\ \eta_{inv}(r, v)\ \eta_{losses} \tag{4.9}$$

The efficiency of the inverter η_{inv} is given by the inverter model of Schmidt and Sauer (1996) [96] using system dependent parameters r_{loss}, v_{loss}. This efficiency η_{inv} is modeled taking into account different sources for losses within the inverter, like voltage losses, self-consumption and ohmic losses, each represented by a specific factor. Other losses like the influence of reflection or spectral effects at the modules, ohmic cable losses or mismatches of modules within a PV plant are represented by the efficiency η_{losses} [20].

4.2.3. Parameter configuration and model variation

Two different variations of the parameter set used in the presented PV power efficiency model are compared to a simple reference model, as introduced in the following:

- **Empirical parameter set** In this approach, a fixed parameter set was chosen representing typical PV modules [20] based on an evaluation of a huge dataset of systems of *meteocontrol GmbH*. There, a_i and α are kept constant for all sites, as more precise individual station information were not available. The parameter γ was estimated from installed capacity of the system: Large plants tend to be freely mounted, whereas smaller plants usually are roof-top mounted.

Table 4.2.: Parameters used in the PV power simulation model introduced in section 4.2.2.

$a_{1,2,3}$	parameter of Beyer et al. (2004) model [95], characterising the irradiance dependent efficiency $\eta_{MPP}(I_t, T = 25°C)$
γ	parameter characterizing the influence of POA irradiance on the modules' temperature T_m
α	parameter characterizing the influence of modules' temperature T_m on PV power efficiency $\eta_{MPP}(I_t, T_m)$
r_{loss}, v_{loss}	parameters of inverter model by Schmidt and Sauer (1996) [96]
η_{losses}	additional losses caused by reflection, cable resistance etc.

- **Parameter fitted to historical data** As model parameters for each PV system are not available, parameters are fitted to historical data. The standard PV efficiency model is simplified in favor of a better adaptation of the model parameters: Inverter losses $\eta_{inverter}$ are assumed to be constant and are combined with the other losses η_{system}, so the AC power P_{AC} is modeled with P_{DC} from equation 4.8:

$$P_{AC} = P_{DC}\ \eta_{system} \tag{4.10}$$

The remaining parameters a_i, α, γ and η_{system} were fitted to a training dataset. This consists of satellite derived irradiance I_{sat}, ECMWF ambient temperature forecasts $T_{a,NWP}$ and PV power measurement data P_{meas}. The months April to September 2012 were taken into account, situations with incident angles higher than 60° and solar zenith angles $\theta_Z > 80°$ were neglected. A common two-dimensional least-square algorithm was applied and the parameters were limited to a reasonable range around the empirical parameters. Figure 4.5 displays the resulting fitted curves for $\eta_{MPP}(I_t, T_m)/\eta_{STC}$ for all sites. This array of curves is compared against the equivalent curve for the non-fitted empirical model, for the temperature independent case (assuming $T_m = 25°$) and the temperature dependent case (with fixed ambient temperature $T_a = 15°$). By fitting all parameters, also site specific features of the relationship between irradiance, temperature and PV power output

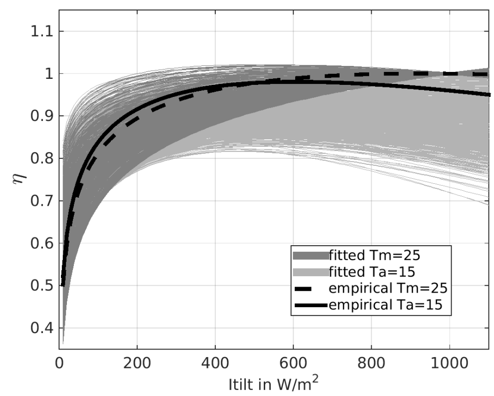

Figure 4.5.: Fitted efficiency curves compared with curves from empirical dataset, for temperature independent case (module temperature $T_m = 25°$) and temperature dependent case (ambient temperature $T_a = 15°$).

are reflected and included. The influence of the temperature is visible by a decline of efficiency for high levels of irradiance, as for $T_m > 25°C$ the efficiency of PV system decreases significantly.

- **Linear PV efficiency model** Following the concept of comparing to a trivial reference models, a simple approach for irradiance to PV power conversion was additionally applied and compared to. Here PV power output is assumed to be linear with I_{POA}, following the equation

$$P_{AC} = \lambda \, I_{POA}. \tag{4.11}$$

The parameter λ was fitted for each station individually, using the same dataset as in section 4.2.3 with same restrictions to solar zenith angles and incidence angles Θ as mentioned above. This approach completely neglects the temperature dependent behavior as well as the non-linearity of PV power efficiency.

4.2.4. Linear regression with daily updated PV power measurements

A linear regression procedure is applied in order to achieve ongoing adaption of forecasts to PV power measurements by a statistical post-processing. This is done based on daily updated PV power measurements and corresponding PV power forecasts of the preceding days for each system individually, and for each forecasting method and horizon separately. By this, an adaption of the PV power forecasts to the seasonal meteorological conditions of a period close to the forecast computation time is performed. The linear regression coefficients a and b, as introduced by the equation

$$P_{AC}^{lr} = a \cdot P_{AC} + b \tag{4.12}$$

with P_{AC}^{lr} the corrected PV power output based on simulated power output P_{AC}, are determined by a least-square-fit with PV power measurements.

The optimal length of the training period for coefficients a and b is determined by the Improvement Score $IS(P_{sat}^{lr}, P_{sat})$: The satellite-based PV power P_{sat}^{lr} with linear regression ('lr') applied is compared to P_{sat} without linear regression. In figure 4.6, the

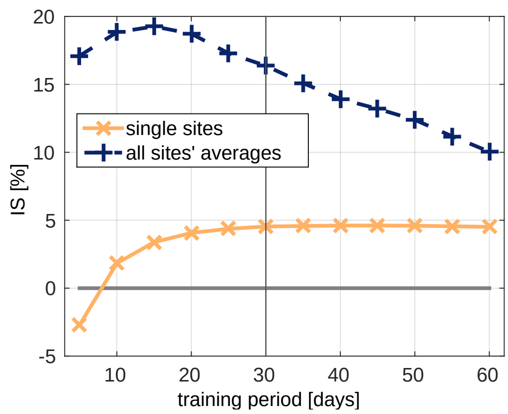

Figure 4.6.: Improvement score $IS(P_{sat}^{lr}, P_{sat})$ in dependence on training period for satellite-based PV power simulation by the empirical approach Dataset: Apr–Nov 2012, 1196 sites, 15 min resolution.

$IS(P^{lr}_{sat}, P_{sat})$ is displayed depending on the amount of preceding training days, with empirical parameter set and temperature T_{NWP}. For single sites a good adaption is found for 30 days with only little improvements for longer periods. For all sites' averages a training period of 15 days shows best results. In further evaluations a common training period of 30 days is chosen.

4.3. Forecasts of ambient temperature

The PV power efficiency model according to equation 4.6 requires modeling the PV modules' temperature T_m. This temperature T_m is mainly depending on the plane-of-array irradiance I_{POA} and the ambient temperature T_a. In this section, evaluations of NWP forecasts of ambient temperature T_a are presented as well as of temperature information gathered from monthly mean climatology, used for reference purpose. The impact of using either of them in PV power prediction is picked up in section 4.4. Evaluations given in this section are based on measurements of ambient temperature at the meteorological stations set 3 (see section 3.6). Only daytime values, defined by the clear sky irradiance $I_{clear} > 0\ W/m^2$ at the corresponding site, are considered.

4.3.1. NWP temperature forecasts

Forecasts of ambient temperature are retrieved from the ECMWF IFS and from the DWD COSMO-EU (see section 3.4) models. To derive spatially and temporally allocated forecasts, the nearest grid point and a linear temporal interpolation procedure is used. A frequency scatter plot of ECMWF forecasts interpolated to a hourly resolution is shown in the left panel of fig. 4.7. Compared to the scatter plot for single site irradiance forecasts (left panel of fig. 3.5), the scatter is comparatively small, showing a good agreement of temperature forecasts and measurements. The frequency distribution shows two peaks for measurements and forecasts at around $T_a = 16°C$ and at around $T_a = 7°C$.

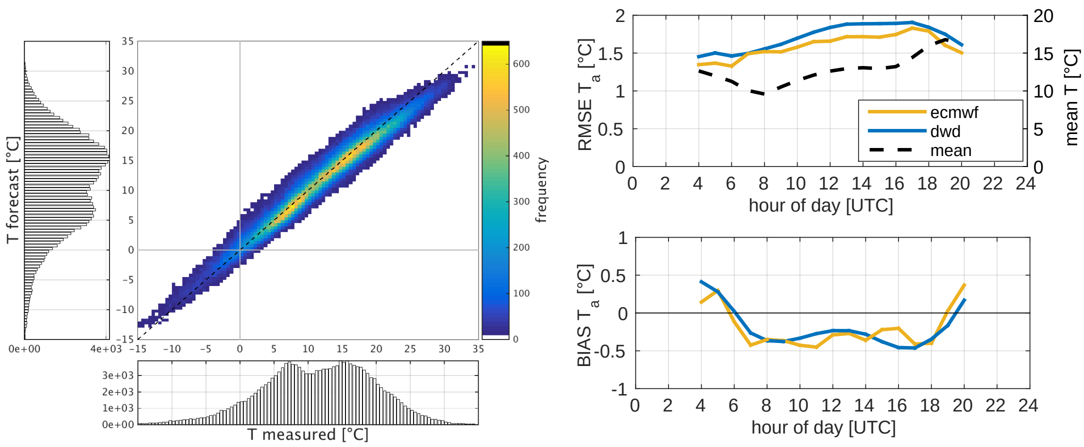

Figure 4.7.: Left: Frequency scatter plot of ECMWF intraday temperature forecasts vs ambient temperature measurements. Right: Rmse and bias of ECMWF and DWD single-site intraday forecasts of ambient temperature T_a in dependence on the hour of day. Dataset: Jan–Dec 2012, 32 sites, 1 hour resolution, daytime values.

The daytime dependency of rmse and bias for temperature forecasts is displayed in the right panel of fig. 4.7. Alongside, the mean ambient temperature for each hour of the day is displayed. The diurnal course of temperature follows the course of irradiance but with a lag of a few hours. Typically, lowest temperatures are expected shortly before sunrise, highest temperature shortly after noon. In contrast to that, in fig. 4.7 highest temperatures are observed later in the evening and the level of early morning hours is the same as e.g. for noon in this evaluation. This is a consequence of restricting temperature evaluations to day-time values only: By this, temperature of the early morning and later evening hours only occur in summer months when average temperatures are generally higher than in winter. At the same time, temperature evaluations during the day are based on all months of the year, shifting the mean to lower values. For comparison to the evaluation of all-day temperature, refer to fig. A.1 in the appendix. The rmse of temperature forecasts (fig. 4.7, right) follows the course of mean temperature for both models. Also, a consistent underestimation of ambient temperature is observed during the day (from 6 to 19 UTC) for both models similarly, as well as an overestimation for the morning and evening hours.

The dependence of rmse and bias on the month of the year is displayed in fig. 4.8. For temperature forecasts of the ECMWF, rmse values differ between $1.3°C$ and $2°C$ for the different months, for forecasts of the DWD model between $1.6°C$ and $2.5°C$. A slight seasonal trend with higher rmse in summer and lower rmse in winter months can be observed for both models. The DWD shows higher rmse for all months compared to ECMWF forecasts with highest differences in the months January to March and December. The bias of ECMWF forecasts is between $-0.5°C$ and $+0.5°C$ with no significant annual trend. The DWD forecasts show underestimation in winter and overestimation in summer months, overall the bias is between $-1°C$ and $+0.5°C$.

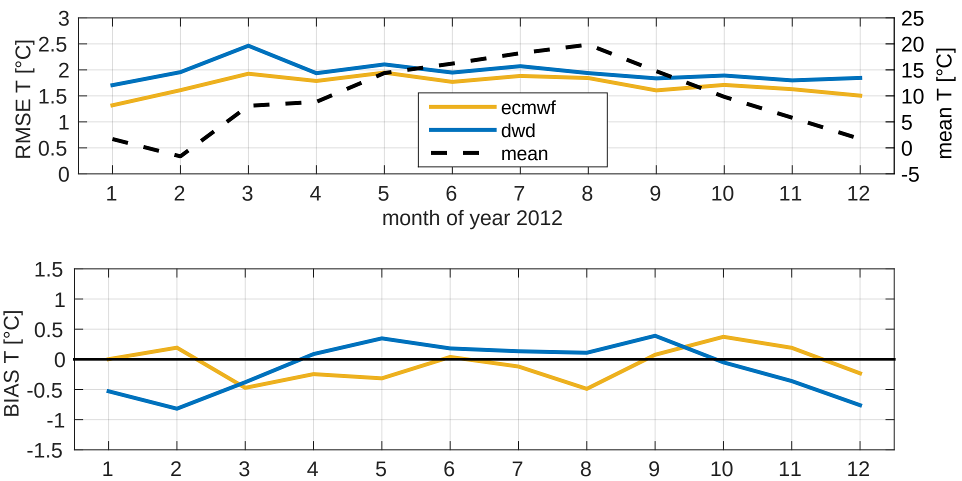

Figure 4.8.: Rmse and bias of ECMWF and DWD single-site intraday forecasts of ambient temperature T_a, in dependence on the month of year 2012. Dataset: Jan–Dec 2012, 32 sites, 1 hour resolution, daytime values.

4.3.2. Climatological mean temperatures

Monthy climatological mean temperature values are used as a reference for the following analysis. These are retrieved from the Climate Atlas Germany (Klimaatlas Deutschland, [97, 98]): There, climatology values were derived using temperature measurements at DWD sites for the year 1980 to 2010 for the months January to December individually. Measurements were interpolated to a 1 km × 1 km grid covering Germany and considering topographic effects (fig. 4.9). In this analysis, the nearest grid points corresponding to the sites evaluated is chosen.

The comparison of the monthly climatological mean to measured ambient temperature T_a is displayed in the left panel of fig. 4.10. The temperature follows a clear annual trend with minimum values in January and maximum values in July. A good representation of mean temperatures as measured for 2012 is visible. But evidently, these monthly mean values are able to represent neither the diurnal temperature dependency nor any specific weather situation. Thus, climatological mean temperature shows a significantly higher rmse between 3.7 and $8°C$ when evaluated on an hourly basis. A systematic underestimation up to $-4°C$ except for February (with bias of $+2.8°C$) is visible.

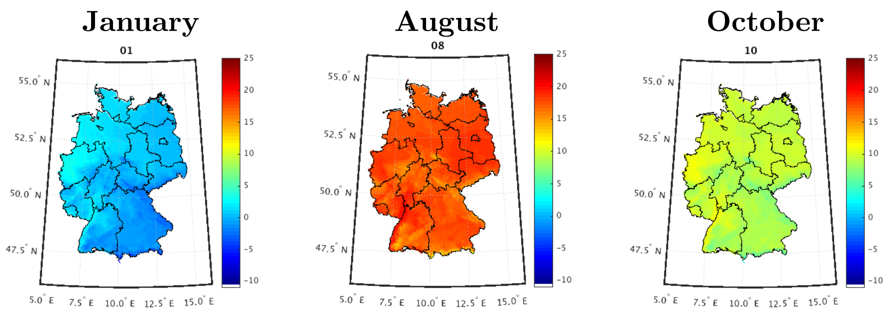

Figure 4.9.: Spatial distribution of mean temperature for three exemplary months, in $°C$. Topographic differences are considered as well as seasonal changes in average temperatures.

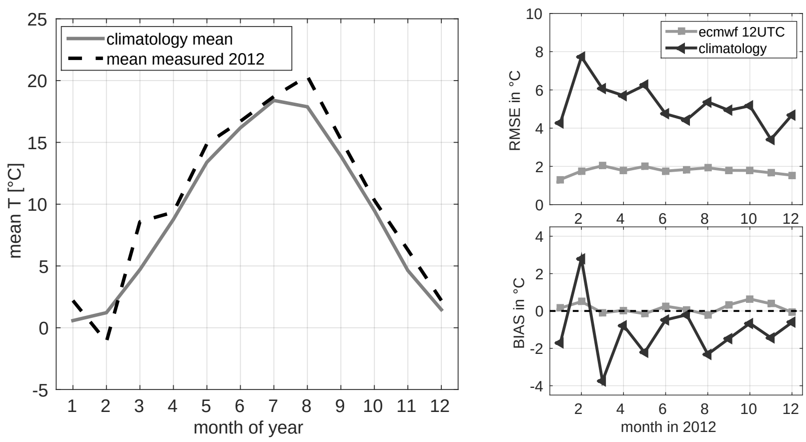

Figure 4.10.: Left: Mean monthly ambient temperature from climatology (based on the Climate Atlas Germany [97]) compared to measured mean temperature for each month of the year 2012. Right: Rmse and bias of climatology data compared to ECMWF intraday forecasts. Dataset: Jan–Dec 2012, 32 sites, 1 hour resolution, daytime values.

4.4. Impact of PV power simulation on forecast accuracy

The accuracy of PV power forecasts is determined by the accuracy of irradiance and temperature forecasts, but also by the models used for irradiance-to-power conversion. Knowledge of parameters describing the behavior of the PV system is an important issue as well as an adequate modeling of the incidence irradiance and the efficiency of the system. Here, focus is explicitly on the irradiance-to-power conversion approach. This is done in order to identify the optimal model configuration, following the scheme in figure 4.11.

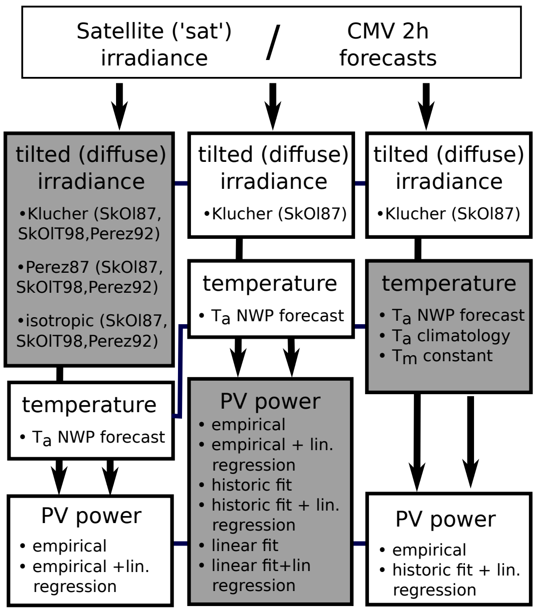

Figure 4.11.: Overview on PV model validation and comparison. In each section (corresponding to one column each), one aspect of PV power simulation is varied, the remaining parts are fixed to one configuration. Left → variation of diffuse and tilted irradiance model (section 4.4.2), center → variation of PV models (section 4.4.3), right → application of different temperature data (section 4.4.4).

The impact of the single modeling steps on the overall PV power efficiency is analyzed with respect to the resulting PV power forecasts in comparison to power measurements (see section 4.1). Presented results are selected from a multiplicity of possible configurations. Variations in each segment are investigated by retaining fixed configurations within the remaining segments. Additionally, validations using meteorological data of irradiance or temperature measurements are provided. The influence of each modeling step is shown for single sites and averaged for all sites to highlight differences with respect to the forecast application. For most steps, the models' performance is compared to trivial references.

In this section, the influence of the different models and configurations on PV power simulation is analyzed with respect to i) diffuse and tilt conversion models (section 4.4.2), ii) PV power simulation models (section 4.4.3), and iii) temperature information dependency (section 4.4.4). Comparisons are done by elaborating the sensitivity of the overall power simulation process towards the changes in models selection and configuration (fig. 4.11).

These are performed for:

- Irradiance derived from satellite data (further denoted as 'sat') and CMV forecasts of 2 hours ahead ('CMV 2h'),
- single sites and all sites' averages, and
- with and without linear regression with PV power measurements applied to PV power forecasts.

4.4.1. Characteristics of single site and spatially averaged PV power forecasts

The CMV 2h forecast error is visualized by frequency distribution scatter plots (fig. 4.12) based on the empirical PV power model for single sites (left) and all sites' average (right). Both, single sites and all sites' averages have high share of data points along the identity line. The scatter for all sites' averages is significantly lower than for single sites average, as it also is valid for irradiance forecasts due to spatial averaging effects. As 15-minute values are evaluated here, single site PV power forecasts are more scattered as irradiance forecasts with 1 hour resolution, as displayed in fig. 3.5, section 3.7).

From the histogram representing the sum of data points at x- and y-axis for each line or column of the frequency distribution scatter, a high share of measurements and forecasts are found within the range of $P/P_{inst} \leq 20\%$ for single sites. Here, the shape of the histogram characterizing the predicted values differs slightly from the shape of the measured ones, showing a small overrating of PV power in this range.

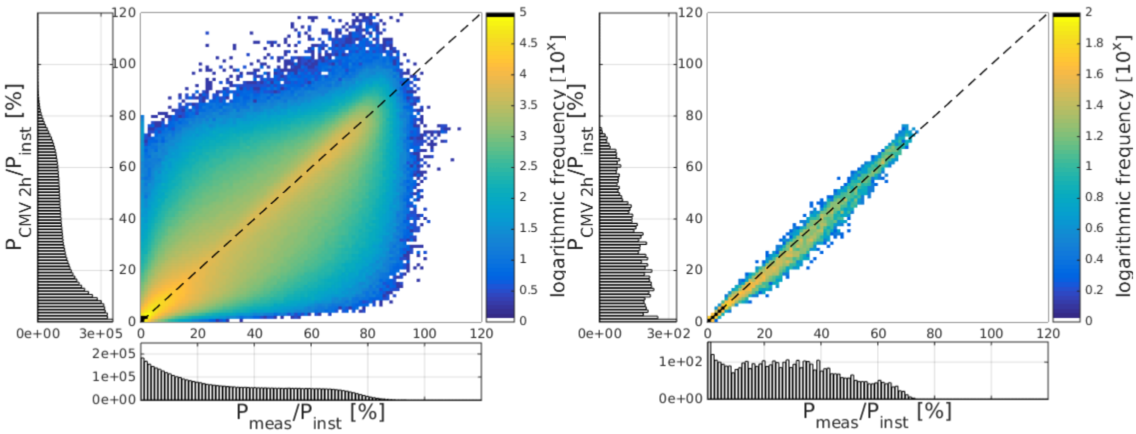

Figure 4.12.: Frequency scatter for CMV 2 hours forecasts for the empirical model, with SkOl87/Klucher tilt conversion modeling and NWP ambient temperature; left for single sites, right for all sites averages. Dataset: Apr–Nov 2012, 1196 sites, 15 min resolution, solar zenith angles $\theta_Z < 80°$.

4.4.2. Diffuse and tilted irradiance models

In this section, three diffuse irradiance models, and two state-of-the-art and one reference tilt conversion models (table 4.1 and left column in figure 4.11) are compared. Error measures, showing the impact on the PV power simulation, for all possible combinations

Table 4.3.: Error measures for different conversion models with a) satellite derived irradiance, b) satellite derived irradiance with linear regression and c) CMV 2 hour forecasts with linear regression applied. Dataset: Apr–Nov 2012, 1196 sites, 15 min resolution, $\theta_Z < 80°$.

a) I_{sat} and $T_{a,NWP}$ → **tilt+diffuse models varied** → empirical model						
	single sites			**all sites' averages**		
tilt conversion + diffuse models	rmse	bias	IS	rmse	bias	IS
Klucher 1979 + SkOl87	9.05	-1.00	0.0 %	2.43	-0.95	0.0 %
Klucher 1979 + SkOlT98	9.09	-1.07	-0.4 %	2.60	-1.01	-7.0 %
Klucher 1979 + Perez92	9.06	-1.02	-0.1 %	2.47	-0.97	-1.6 %
Perez 1987 + SkOl87	9.04	-0.63	0.1 %	2.28	-0.60	6.2 %
Perez 1987 + SkOlT98	9.07	-1.03	-0.2 %	2.52	-0.98	-3.7 %
Perez 1987 + Perez92	9.06	-0.97	-0.1 %	2.41	-0.94	0.8 %
Isotropic + SkOl87	9.24	-1.81	-2.1 %	3.07	-1.74	-26.3 %
Isotropic + SkOlT98	9.31	-1.89	-2.9 %	3.25	-1.81	-33.7 %
Isotropic + Perez92	9.25	-1.84	-2.2 %	3.09	-1.76	-27.2 %

b) I_{sat} and $T_{a,NWP}$ → **tilt+diffuse models varied** → empirical model + linear regression						
	single sites			**all sites' averages**		
tilt conversion + diffuse models	rmse	bias	IS	rmse	bias	IS
Klucher 1979 + SkOl87	8.60	0.18	0.0 %	1.61	0.15	0.0 %
Klucher 1979 + SkOlT98	8.47	0.12	1.5 %	1.43	0.11	11.2 %
Klucher 1979 + Perez92	8.48	0.11	1.4 %	1.42	0.11	11.8 %
Perez 1987 + SkOl87	8.60	0.14	0.0 %	1.61	0.11	0.0 %
Perez 1987 + SkOlT98	8.47	0.12	1.5 %	1.44	0.10	10.6 %
Perez 1987 + Perez92	8.51	0.12	1.1 %	1.44	0.11	10.6 %
Isotropic + SkOl87	8.62	0.10	-0.2%	1.61	0.12	0.0 %
Isotropic + SkOlT98	8.46	0.09	1.6 %	1.42	0.08	11.8 %
Isotropic + Perez92	8.47	0.09	1.5 %	1.40	0.10	13.0 %

c) $I_{CMV,2h}$ and $T_{a,NWP}$ → **tilt+diffuse models varied** → empirical model + linear regression						
	single sites			**all sites' averages**		
tilt conversion + diffuse models	rmse	bias	IS	rmse	bias	IS
Klucher 1979 + SkOl87	12.63	0.40	0.0 %	3.35	0.20	0.0 %
Klucher 1979 + SkOlT98	12.66	0.42	-0.2 %	3.34	0.18	0.3 %
Klucher 1979 + Perez92	12.62	0.38	0.1 %	3.32	0.23	0.9 %
Perez 1987 + SkOl87	12.64	0.37	-0.1 %	3.36	0.19	-0.3 %
Perez 1987 + SkOlT98	12.65	0.39	-0.2 %	3.35	0.17	0.0 %
Perez 1987 + Perez92	12.66	0.39	-0.2 %	3.35	0.18	0.0 %
Isotropic + SkOl87	12.59	0.31	0.3 %	3.34	0.16	0.3 %
Isotropic + SkOlT98	12.61	0.33	0.2 %	3.32	0.14	0.9 %
Isotropic + Perez92	12.65	0.26	-0.2 %	3.36	0.20	-0.3 %

of the named models are displayed in tables 4.3 (a-c). The Improvement Score IS is given with respect to the Skartveit-Olseth87 and Klucher79 (highlighted in grey) models. The PV power simulation is done by the empirical model, with satellite-based irradiance or CMV 2h forecasts as irradiance input, and with and without linear regression 'lr' applied.

The PV power modeling based on satellite data without linear regression (table 4.3a), shows little sensitivity to the selection of the diffuse and tilted irradiance model for single site evaluation, as expected from results in section 4.2.1. Here the range of the IS measure covers values between -2.9% and 0.1%. Highest rmse is found for the isotropic model, which also shows the highest bias among the compared models. For averaged site evaluations, larger differences are found with the IS between -33.7% and $+6.2\%$, or without considering the isotropic model, between -7.0% and $+6.2\%$.

The application of the linear regression 'lr' model, (table 4.3 b), in general leads to a reduction of rmse and bias. By the linear regression applied, the bias is reduced and the amplitude of the predicted time series is adapted to measured time series. This is observed to varying extents for the models compared: The IS for the different diffuse models shows an improvement when applying the SkOlT98 or Perez92 model instead of the SkOl87, as is expected from the measurement-based evaluations in section 4.2.1. For each diffuse model, all tilt conversion models lead to comparable results, with around 0.4% spread of the IS for single sites and around 1.2% for averaged sites. Remarkably, with linear regression applied, the isotropic model leads to results similar to or better than both state-of-the-art models. Applying the 'lr' thus leads to a correction of systematic differences among the models and leads a smaller impact of the tilt models' performance. Same is valid for the diffuse models, except for the SkOl87 model which benefits less from linear regression applied.

The application of the model comparison to PV power forecasts is shown exemplary for the 2 hours CMV forecasts with linear regression applied (table 4.3c). Differences between the diffuse and tilt model combinations level out almost completely as the impact of forecast errors of irradiance I gets more dominant and the already small differences in models performance gets less pronounced. The IS measure varies between -0.3% and $+0.9\%$ for single sites and all sites' averages. Also the bias error shows little variation among the model combinations.

This behavior shows that presented PV power modeling for forecast application is rather insensitive to the selection of diffuse and tilted irradiance conversion models, especially when an adaption to measurement is realized. Effects in general are much higher for regional forecasts than for single sites. These results for CMV forecasts are consistent with the findings in Pelland et al (2011) [16] for NWP-based forecasts. For the PV power prediction presented in this paper, the Skartveit-Olseth87 diffuse and the Klucher79 tilt conversion model are chosen.

4.4.3. PV power modeling

In this section, the PV power simulation models as described in section 4.2.2 are compared (see figure 4.11, centre column) with respect to the impact on the overall PV power simulation accuracy for the application in forecasting. This enables to derive statements on the impact of using an model based on a standard parameter set ('empirical model') versus a parameter set adapted to measurements ('historic fit model'). These models are also compared to a trivial reference ('linear reference model'). Each variant is presented with additional linear regression ('lr') applied as described in section 4.2.4 to demonstrate the impact of training to daily updated measurements. The Improvement Score refers to the highlighted 'historic fit model' for the following evaluations. In analogy to the section above, satellite-based irradiances and 2 hours' CMV forecasts as well as ECMWF intraday temperature forecasts are used in the evaluated PV power simulations.

The effect of employing the historical fit data is compared to the empirical model for 200 single sites randomly selected from the dataset (fig. 4.13), evaluated based on the satellite derived PV power P_{sat} and sorted by the corresponding rmse or bias for the historic fit model. This historic fit model shows generally lower rmse than the empirical model for all single sites displayed, with only few exceptions. Also, the bias error indicates an improvement concerning systematic deviations by the historic fit approach.

Scatter plots of P_{sat}/P_{inst} for all sites' averages, for the historic fit and the simple linear model are displayed in the left panel of fig. 4.14. There, the linear model shows significant overestimation at $P/P_{inst} > 50\%$ and a slight underestimation at intermediate values for P/P_{inst}. This is a direct consequence of not considering the non-linearity of the PV power efficiency and neglecting the impact of module temperature in the simple approach. However, th scatter for both variants shows about the same scale.

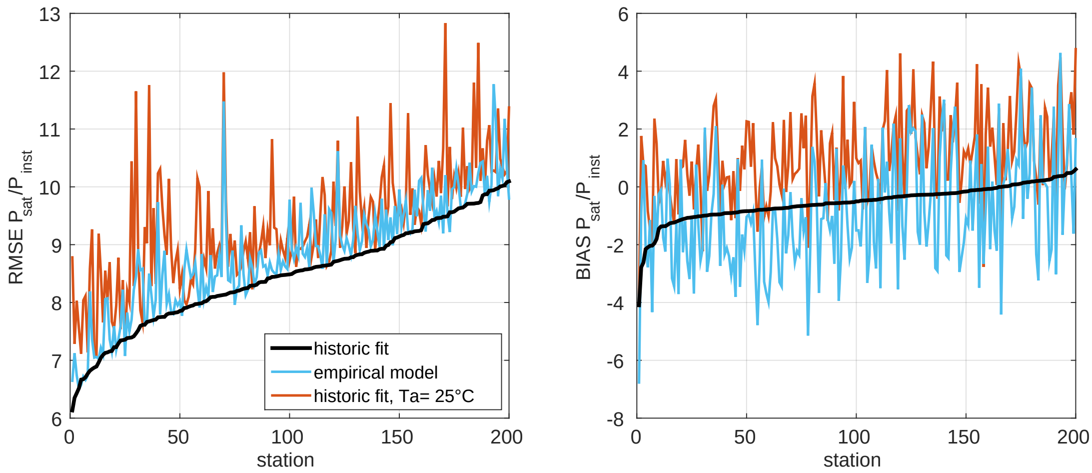

Figure 4.13.: Comparison of the empirical PV model with i) the historic fit model and ii) the empirical model without impact of temperature for satellite-based PV power P_{sat}, for 200 PV sites, randomly selected and sorted by corresponding error measures, for rmse and bias individually. Dataset: Apr–Nov 2013, 200 sites, 15 min resolution, $\theta_Z < 80°$.

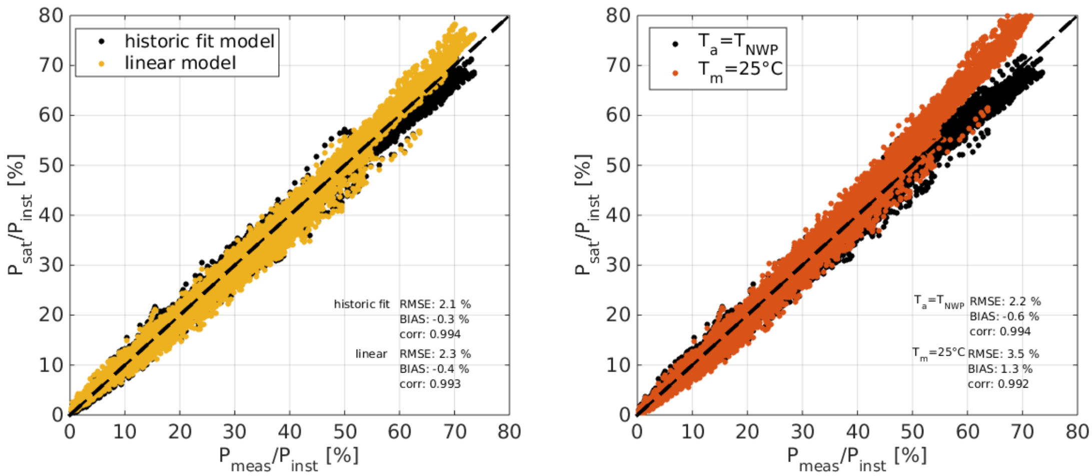

Figure 4.14.: Satellite-based PV power P_{sat} for all sites average versus PV power measurements P_{meas} for two different PV simulation models (left, historic fit and linear model) and different temperature information (right, with T_a from NWP or $T_m = 25°C$). Dataset: Apr–Nov 2013, 200 sites, 15 min resolution, $\theta_Z < 80°$.

The impact of the different models applied is summarized in table 4.4. In general, lowest rmse for the 'historic fit'-PV model are shown there. The remaining approaches show negative IS compared to that, but to a different extent depending on the configuration: For single sites, the advantage of the 'historic fit'-model is notably low, valid for satellite derived irradiance (up to $IS = -3.8\%$) and CMV 2 hours forecasts (up to $IS = -3.1\%$). The linear model fitted to historic data leads to lower rmse values than the more complex empirical model, which is not adapted to historic measurements ($IS = -0.3\%$ for satellite derived irradiance and $IS = -1.2\%$ for CMV 2h forecasts). For averaged forecasts, the models' impact on PV simulation is more prominent: For satellite derived irradiance it is up to $IS = -9.4\%$ for the linear model (see also fig. 4.14, left) and $IS = -1.4\%$ for the empirical model; for CMV forecasts $IS = -13.8\%$ for the linear and up to $IS = 22.6\%$ for the empirical model.

When applying the linear regression approach, the overall rmse decreases for all variants displayed. With this adaption to recent measurements applied, the PV power simulation shows less sensitivity to the applied model configuration, especially true for the CMV 2 hours' forecasts. For satellite-based PV power simulation, the IS ranges up to -0.7% for single sites, and -5.5% for all sites' averages, for CMV 2 hours forecasts up to -0.2% (single sites) and -1.4% (averages). According to that, the application of a more complex model fitted to historical data does not necessarily lead to improvements in PV power forecasting. Much more important is the adaption to recent measurements, making the benefit of parameter fitting to historic measurements insignificant. In the following evaluations, the model fitted to historical data with linear regression is used.

Table 4.4.: Rmse, bias and IS for combinations of different PV models with a) satellite derived irradiance without linear regression, and b) with linear regression; c) CMV 2 hour forecasts without and d) with linear regression applied.

a) I_{sat} and $T_{a,NWP}$ → Klucher79 + SkOl87 → **PV model varied**						
	single sites			all sites average		
error [%]	rmse	bias	IS	rmse	bias	IS
empirical model	9.02	-0.66	-3.8%	2.15	-0.56	-1.4 %
fitted to historical data	8.69	-0.36	0.0 %	2.12	-0.31	0.0 %
linear reference model	8.72	-0.42	-0.3 %	2.32	-0.38	-9.4 %

b) I_{sat} and $T_{a,NWP}$ → Klucher79 + SkOl87 → **PV model varied + linear regression**						
	single sites			all sites average		
error [%]	rmse	bias	IS	rmse	bias	IS
empirical model	8.60	0.00	-0.7 %	1.87	0.04	-2.7 %
fitted to historical data	8.54	0.00	0.0 %	1.82	0.03	0.0 %
linear reference model	8.57	0.09	-0.4 %	1.92	0.11	-5.5 %

c) $I_{CMV,2h}$ and $T_{a,NWP}$ → Klucher79 + SkOl87 → **PV model varied**						
	single sites			all sites average		
error [%]	rmse	bias	IS	rmse	bias	IS
empirical model	12.04	-2.50	-3.1%	3.90	-2.40	-22.6 %
fitted to historical data	11.68	-1.58	0.0 %	3.18	-1.09	0.0 %
linear reference model	11.82	-1.24	-1.2%	3.62	-1.20	-13.8 %

d) $I_{CMV,2h}$ and $T_{a,NWP}$ → Klucher79 + SkOl87 → **PV model varied + linear regression**						
	single sites			all sites average		
error [%]	rmse	bias	IS	rmse	bias	IS
empirical model	11.55	0.05	0.0 %	2.90	0.08	0.0 %
fitted to historical data	11.55	0.07	0.0 %	2.90	0.10	0.0 %
linear reference model	11.57	0.16	-0.2 %	2.94	0.19	-1.4 %

4.4.4. Temperature modeling

In this section a quantification of the impact of temperature information on PV power forecasting (fig. 4.11, right column) is given. The module temperature T_m was considered with equation 4.6 of the PV efficiency model, using ECMWF temperature forecasts T_{NWP} (see section 4.3) as input for the ambient temperature T_a. This is compared to simulations using information on T_a from climatology T_{clim} (see section 4.3.2) or neglecting temperature information by assuming $T_m = 25°C$. The parameters of the historic fit were trained for each case separately with the appropriate input dataset. All variants are compared to $T_a = T_{NWP}$ as the highlighted reference.

The effect of choosing a fixed model temperature of $T_m = 25°C$ is displayed in fig. 4.13, compared to the same model but with temperature information from NWP forecasts. In general, with $T_m = 25°C$, an systematic overestimation of the PV power is induced. This is mainly the consequence of not considering heating losses in PV power efficiency modeling by neglecting temperature information. PV efficiency is reduced in case of high temperature, which mainly occur at high levels of irradiance. Same effect is visible in right panel of fig. 4.14, showing the impact of different temperature information on the PV power forecasts for all sites averages. A strong positive bias at high PV power feed-in of 50% and above is visible. For low irradiance and temperature levels an underrating of PV power observed, visible at $P/P_{inst} < 25\%$, but to a much smaller extent than the overrating at high irradiances. This is due to the fact, that the PV power efficiency gain at low module temperatures T_m is modeled correctly with this assumption. When applying T_a from NWP, a good agreement between simulated and measured PV power is prevalent.

According to table 4.5, the replacement of temperature forecast information by monthly mean climatology values shows little effects for single site power simulations when applied to the empirical model without linear regression applied. The decline in forecast accuracies amounts up to $IS = -0.2\%$ for satellite derived irradiance and $IS = +0.2\%$ for CMV 2h forecasts. The impact is stronger for all sites averages, with $IS = -8.5\%$ for single sites and $IS = -1.0\%$ for CMV 2h forecasts. When assuming $T_m = 25°C$ the temperature impact is much higher and amounts to as much as $IS = -60.9\%$ for satellite-based irradiance. For CMV 2h forecasts, the positive bias partially compensates for the negative bias of PV power forecasts, indicating a lower impact of varying the temperature input.

When applying a best fit model (historic fit with linear regression applied) this impact on bias and therefore the importance of temperature information lessens. For single sites, for $T_m = 25°C$ the IS is reduced from $IS = -5.5\%$ to $IS = -0.5\%$, for all sites' averages from -60.9% to $IS = -6.0\%$. For CMV 2 hours' forecasts the impact of temperature information decreases further and is only leading to maximum negative IS of -0.3% for single sites and -1.4% for all sites' averages. The use of climatology data here shows slightly higher rmse as for the $T_m = 25°C$ assumption when linear regression applied.

In summary, the impact of temperature information is higher for satellite-based irradiance than for CMV forecasts. Neglecting the impact of changing modules' temperature has a high impact on PV power modeling accuracies, especially for all sites averages. These can be partly compensated for by applying the linear regression approach. Still,

Table 4.5.: Rmse, bias and IS for combinations of different temperature information with a) satellite derived irradiance and empirical PV model b) CMV 2 hour forecasts and empirical PV model, c) and d) satellite derived irradiance / CMV 2 hour forecasts with historically fit model and linear regression applied. Dataset: Apr–Nov 2013, 1196 sites, 15 min resolution, $\theta_Z < 80°$.

a) I_{sat} + **T varied** → Klucher79 + SkOl87 → empirical model						
	single sites			all sites average		
error [%]	rmse	bias	IS	rmse	bias	IS
$T_a = T_{NWP}$	9.02	-0.66	0.0 %	2.15	-0.56	0.0 %
$T_m = 25°$	9.52	1.32	-5.5 %	3.46	1.25	-60.9 %
$T_a = T_{climatology}$	9.04	-0.98	-0.2 %	2.33	-0.88	-8.4 %

b) $I_{CMV,2h}$ + **T varied** → Klucher79 + SkOl87 → empirical model						
	single sites			all sites average		
error [%]	rmse	bias	IS	rmse	bias	IS
$T_a = T_{NWP}$	12.04	-2.50	0.0 %	3.90	-2.40	0.0 %
$T_m = 25°$	12.43	-0.07	-3.2 %	4.24	-0.01	-8.7 %
$T_a = T_{climatology}$	12.02	-1.79	0.2 %	3.94	-1.73	-1.0 %

c) I_{sat} + **T varied** → Klucher79 + SkOl87 → historical fit model + linear regression						
	single sites			all sites average		
error [%]	rmse	bias	IS	rmse	bias	IS
$T_a = T_{NWP}$	8.54	0.00	0.0 %	1.82	0.03	0.0 %
$T_m = 25°$	8.57	0.09	-0.4 %	1.92	0.11	-5.5 %
$T_a = T_{climatology}$	8.58	0.06	-0.5 %	1.93	0.09	-6.0 %

d)$I_{CMV,2h}$ + **T varied** → Klucher79 + SkOl87 → historical fit model + linear regression						
	single sites			all sites average		
error [%]	rmse	bias	IS	rmse	bias	IS
$T_a = T_{NWP}$	11.55	0.07	0.0 %	2.90	0.10	0.0 %
$T_m = 25°$	11.57	0.15	-0.2 %	2.93	0.17	-1.0 %
$T_a = T_{climatology}$	11.58	0.12	-0.3 %	2.94	0.15	-1.4 %

using temperature forecasts shows best results in all considered configuration and is included in PV power forecasting. Being already of high forecast quality (see section 4.3) and showing little impact on the overall PV power accuracy, temperature forecasts are not subject to research for further improvements in this context.

4.4.5. Summary

The discussion above shows a weak influence of the chosen diffuse and tilt conversion model on the overall PV power simulation for the application to PV power forecasting. Also the selection of the PV efficiency model configuration has only a small influence, when an adaption of forecasts to PV power measurement is possible. The impact of using low-level temperature information has a high impact especially for averaged forecasts. However, this can also be reduced when adapted to measurements, as it has been demonstrated with a simple linear regression approach.

Conclusions drawn are only valid for the described application to PV power forecasting, where forecasts of global horizontal irradiance show the largest impact on PV power forecast accuracy. Statements which are made especially refer to this specific application of the PV power simulation model to forecasting. For other applications such as PV site assessment, a different conclusion can be drawn when system information and measured irradiance or temperature is available in more detail. In any case, the forecast accuracy has been improved most when an adaption to daily updated measurement is implemented, more so than any variation in the models configuration shown.

For the following evaluations, the best performing PV power simulation configuration according to results this section is selected:

- Diffuse irradiance model by Skartveit and Olseth 1987 [87] and plane-of-array irradiance conversion model by Klucher 1979 [91],
- ECMWF intraday forecasts T_{NWP} of ambient temperature T_a,
- PV power model with the configuration fitted to historical data of the year 2012 for each site individually, and
- with linear regression ('lr') applied, trained at the previous 30 days' PV power measurement for each site individually

4.5. Evaluation of PV power forecasts

In this section an evaluation of PV power forecasts for single sites and all sites average is provided. CMV-based PV power forecasts are compared to NWP forecasts as references. Here, PV power measurements of the year 2013 in 15 minutes resolution for the dataset B (1196 sites) are used.

Some features of CMV-based PV power forecasts compared to NWP based forecasts are visible from PV power times series in fig. 4.15. CMV forecasts, having a comparatively high temporal and spatial model resolution are capable of following short-term fluctuations of irradiance and hence of PV power more than the NWP-based forecasts. In the

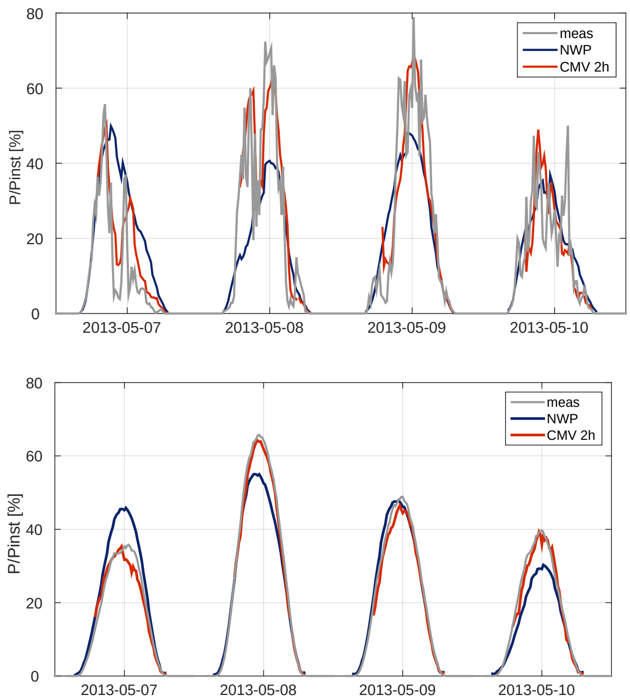

Figure 4.15.: Time series for four days in May 2013, with PV power measurements, CMV 2h and NWP intra-day forecasts in terms of P/P_{inst}. Top for one single site, bottom for all sites' averages. Dataset: 07-May-2013 to 10-May-2013, single site (top)/averages of 1196 sites (bottom), 15 min resolution.

bottom time series of figure 4.15 the smoothing effect of regional averaging is visible: Small scale fluctuations of PV power feed-in are compensated for and the regional PV power feed-in situation is the main feature to be predicted.

The forecast rmse and bias are displayed in figure 4.16 for CMV 1-5 hours and NWP forecasts for single sites and all sites' averages. For single sites, the rmse for CMV forecasts ranges from 10% of installed capacity for one hour to around 13.5% for five hours ahead, whereas the NWP forecasts show an rmse of around 12.9%. For averaged forecasts, rmse ranges from around 2% of installed capacity to 4.2% for CMV forecasts and 4.7% for the NWP-based forecasts, showing better performance of CMV forecasts at 5 hours ahead. The comparison of the rmse normalized to the average PV power feed-in allows a better comparison to irradiance forecast errors. The single site rmse is around 45% of the average feed-in for NWP and 35% for CMV 2h forecasts, for averaged forecasts around 18% (NWP) and 8% (CMV 2h).

The bias in all cases is neglectable and not higher than around 0.1% of P_{inst} (0.25% of average feed-in) as a result of the linear regression approach applied to the PV power forecasts.

The PV power forecast accuracy as a function of the time of day in the right panel of fig. 4.16 shows a strong diurnal dependency, like for irradiance in fig. 3.7. Power feed-in at noon is the highest, which also applies to the absolute forecast rmse, touching around 19% of P_{inst} for CMV 5 hour forecasts at noon. As CMV forecasts are not applicable when computed at solar zenith angles $\theta_Z > 80°$ when using satellite images of the HRV channel, first forecasts are available at different hours of the day depending on the forecast horizon.

Tilt and orientation of the PV systems have a relevant impact on the forecast accuracy. In figure 4.17 (left) the rmse of PV power forecasts is displayed dependent on the tilt and azimuth angle of the single systems, for PV power based on satellite derived irradiance and from CMV 2 hour and NWP intraday forecasts. There, the absolute rmse of P/P_{inst} and normalized to P_{mean}/P_{inst} are compared. A trend of higher absolute rmse for systems with a higher tilt angle β is observed: For instance for CMV 2h forecasts, the rmse with respect to angles between 0° and 10° is around 10.1%, for steeper angles (40° to 50°) the rmse reaches up to 12.4%. Partially, this is a consequence of higher incident angles and thus larger average irradiance incident on steeper tilted PV modules. However, for the normalized rmse the same but less pronounced trend is visible: An increase from 36% to 41.5% for CMV 2h forecasts is observed. The rmse dependence on the azimuth angle of the PV systems shows a decline with higher azimuth angles (fig. 4.17, right): The nrmse of 2h CMV forecasts decreases from around 38.3% to 35.8% (for $\phi = 0°$ to 90°).

The frequency error distribution for single sites and all sites' averages in fig 4.18 quantifies the occurrence of forecast errors magnitudes. For single sites, only 44% (NWP) to 51% (CMV 2h) lie within the error range of rmse ±5% of P_{inst} (dashed vertical lines), whereas 98% of all values are within ±35% (NWP) and ±32% (CMV 2h). For all sites averages, 77% (NWP) to 90% (CMV2h) are within the 5% margin, and 98% of all values between ±13% (NWP) and ±7.5% (CMV2h). The error frequency distribution is rather symmetrical with respect to $\epsilon = 0$, as can be expected from the low bias errors except for NWP forecasts, showing a higher occurrence of low positive ϵ.

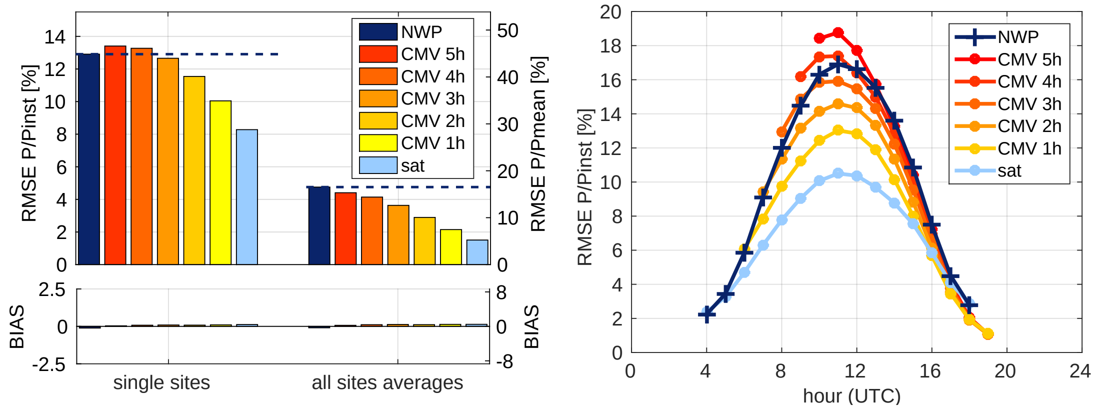

Figure 4.16.: Left: Rmse and bias of P/P_{inst} (left axis) and of P_{mean}/P_{inst} (right axis) for CMV 2 hour forecasts, compared to NWP intra-day forecasts and satellite derived irradiance (no forecast). Right: Rmse of of P/P_{inst} for single sites forecasts depending on the hour. Dataset: Apr–Nov 2013, 1196 sites, 15 min resolution, $\theta_Z < 80°$.

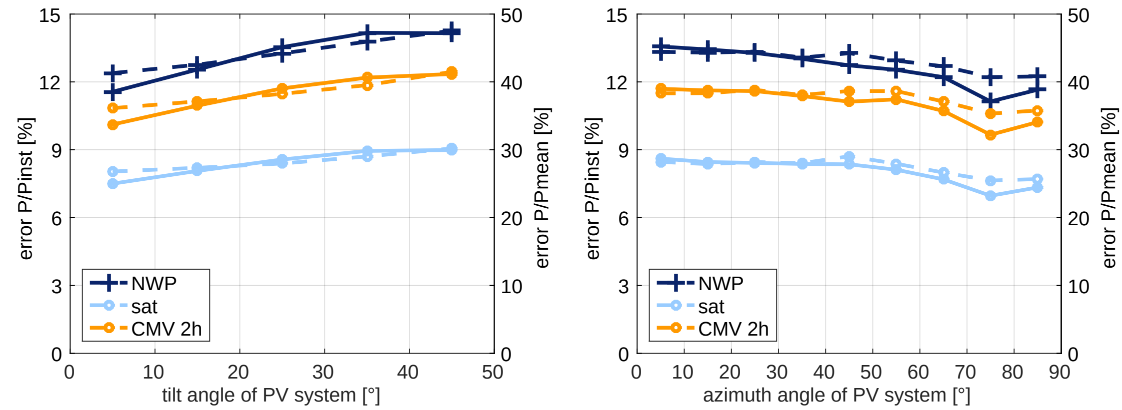

Figure 4.17.: Rmse for 2 hour CMV and NWP intra-day forecasts and satellite-based PV power (no forecast) in dependence on the tilt angle (left, with azimuth angles $|\phi| \leq 30°$), and on the azimuth angle ϕ (right, with tilt angles $20° \leq \beta \leq 40°$). Rmse of P/P_{inst} (left scale, solid lines) and P_{mean}/P_{inst} (right scale, dashed lines) for single sites forecasts. Dataset: Apr–Nov 2013, 1196 sites, 15 min resolution, $\theta_Z < 80°$.

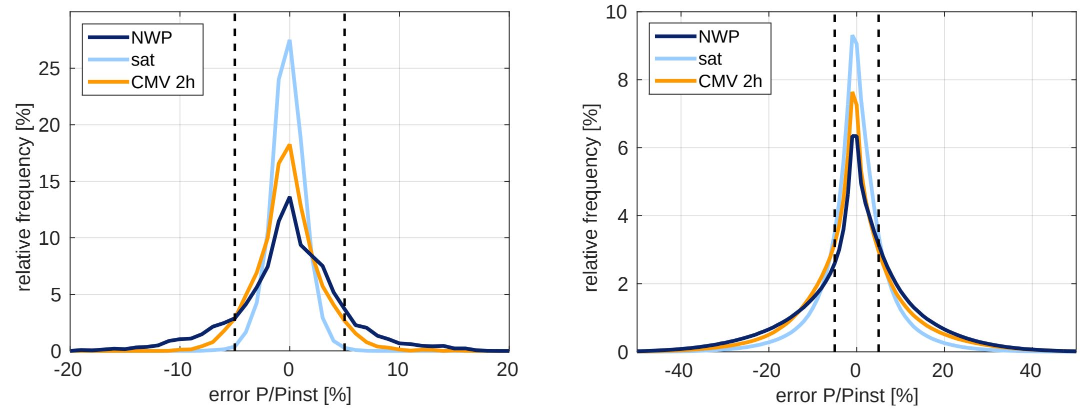

Figure 4.18.: Frequency distribution of error ϵ for single sites (left) and all sites' averages (right) for CMV 2 hour and NWP-based PV power forecasts and satellite-based PV power. Relative frequency for bins of 1% size, dashed lines at $P/P_{inst} = 5$ %. Dataset: Apr–Nov 2013, 1196 sites, 15 min resolution, $\theta_Z < 80°$.

The annual trend of PV power forecast errors is displayed in figure 4.19 for all sites' averages compared to the average normalized PV power production for all systems. All months are included in contrast to the evaluations shown above. For the averaged power feed-in, a strong annual trend is visible, with the highest PV power production in the summer months. The absolute rmse of PV power simulation based on irradiance forecasts or satellite derived data remains almost constant over the year, only the months January and March and April show rmse slightly above average. This disagrees with evaluations of the global horizontal irradiance forecasts' rmse (fig. 3.9 in section 3.7), showing a significant annual trend and higher rmse in summer months. This issue is discussed in more detail in the following section 4.6. For NWP, a trend of higher rmse for the first half of the year is observed, as also found for corresponding evaluations of irradiance forecasts in fig 3.9.

Additionally, a significant increase in bias for the months January and February regardless the forecast method or horizon can be seen. This is due to a frequent occurrence of snow-covered modules in the measurement dataset, leading to an overrating of PV power from forecasts. The effect varies for NWP and CMV forecasts, having smaller effect on CMV forecast as partially snow is detected as cloud cover and therefore leading to a reduced feed-in being forecast. The issue of snow cover forecasting and detection is addressed in Lorenz et al. (2011) [22] but also is subject to ongoing research. This is also true for the impact of persistent large-area fog which occurred on a significant number of days in spring and fall months, contributing to an overrating of PV power forecasts.

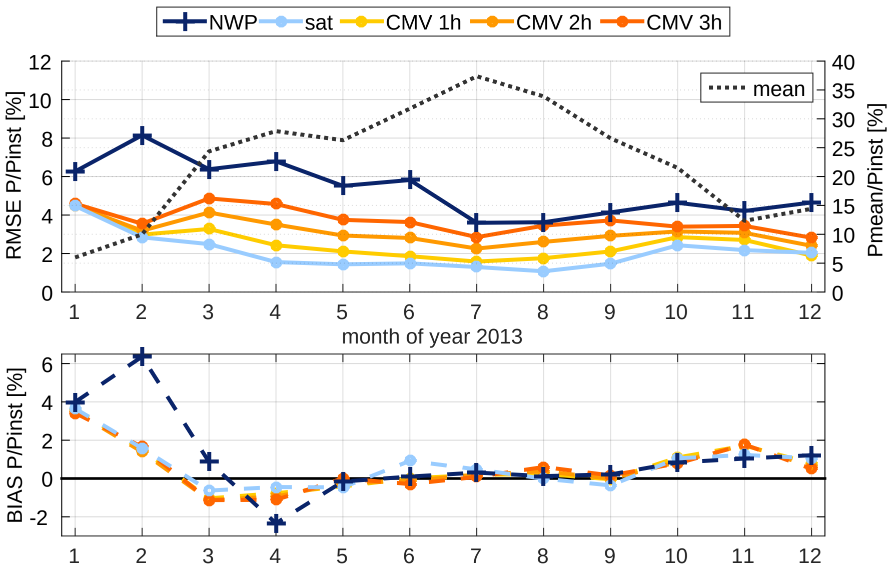

Figure 4.19.: Rmse (top) and bias (bottom) of PV power forecasts depending on the month of the year 2013 for all sites' averages, displayed for CMV 1 to 3 hours and NWP intraday forecasts, and for satellite-based PV power (no forecast). Dataset: Jan–Dec 2013, 1198 sites' averages, 15 min resolution, $\theta_Z < 80°$.

4.6. Comparison to irradiance forecasts

The correlation of PV power and irradiance forecasts is addressed in this section. In previous sections, irradiance forecasts were evaluated with temporal resolution of 1 hour, PV power forecasts with 15 minutes. To compare both, the different temporal resolutions and effects of spatial averaging on the forecast rmse are addressed. In a next step, the differences arising from evaluating PV power forecasts with various tilt angles are quantified.

For comparison, the normalized rmse PV power forecasts for different temporal and spatial resolutions are displayed in fig. 4.20. The datasets are unified to the months April to November 2013, with the same restrictions to evaluated situations, i.e. solar zenith angles and data availability. Irradiance and PV power forecast rmse both are normalized to the corresponding averages I_{mean} or P_{mean}. 220 PV power sites are evaluated here, randomly picked from the overall dataset, to consider a comparable amount of sites as for irradiance evaluations (217 sites).

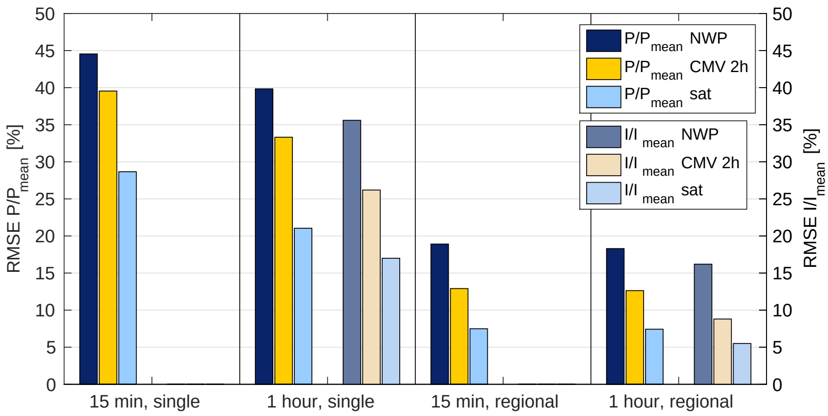

Figure 4.20.: Rmse of PV power and irradiance forecasts, normalized to P_{mean} or I_{mean} respectively for different temporal and spatial resolutions. Dataset: Apr–Nov 2013, 220 PV sites, 217 irradiance measurement stations.

In general, spatial and temporal averaging leads to a reduction of the rmse for irradiance and PV power forecasts. For example, the rmse of CMV 2 hour PV power forecasts decreases from 39.5% to 33.2% (by 16.0%) from 15 minutes to 1 hour averages for single sites forecasts. When spatial averaging is applied, rmse decreases to 13.1% for 15 minutes all sites' averaged forecasts, representing an improvement of 66.8% compared to 15 minutes single site forecasts. For 1 hour and all sites' averages, the rmse is reduced to 12.6%, which is an improvement of 68.1%, compared to 15 minutes single site forecasts. The beneficial effect on the rmse of temporal averaging from 15 min to 1 hour is smaller for all sites averages, compared to single sites forecast, with a relative improvement of 3.8% compared to 16.0%).

For irradiance evaluated with respect to 1 hour averages only, rmse is lower than for normalized PV power with the same temporal resolution. This is valid for both, single site and all sites' averages. This is a consequence of PV power forecasts being based on forecasts of irradiance and of error added by the irradiance-to-power conversion and by

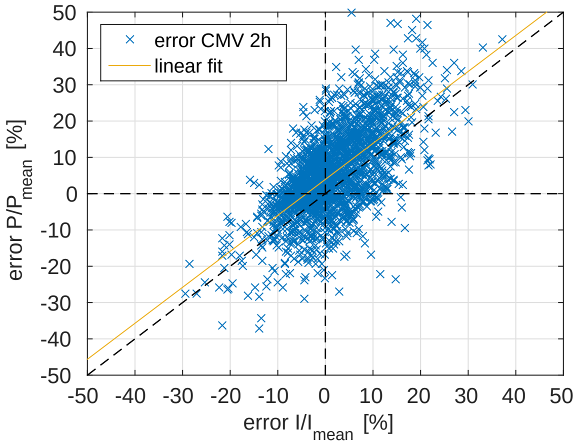

Figure 4.21.: Comparison of 2 hour CMV forecast error for irradiance ϵ_I and PV power ϵ_P; correlation coefficient $cc = 0.66$. Dataset: Apr–Nov 2013, 1 hour resolution, averages for 220 PV power and 217 irradiance measurement sites, $\theta_Z < 80°$

the contribution of differently tilted PV modules in the evaluation. A direct comparison of PV power and irradiance forecast error is given in figure 4.21. Here, forecasts with same temporal and spatial resolution are compared: The error ϵ for 1 hour all sites' averages of CMV 2 hour forecasts of PV power and irradiance is compared, each normalized to the average measured irradiance or PV power. Both errors show a correlation of 0.66, with a positive offset for errors of PV power forecasts.

For PV power forecasts an additional error is added, induced by the conversion to POA irradiance and by the PV power simulation process. The annual trend of the rmse of PV power forecasts (see figure 4.19) shows a different behavior than of horizontally measured irradiance, see figure 3.9. For irradiance forecasts, evaluated on the horizontal plane only, the absolute rmse follows the annual trend of mean irradiance, with lower rmse in winter than in summer months. PV power forecasts' rmse show a slight opposing trend with higher absolute rmse for winter than for summer months, see figure 4.19 for all sites' averages. This can be explained partly by snow-covered modules but is mainly a result of the tilt dependent rmse for different systems configuration (see figure 4.17). Solar zenith angles and with it the incidence angle of irradiance on the tilted surfaces changes within the year: For winter months with high solar zenith angles, steeply tilted PV modules receive more irradiance than horizontally aligned ones. Same forecast errors for cloud cover and thus for k^* have higher impact here than for horizontally aligned planes.

The annual course is displayed separately for different classes of tilt angles in figure 4.22. The sites displayed are restricted to azimuth angles of $|\phi| \leq 30°$ to avoid an impact of orientation within this analysis. The amount of stations within each class is reduced to be at a maximum around 100 sites, randomly selected to maintain the comparability among the different classes of tilt angles. For almost horizontally aligned PV modules ($\beta \leq 10°$) the annual trend resembles the trend of irradiance forecast errors with significant lower rmse in winter months than in summer months. This trend is reversed for tilt angles of $\beta \geq 40°$ dominated by higher rmse in winter than summer. For the months May to July the tilt angles' impact is not visible as all configuration show similar rmse values.

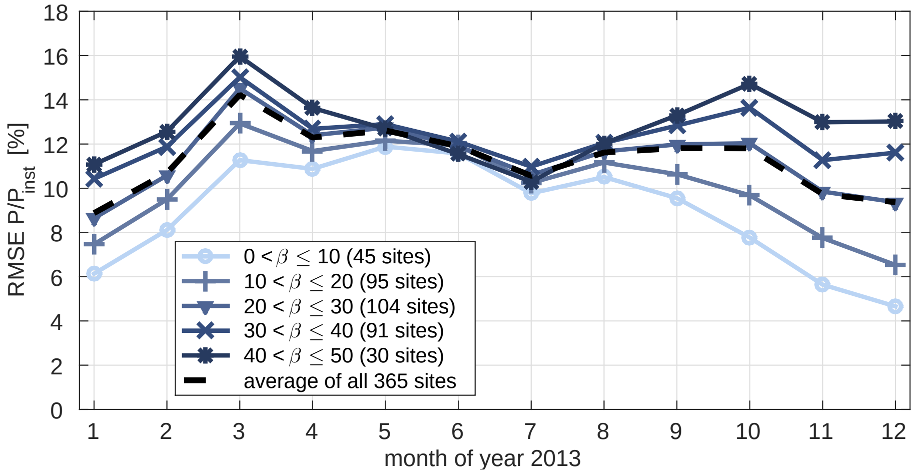

Figure 4.22.: Tilt dependence of annual trend of rmse for single sites and CMV 2 hour PV power forecasts. Systems with azimuth angles of $|\phi| \leq 30°$ are considered here. Note different sizes of datasets for each configuration according to available sites in the corresponding class. Dataset: Jan–Dec 2013, 1 hour resolution.

4.7. Conclusion

In this chapter the process of irradiance-to-power conversion was introduced and evaluated with respect to its impact on the PV power forecast accuracy. The conversion approaches presented here are based on explicit physical modeling, complemented by a simple statistical post-processing. One focus in this chapter was on PV power simulation with respect to the optimized configuration of the models and datasets used for the application to forecasting. Evaluations show only an insignificant impact of the tilt conversion model on the overall PV power simulation accuracy. The benefit of adapting power simulation parameters to a historic dataset and applying post-processing with PV power measurement data is demonstrated. Also, the value of using NWP temperature forecasts rather than climatological mean temperatures was confirmed, with its impact strongly decreasing when an adaption of PV power forecasts to daily updated measurements is possible. The analysis was done in the context of PV power forecasting, being mainly dominated by the accuracy of irradiance forecasts.

A comprehensive evaluation of PV power forecasts based on different irradiance forecasting approaches is provided afterwards. Diurnal trends, the effect of spatial averaging and the better performance of CMV forecasts compared to NWP-based forecasts is comparable to evaluations provided of irradiance forecasts in chapter 3. However, the POA-conversion of irradiance and the PV efficiency modeling adds further inaccuracy.

5. Combination of PV power forecasts

Forecasts of PV power based on CMV and NWP presented so far share a limited forecast quality even for the shortest forecast horizons: For satellite-based forecasts this is due to the error of the Heliosat method (see section 3.7) and limited spatial and temporal resolution of MSG images. For numerical weather predictions, limited model resolution and physical parameterization, as well as insufficient quantification of initial or boundary conditions are the main restrictions [99]. In each case, the PV power simulation process adds another level of uncertainty. High potential for improvement is found in the integration of online-measured PV power, which is capable of representing the actual state of the system, if available. The combination of CMV- and NWP-based PV power forecasts with online measured PV power is subject of this chapter, as visualized in fig. 5.1: Integrating online measured PV power is achieved by the persistence approach, using a PV power clear sky model. Combining the individual forecasts is done for single sites and all sites' averaged forecasts separately. By this combination approach, an optimized forecast for each situation and forecast horizon is aimed at.

For the integration of PV power measurement into PV power forecasting a persistence approach in analogy to the irradiance-based persistence model (sec. 3.5) is used and introduced in section 5.1. The method of forecast combination and its configuration is described in section 5.2, weighting the individual forecasting methods with respect to different parameters. In section 5.3 an evaluation of the combined forecast accuracy is presented; a detailed analysis of the weighting factors is provided in section 5.4. The sensitivity of combined forecast accuracy towards different input datasets and delays in data availability in an operational context is analyzed in sections 5.5 and 5.6.

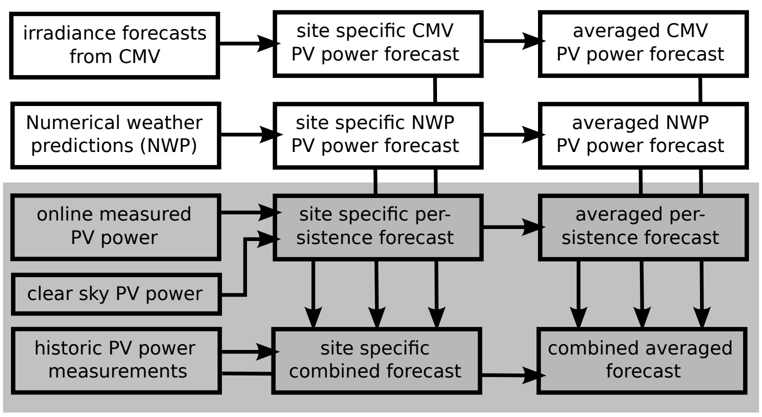

Figure 5.1.: Forecasts of PV power feed-in based on cloud motion vectors (CMV) and numerical weather predictions (NWP) are derived for single sites and all sites' averages. Online measured PV power, combined with a clear sky PV power model, are the basis of persistence forecasts. These individual forecasts are combined for single sites and all sites' averages separately, trained using historic PV power measurements.

5.1. Persistence forecasts based on online measured PV power

For the intregration of online measured PV power into forecasting, a PV power persistence approach is introduced. This approach is used in an analogous manner to the persistence approach for irradiance forecasting, see section 3.5 or e.g. Pelland et al. (2013) [8]. In this section, first, the clear sky PV power P_{clear} and the PV power clear sky index k^*_{PV} are described. These quantities are fundamental for the persistence approach introduced afterwards.

5.1.1. Clear sky and clear sky index for PV power

The clear sky irradiance I_{clear} describing the irradiance in case of no clouds but including absorption processes in the atmosphere was introduced in section 3.1. Based on this clear sky irradiance, a clear sky PV power output P_{clear} is calculated using the same irradiance-to-power conversion approach as introduced in section 4, with the configuration given in section 4.4.5. The simulation of clear sky PV power for each system individually reflects the diurnal and annual dependency on clear sky power taking account of its specific tilt and azimuth angles. The issue of temperature information within the PV power clear sky model is shown in the appendix, section A.3.

For different tilt and azimuth configurations, the clear sky PV power feed-in is displayed in fig. 5.2 for the 21st June and the 21st December, representing the summer and winter solstice with lowest and highest solar zenith angles in a year. Highest power feed-in in both cases is visible for the 30°-tilted PV system ($\phi = 0°$). For summer solstice, the $\beta = 0°$ and $\beta = 50°$ tilted modules (both $\phi = 0°$) show almost equal amplitudes. In contrast to that, for the winter solstice with very high average solar zenith angles, PV systems with a high tilt receive much more irradiance than system with a lower tilt angle. The PV system displayed with a $\phi = 90°$ west and a tilt angle of $\beta = 30°$ shows a strong offset of the typical diurnal cycle towards evening hours. For an equally east orientated but less tilted PV system ($\phi = 90°$ and $\beta = 15°$) the same but less pronounced

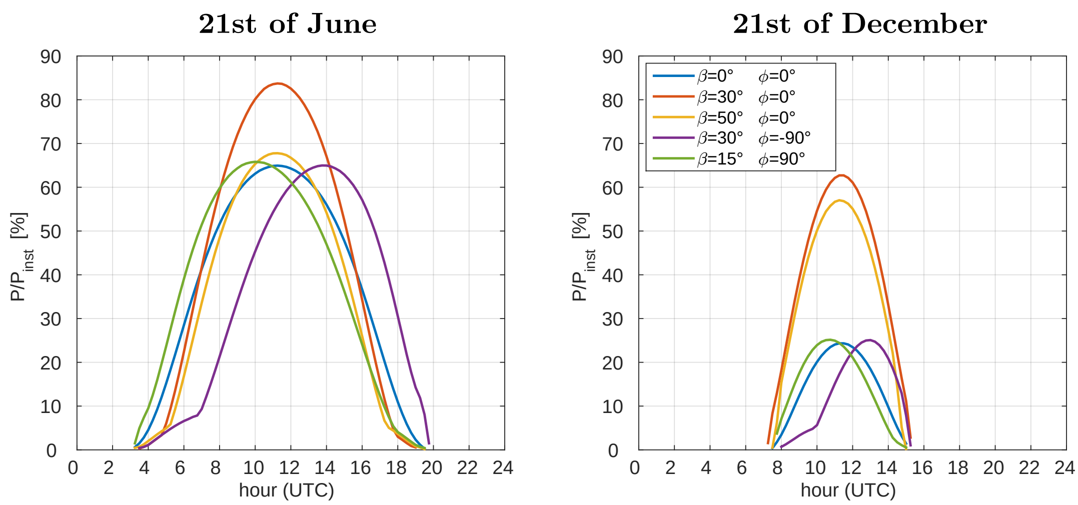

Figure 5.2.: Clear sky PV power time series for two days (left: June 21st, right: December 21st) for PV systems with different tilt and azimuth angles (with azimuth angle $\phi = 0°$ corresponding to South, and tilt angle $\beta = 0°$ to horizontal alignment).

effect towards morning hours is visible. This typical behavior of clear sky PV power for different tilt and azimuth angles is of high importance as it significantly influences feed-in characteristics.

In analogy to the clear sky index for irradiance (sec. 3.1) a PV power clear sky index k^*_{PV} is gained. According to the definition in equation 3.3 it is written as

$$k^*_{PV} = \frac{P_{meas}}{P_{clear}} \tag{5.1}$$

with P_{meas} for the actual measured PV power feed-in of the system and P_{clear} the clear sky PV power introduced in section 5.1.1. The so derived k^*_{PV} is assumed to give a quantification of cloud cover at the PV site. Being based on online PV power measurements P_{meas}, it enables a description of the systems' actual state without being limited by resolution and quality of NWP or satellite data. This measure was for example also used in Engerer et al. (2014) [19]: There, k^*_{PV} was derived with good agreement for a number of PV systems and used for forecasting of nearby PV systems.

The characteristics of k^*_{PV} differs from the global horizontal irradiance-based k^* as tilted irradiance in the clear sky case shows strong dependency on the position of the sun. This has to be regarded when taking k^*_{PV} as quantification of cloud cover, as it is done by the persistence approach, introduced in the following section 5.1.2. In case of k^* based on horizontally measured irradiance I (see section 3.1) the estimation of cloud cover through k^* is a good approximation [100]. For k^*_{PV} the impact of differently tilted modules may lead to a limited applicability of this assumption.

The response of k^*_{PV} to differently modeled cloud cover situations is analyzed in the following in order to validate the transferability of this assumption to PV power persistence forecasts: The diurnal characteristics of k^*_{PV} is essential for the persistence approach. For fixed clear sky indices $k^* = 0.1; 0.5$, the behavior of k^*_{PV} for different tilt angles over the course of the day is modeled (fig. 5.3; for other variations of k^* refer to fig. A.2 in the appendix). For $k^* = 1$, the PV power clear sky index perfectly matches $k^*_{PV} = 1$, as in this case naturally $P_{meas} = P_{clear}$. For $k^* = 0.5$, high shares of the PV power clear sky index are close to $k^*_{PV} = 0.5$, but with significant variation in the morning and evening hours. Except for that, k^* are mapped comparably well by the PV power clear

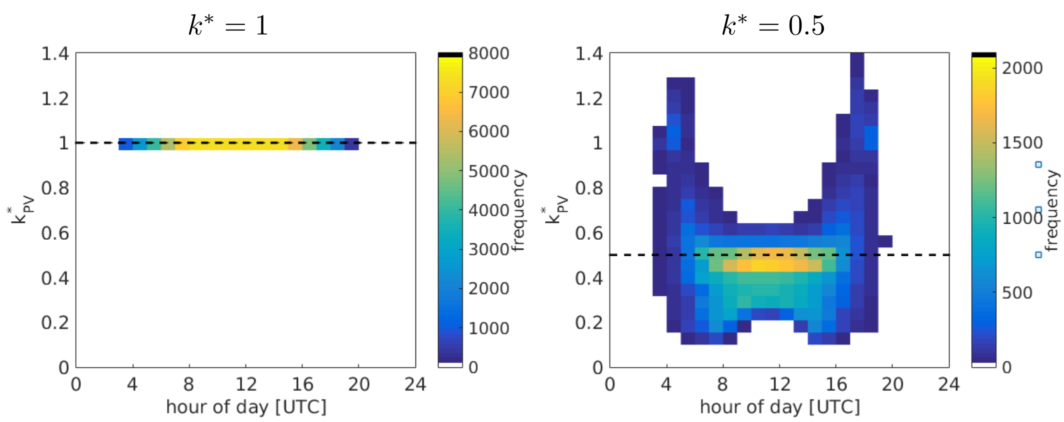

Figure 5.3.: Modelled k^*_{PV} for fixed k^* values in dependence on the hour (UTC) for the dataset for 12 days a year (each 21st) and for 150 sites with $\phi < 30°$ and variating β.

sky index k^*_{PV}, but with a considerably high amount of values tending to $k^*_{PV} < 0.5$. This is a result of different angles of incidence on the PV modules and reveals a limitation of estimating the cloud cover through k^*_{PV}, especially for the morning and evening hours. Still, for a majority of situations, the k^*_{PV} provides a fair approximation of the irradiance-based k^*.

5.1.2. Persistence of k^*_{PV}

The persistence forecast approach is illustrated in fig 5.4. At time t_0, online measured PV power $P_{meas}(t_0)$ is used to determine the PV power clear sky index $k^*_{PV}(t_0)$. A constant k^*_{PV} is assumed for the following hours:

$$k^*_{PV,pers}(t_0 + \Delta t) \equiv k^*_{PV}(t_0) \tag{5.2}$$

The persistence forecast P_{pers} is derived using the corresponding clear sky power P_{clear}. A forecast of PV power at time step $t+\Delta t$ is derived by applying the inverse equation 5.1 and leads to:

$$\begin{aligned} P_{pers}(t_0 + \Delta t) &= k^*_{PV,pers}(t_0 + \Delta t) \cdot P_{clear}(t_0 + \Delta t) \\ &= k^*_{PV}(t_0) \cdot P_{clear}(t_0 + \Delta t) \end{aligned} \tag{5.3}$$

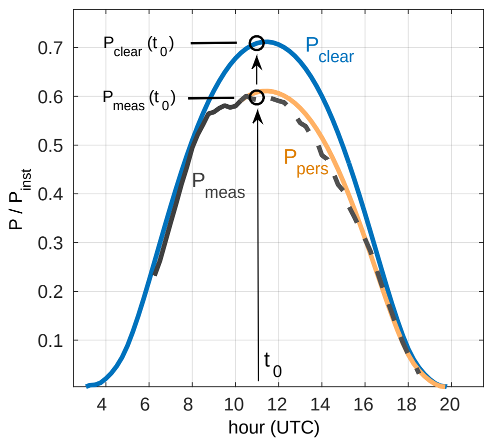

Figure 5.4.: Visualization of the persistence forecasts P_{pers}: At t_0, the PV power clear sky index $k^*_{PV}(t_0)$ is derived from $P_{meas}(t_0)$ and $P_{clear}(t_0)$ and assumed to persist for $t > t_0$.

The accuracy of the persistence forecast strongly depends on the variability of cloud cover and whether applied to single sites or spatially averaged forecasts. For low variability, the persistence approach shows significant lower rmse than for situations with highly variable cloud cover, see left panel of fig. 5.5. Due to smoothing effects reducing variability of spatially averaged forecasts, the persistence approach in general shows better performance than for single site forecasts, see right panel of fig. 5.5.

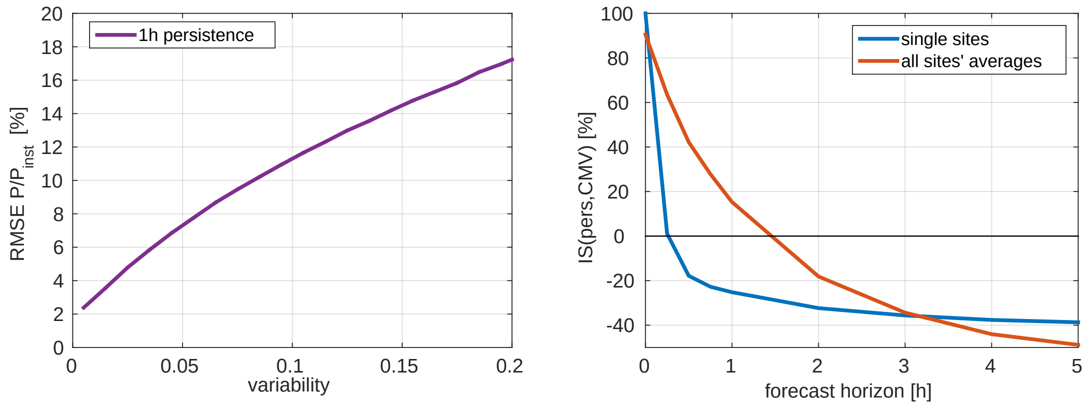

Figure 5.5.: Left: Rmse of 1 hour ahead persistence forecasts in dependency on the intra-hour variability of k^*_{PV} (standard deviation of k^*_{PV}) for single sites. Right: Improvement Score of persistence forecasts compared to CMV-based PV power forecasts in dependency on the forecast horizon for single sites and all sites' averages. Dataset: May–Nov 2013, 921 sites, 15 min resolution, $\theta_Z < 80°$.

5.2. Combination of PV power forecasts

The combination of the different forecast approaches is performed with a linear regression approach: By this, a weighting of the approaches according to their individual forecast rmse within a defined training period and in dependence on the forecast horizon and other parameters is achieved. In addition, a statistical adaptation to recent measurements is introduced by this (compare to section 4.2.4).

Persistence forecasts P_{pers}, CMV forecasts P_{CMV} and NWP forecasts P_{NWP} are combined using linear regression coefficients a, b, c and d. The combined forecast P_{combi} then is written as

$$P_{combi} = a \cdot P_{pers} + b \cdot P_{CMV} + c \cdot P_{NWP} + d \tag{5.4}$$

A linear regression with measured PV power P_{meas} is performed using a *least-square-*algorithm. The allowed range for these coefficients is restricted to positive values to maintain physical plausibility.

The coefficients a, b, c and d are separately derived for each forecast horizon. This is a direct consequence of the horizon depending differences in performance of each forecast approach, as discussed in the previous chapters. Other parameters used as additional constraints for the coefficients are analyzed, as the different forecasting methods' performance are in depending on various other parameters. Here, the effect of e.g. the hour of day or solar zenith angles on the combined forecast rmse is compared. The training of the coefficients is performed based on historic forecasts and measured PV power for a number of preceding days. Choosing a training period close to the forecast day, in contrast to using a fixed set of days, allows to consider seasonal changes in the performance of the different forecasting approaches.

In the following, the optimal configuration of the forecast combination is found. This configuration is done for single site forecasts and all sites' averages separately. For this purpose, measured PV power and PV power forecasts in the period April to November 2012 of the dataset 'B' (921 sites) is used. The configuration of the irradiance-to-power conversion as summarized in section 4.4.5, without the application of linear regression 'lr' is used. All evaluations shown in this chapter are based on persistence forecasts (sec. 5.1.2), CMV forecasts (sec. 3.3) and the combined-DWD-ECMWF forecasts (sec. 3.4) unless denoted otherwise. For an evaluation of the forecast rmse in dependence on the forecast horizon for the selected testing period, top row of fig. 5.6, left for single sites, right for all sites' averages.

As a reference for evaluation of the combined forecast configuration, the best available individual approach for each horizon is determined ('best' in fig. 5.6). In the bottom row of fig. 5.6, the IS of the individual forecasts to the 'best' for each forecast horizon is displayed. By this, the rating of the forecasting methods by the IS is shown, with $IS = 0$ for the forecasting method referenced to for each horizon.

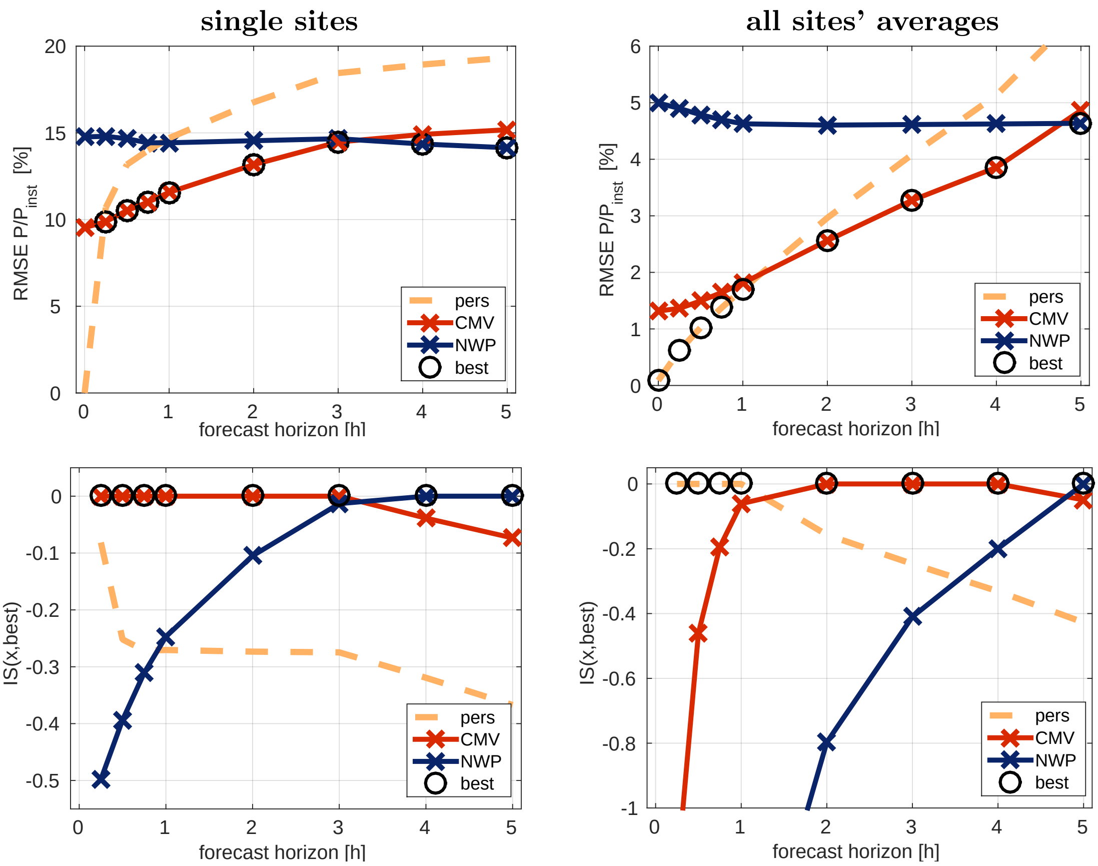

Figure 5.6.: Evaluation of the three individual forecast approaches persistence, CMV and NWP and representation of best forecast for each horizon from 0 to 5 hours ahead, rmse of $\frac{P}{P_{inst}}$ (top) and Improvement Score of all approaches according to the 'best' forecast (bottom). Dataset: Apr–Nov 2012, 921 sites, 15 min resolution, $\theta_Z < 80°$.

5.2.1. Configuration for single sites

The benefit of the combination approach depends on its configuration with respect to i) the selection of additional constraints for the calculation of the fitting coefficients and ii) the length of the training period applied. The fitting coefficients are trained separately for each forecast horizon and for classes of auxiliary parameters (see table 5.1). These parameters are used to determine classes with varying performance of the individual forecast approaches that are combined.

The different parameter sets from table 5.1 are compared to each other with respect to their impact on the combined forecasts rmse. A common training period of 50 days is used; the parameter sets are compared by the $IS(combined, best)$. This improvement score relates the rmse of the combined approach, using the tested parameter, to the best individual forecast approach for each forecast horizon (fig. 5.6). In the left panel of fig. 5.7, the $IS(combined, best)$ is normalized to the 'hour' parameter set and displayed for the forecast horizon 1 to 3 hours ahead.

According to this evaluation, the approach using 'hour', 'var(k^*_{PV})' and the combination of both 'hour + var(k^*_{PV})' almost equally show the highest performance for each horizon.

Table 5.1.: Different parameter sets used in addition to the horizon dependency for combination of forecasts. For each parameter set the best configuration is displayed with respect to its impact on the improvement of the combined forecasts.

ID	description
simple	horizon dependency considered only
sol zenith	solar zenith angles θ_z at forecast calculation time, in classes of $30° \leq \theta_z \leq 90°$ by $10°$ step size (6 classes)
slots	15 min intervals of a day (96 classes)
hour	hour of day (24 classes)
var(k^*_{PV})	variability by standard deviation of measurement-based k^*_{PV} of the preceding hour at forecast calculation time (3 classes)
hour + var(k^*_{PV})	2 classes of variability of k^*_{PV} for each hour per day (48 classes)

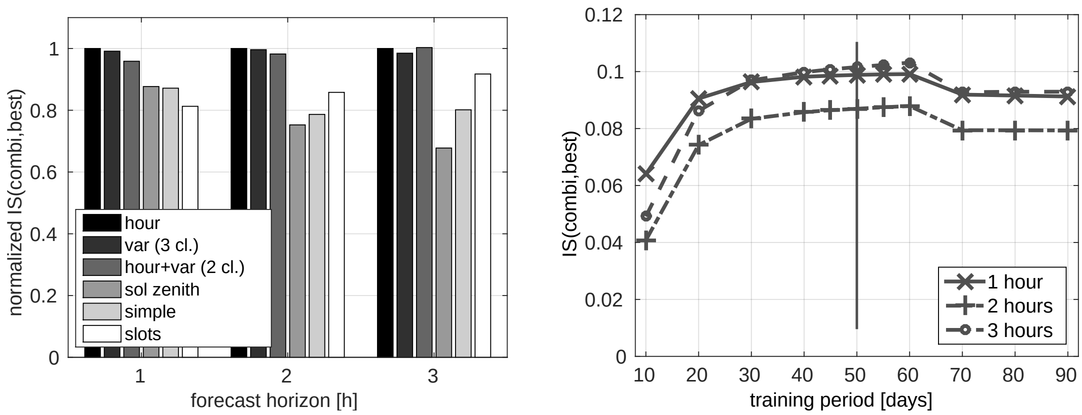

Figure 5.7.: Comparison of the additional parameter sets for the combined forecast approach, according to table 5.1. Left: Improvement score of rmse for the combined forecasts normalized to the rmse of the best not-combined forecasts for horizons 1, 2 and 3 hours. For each horizon, the IS is normalized in relation to the first displayed parameter set ('hour'). Right: IS as a function of the training period for single site combination of forecasts, displayed for combination based on the 'hour' parameter. Dataset: May–Nov 2012, 921 stations, 15 min resolution.

The approach 'var(k^*_{PV})' considers the variability of the k^*_{PV} for hourly averages of the hour before forecast calculation and is derived from measurements. Doing so, the variation of the forecast performance for different classes of variability is introduced. Referring to different hours a day ('hour'), the diurnal dependency of the forecast rmse is considered on an hourly average basis, as the forecast rmse of the different methods vary over the day. The lower IS than for the 'var(k^*_{PV})'-approach in these hours is partially a consequence of a higher amount of classes (24 for 'hours' compared to 3 for 'var(k^*_{PV})') and thus a reduced amount of data in each class. For the 'hour + var(k^*_{PV})' approach, the 'hour' and variability approach are combined using two variability classes. The combination based on the solar zenith angle θ_z ('sol zenith') takes into account the dependency on the solar zenith angles at forecast origin, here in fixed classes of 10°. This considers the diurnal change of forecast performance for each method but does not differentiate between morning and evening hours. With classes of 15 min intervals of a day ('slots'), the diurnal dependency of the forecast rmse is represented, like for the 'hour' parameter. This shows less improvement, as the high amount of classes further reduces the data availability. The 'simple' combination does not include any other parameter and shows also considerable small improvement, as no further information is utilized. Still, this approach can compete with the 'slots' or 'sol zenith'.

In the right panel of figure 5.7, the IS in dependence on the length of the training period is displayed, evaluated for the 'hour' approach and horizons 1 to 3 hours, for 10 to 90 days prior to the day the forecast is derived at. Using the previous days instead of a fixed set of training days allows to include seasonal changes of forecast performance for the different methods. A longer training period would on the one hand increase the amount of data and thus the stability of coefficient fitting; but on the other hand, the seasonal changes are less distinct then. An optimum is found at around 40 to 60 days, regardless the forecast horizon.

For parameter training, using an additional description of relevant parameters proved to be beneficial to the combination of forecasts. Still, a compromise between size of parameter classes and the degree of details depicted has to be found. For forecast combination, the approach of considering different hours of day 'hour' and a training period of 50 days is chosen. In contrast to that, the parameter considering different classes of variability 'var(k^*_{PV})' were utilized in Wolff et al. (2015) [86] and Kühnert et al. (2014) [101].

5.2.2. Configuration for spatially averaged forecasts

For spatially averaged forecasts, the configuration of the combined forecasts is determined separately, as it shows differences in characteristics compared to single site forecasts. Similar variation in parameter selection for training was tested as well as the optimal training horizon derived (see fig. 5.8). This was done using the average of all sites in the dataset named prior. Here, the 'hour' parameter for testing shows largest values of IS for all horizons displayed. Differences to the remaining parameter sets are comparatively small, even for the 'simple' approach with no additional training parameter but a larger training set included. The training with 'var (3cl)' as additional parameter set shows lowest improvement especially for larger forecast horizons, as variability is less pronounced for the regional averages than for single sites and the value of this information decays with increasing forecast horizon.

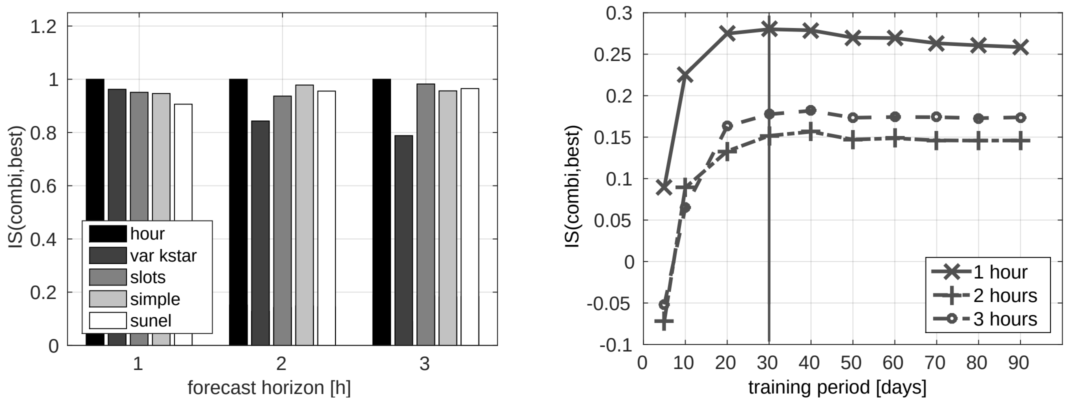

Figure 5.8.: Left: Improvement score of rmse for the combined forecasts referring to the rmse of the best non-combined forecasts for horizons 1, 2 and 3 hours. For each horizon, the IS is normalized with respect to the first displayed parameter set ('hour'). Right: IS as a function of the training period for combination of spatially averaged forecasts, displayed for combination based on the 'hour' parameter. Dataset: May–Nov 2012, 921 stations, 15 min resolution.

The IS in dependence on the length of the training period is shown in the right panel fig. 5.8. Most benefit of increasing the length of the training period is seen for around 30 preceding days. Shorter training periods show a significant lower Improvement Score, longer training periods do not lead to any improvement. For the combination of spatially averaged forecasts the 'hour' parameter and a 30 days training period were chosen.

5.3. Evaluation of the combined forecasts

An evaluation of the combined forecasts, compared to the individual forecast approaches is displayed in fig. 5.9 for single sites (left) and all sites' averages (right). The error of the individual forecast approaches with linear regression applied are displayed. The evaluation is done for the months May to November 2013, again to omit months with a high probability of snow-covered modules in the training and evaluation period.

The reduction for forecast rmse by the combined forecasts and including PV power measurements amounts up to around 15% (at 15 to 30 minutes ahead) for single sites compared to the CMV-based forecasts. For the forecast horizon of two hours, the improvement is around 11%. Naturally, at forecast horizon '0' representing the time of forecast calculation, forecast rmse and bias are zero, as the persistence equals the measured PV power and is weighted with the factor 1. For all sites' averages, the improvement by including measured PV power and the combination of forecasts is much higher: Here, it reaches up to around 60% for 15 to 30 minutes ahead. For 2 hours, the improvement still is about 28%.

With respect to the size of the area averaged, the benefit of including the persistence forecasts into the combined forecasts differs. Different sizes of averaged areas are analyzed with respect to persistence forecasts and the impact on combined forecasts in fig. 5.10. The areas compared here are based on a similar analysis in chapter 3, see fig. 3.4. Areas with dimensions $1° \times 1°$, $2° \times 2°$ etc. to $10° \times 10°$ (corresponding to all sites' averages)

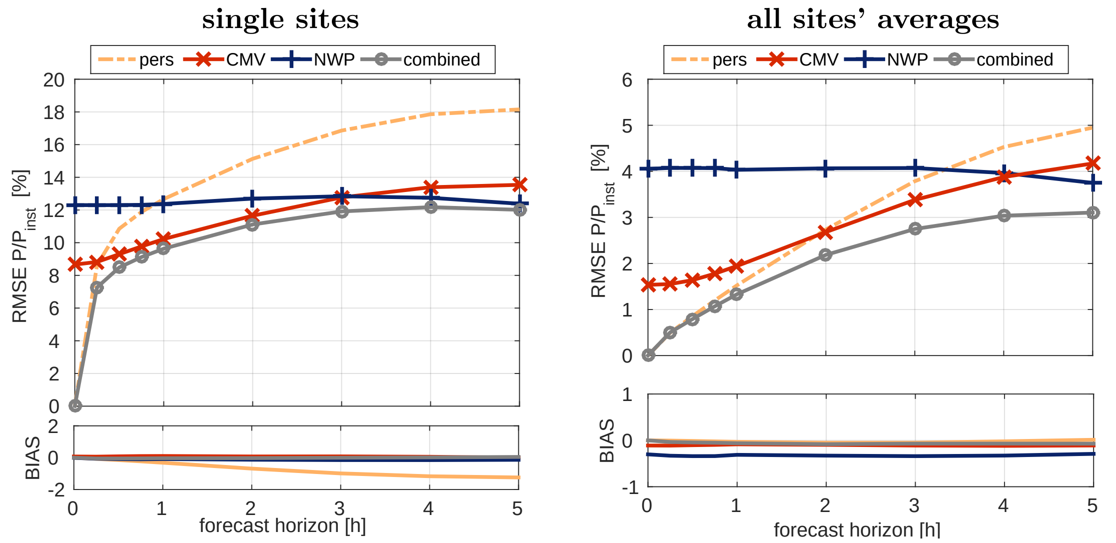

Figure 5.9.: Evaluation of combined forecasts ('combined'), compared to the persistence, CMV- and NWP-based PV power forecasts ('pers','CMV','NWP'). Dataset: May–Nov 2013, 921 stations, 15 min resolution, solar zenith angles $\theta_z < 80°$.

are averaged and evaluated. Multiple overlapping regions of the same size with 1° shift in both directions (latitude and longitude) are considered here.

Improvement Scores with CMV forecasts as reference, are displayed in the left panel of fig. 5.10 in dependence on the forecast horizon for the different area sizes, for i) the combined forecasts (top) and ii) persistence forecasts with linear regression applied (bottom). The 'IS(combi,CMV)' for 1 to 3 hours ahead as a function of the region size are displayed in the right panel of fig. 5.10. This figure includes the forecast horizon IS(pers,CMV)=0, i.e. the persistence forecast shows same rmse as CMV forecasts.

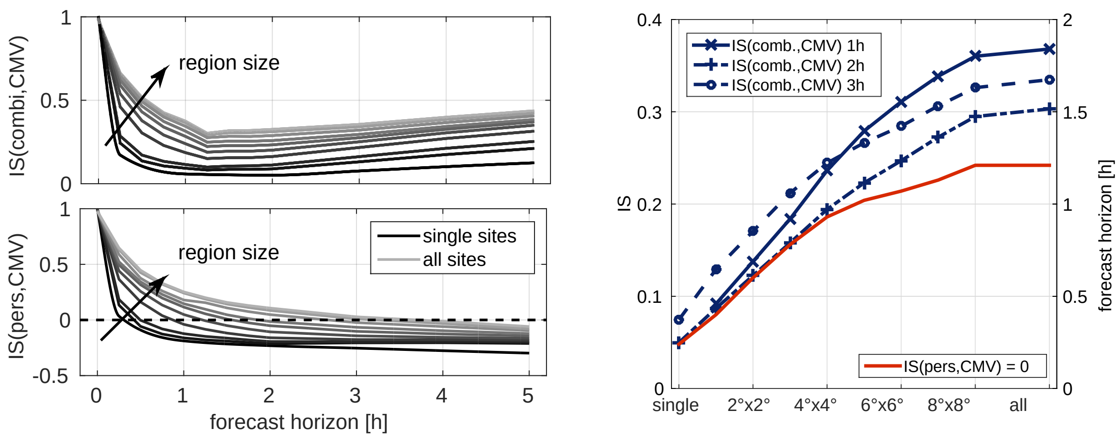

Figure 5.10.: Evaluation of persistence and combined forecasts for different averaging regions, from single sites to all sites averages. For an overview of the areas' distribution refer to fig. 3.4. Left: IS(combi,CMV) and IS(pers,CMV) in dependence on the forecast horizon for different regions averaged. Right: Dependency of i) the IS(comb,CMV) for 1 to 3 hours ahead forecasts and ii) the forecast horizon with IS(pers,CMV)=0 as a function of the averaging area. Dataset: April–Nov 2013, 921 stations, 15 min resolution, $\theta_Z < 80°$.

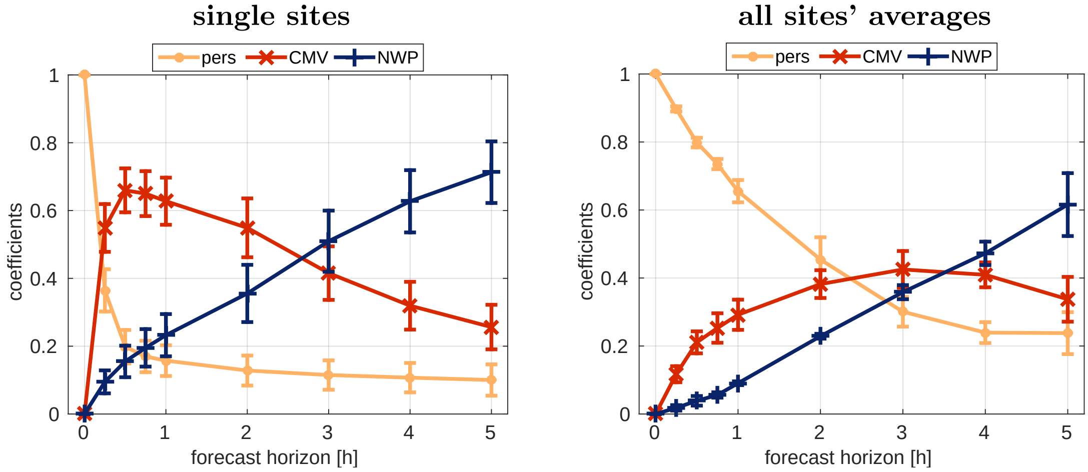

Figure 5.11.: Fitting coefficients for single sites (left) and for all sites averages (right) in dependence on the forecast horizon; error bars give the standard deviation of the fit parameters. Dataset: Apr-Nov 2013, 921 stations.

From both figures, the skill of the persistence and combined forecast increases with the size of area averaged, valid for all forecast horizons, with a declining gradient towards larger areas. The forecast horizon, when the condition $IS(pers, CMV) = 0$ is satisfied, increases with the size of region as well as the IS for the combined forecasts. For persistence forecasts of 3 hours onward, spatial averaging is of less benefit compared to the gain of regional averaging for the CMV forecasts.

5.4. Evaluation of fit coefficients

In this section, an analysis of the fit coefficients a, b and c and by this the rating of the individual forecasts P_{pers}, P_{CMV} and P_{NWP} in the combined forecasts is given. The dependence of the coefficients on different parameters such as forecast horizon, time of day and day of year is displayed.

The dependency of the coefficients on the forecast horizon is displayed in fig. 5.11, from 0 (i.e. the time of forecast computation) to 5 hours ahead, for singles sites (left) and all sites' averages (right). For horizon 0, the P_{pers} is weighted with $a = 1$ (with $b = c = 0$), as here the measurement naturally is the perfect match. For single sites, the persistence forecasts' weight significantly reduces within the 30 minutes-horizon. At 15 minutes, CMV forecasts already are rated higher than the persistence (with $b \approx 0.55$, $a \approx 0.35$ and $c \approx 0.10$). From horizons of 3 hours onward, NWP forecasts dominates the combined forecasts, rated equally with CMV forecasts ($b \approx c \approx 0.5$) between 2 and 3 hours horizons. For all horizons greater than 0 evaluated here, combined forecasts include rates of all forecast approaches involved. That includes on the one hand NWP at 15 minutes ($c \approx 0.1$) and persistence forecasts at 5 hours ahead ($a \approx 0.1$).

When comparing the coefficients of the combined forecasts for all sites' averages to single sites, main differences between the weighting coefficients are visible in the horizon dependency. A much higher rate of the persistence forecast is displayed for all forecast horizons, dominating the combined approach for up to two hours ahead. This is a consequence of the better performance of spatially averaged persistence forecasts. For horizon 5 the rating of persistence is still around $a = 0.25$. From around 2.5 hours ahead, the CMV forecast is rated the highest; from around 3.5 hours onward, the NWP again dominates the combined forecasts.

The dependency of the coefficients on the time of day (fig. 5.12 left, for single sites) also reflects the diurnal dependency of the forecast approaches' rating. As CMV forecasts usually show higher rmse for high solar zenith angles, this leads towards a comparable low rating in the combined forecasts for these hours. In these cases, the persistence (for 15 minutes) and the NWP-based forecasts (for 2 hours horizon) are rated higher. The diurnal course of the fit coefficients is less pronounced for the 2 hour than for the 15 min forecast horizon. For 2 hours ahead, persistence, CMV and NWP show only little changes in rating after 10 UTC here. For the 15 min horizon, the NWP also features only small changes in the range from 0.08 to 1.8, but the persistence and CMV rating varies to a high extent, from 0.4 to 0.8 for the persistence and from 0.14 to 0.5 for CMV.

The change of the weights during the year is displayed in the right panel of fig. 5.12. As stated in sections above, the rmse of CMV forecasts is usually higher in winter months, reflected by a comparable low rating for the days of year 0 to 100 and from 300 onward. This is valid for all forecast horizons displayed with declining characteristics for the larger forecast horizons. For the weighting of the NWP forecasts, no significantly annual trend is shown, a slight decrease in its rate can be observed for winter days. For these months, the persistence is weighted higher than for the summer, being a consequence of two aspects: The decline in the performance of the CMV in winter and the impact of snow-covered modules. For snow cover, the persistence forecasts would proof to be more accurate, which is reflected by the weight coefficients trained in winter months. As snow cover not necessarily occurs for all modules at the same time and not persistently over a long period, considering its impact by the coefficient training is not sufficient: Single days with snow cover cannot be adapted accurately to by this training; moreover, the other way round, a higher amount of days with snow cover would affect the coefficients also for days without and lead to a higher rating of the persistence forecasts than usual.

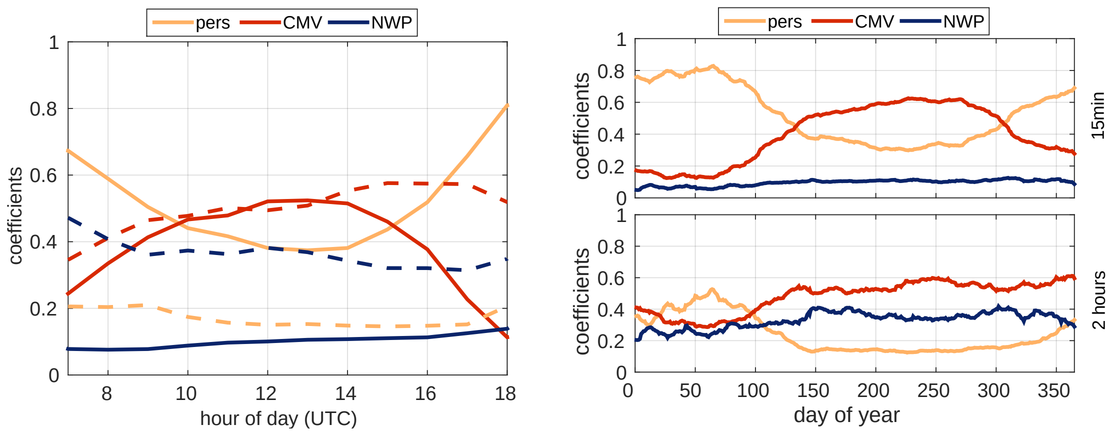

Figure 5.12.: Left: Fitting coefficients in dependence on the time of day for forecast horizons 15 minutes (solid lines) and 2 hours (dashed lines), for months May to July 2013. Right: Fitting coefficients for single sites in dependence on the day of year 2013 for forecast horizons of 15 minutes (top) and 2 hours (bottom), for noon hours (10 to 12 UTC).

5.5. Contribution of individual forecasts

In evaluations above, the combined forecast approach is based on P_{pers}, P_{CMV} and the P_{NWP} forecasts. In this section, different realizations of the combination approach with respect to the input data used is evaluated: Successively, each individual forecast (P_{pers}, P_{CMV} or P_{NWP}) is excluded from the combination approach and the response of the combined forecast accuracy evaluated. By this, the relevance of each single approach in the combined forecast is shown. Resulting are three two-components-forecast realizations, which are compared to the combined forecasts using all three components in fig. 5.13.

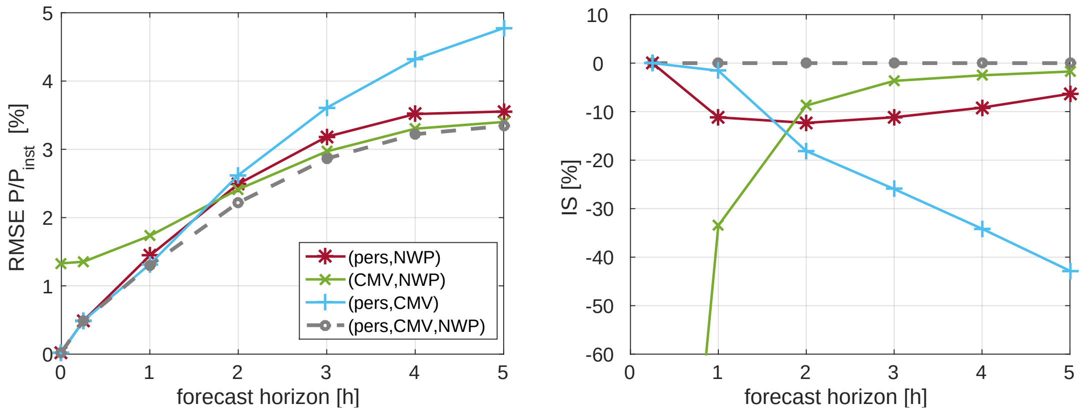

Figure 5.13.: Comparison of the rmse (left) and the Improvement Score (right) of two-component combined forecasts in relation to all three forecast models included. Data set: Apr-Nov 2013, 921 sites averages, 15 minutes values, no restrictions to solar zenith angles.

In general, the forecast rmse increases when based on only two components, to different extents depending on the component not included as well as on the forecast horizon. Naturally, the rmse increases most for those horizons, the component not included is weighted highest according to section 5.4. But all other horizons are also affected, except for the 15 minutes ahead forecasts when using persistence with CMV or with NWP only. For example, combined forecasts without the persistence forecasts included, show an $IS \approx -34\%$ for the 1 hour forecasts, but also still of $IS \approx -2\%$ for the 5 hours forecasts. Not using CMV forecasts affects all forecast horizons between 1 and 4 hour by more than 10% increase in rmse. Forecast combination without NWP-based forecasts affect later forecast horizons of 2 hours and more by up to 42%.

In general, all individual forecast approaches are relevant to the combined forecast quality. For the most relevant 2 hour forecast horizon, the rmse increases between 9% and 18%, with persistence the lowest and NWP the highest impact; not including CMV forecasts leads to an increase of rmse by 12% for the 2 hour forecast horizon.

5.6. Delayed availability of measurements or forecasts

The approach presented above takes into account online PV power measured close to the time of forecast calculation. When considering operational forecasting, measured data is often not immediately available. Data processing times are always an issue causing a delay in data availability, as for measured power e.g. the data collecting and processing consumes time. Also the availability of CMV forecasts may be subject to delay caused by processing times or missing images on some occasions. As the presented approach of short-term forecasting utilizes forecast data generated close to the forecast valid time, this aspect influences forecast quality. In this section a quantification of the impact of a delay in measurements or CMV forecasts is given. This delay is simulated from 0 minutes (the ideal case) to 2 hours and any combination thereof. As NWP forecasts are naturally aiming at larger forecast horizons and are available with high reliability, for these forecasts no delay is simulated. The impact is shown with respect to the combined forecasts' rmse (table 5.2) and to the change in fit coefficients (fig. 5.14). The reference is the (0,0)-delay, as evaluated in all sections above.

In general, with the delay in the availability of persistence or CMV forecasts, the rmse of the combined forecasts increases and the fit coefficients change. Its extent depends on the forecast horizon and if for single sites or all sites' averages. The higher the rate of the method concerned is in the combined forecast, the stronger the sensitivity of the combined forecast is towards delays. For example, for single sites 15 minutes forecasts the rate of persistence forecasts within the combined forecasts drops quickly with increasing measurement delay; the rmse increases by more than 20% from 0 to 2 hours delay of measured PV power. For the 2 hours forecasts with little initial share of the persistence forecasts, the rmse increases only by around 3%. In this case, the delay of CMV forecasts has a higher impact, a delay of 2 hours increases the rmse by around 10%.

For all sites' averages, with an initially higher share of persistence forecasts also for later forecast horizons, persistence forecasts have much higher shares in the combined forecasts even for larger delays. However, the combined forecasts' rmse responds stronger to delays in persistence forecast availability than for the CMV, both valid for the 15 minutes and the 2 hour forecast horizon. Generally, the steeper the increase of rmse with forecast horizon of the initial combined forecast (fig. 5.9), the higher the modification of the forecasts coefficients is with increasing delay. For all sites' averages with a general higher relative increase in rmse with forecast horizons, modifications of the fit coefficients responds much stronger towards delays.

The delay of the availability of persistence or CMV forecasts leads to a higher rating of the other approaches within the combined forecasts. This depends on the initial rating of the replacing forecast approaches for the corresponding forecast horizon. For single sites 15 minutes forecasts, the delay in persistence forecasts availability leads to a higher rating of the CMV-based forecasts, but almost no change in the contribution of the NWP forecasts' share. With CMV forecasts' delay, both the contribution of persistence- and NWP-based forecasts increases. Concerning all sites' averages for both, 15 minutes and 2 hours forecast, delays in persistence tend to be compensated for by higher shares of CMV forecasts and vice versa. This is a result of the NWP forecasts showing small initial contribution at these forecast horizons, compare to fig. 5.11.

Table 5.2.: rmse of P/P_{inst} for combined forecasts with delayed measurements or CMV forecasts, for single sites (top) and all sites' averages (bottom), for 15 minutes (left columns) and 2 hours (right columns) ahead. Dataset: Apr–Nov 2013, 921 sites, 15 min resolution.

		single sites, 15 min					**single sites, 2 hours**				
RMSE		delay measurement					delay measurement				
$P/P_{inst}[\%]$		0min	15min	30min	1h	2h	0min	15min	30min	1h	2h
delay CMV	0min	6.94	7.74	7.92	8.10	8.55	10.98	11.04	11.06	11.12	11.28
	15min	7.21	8.15	8.35	8.53	8.99	11.23	11.30	11.31	11.36	11.51
	30min	7.42	8.52	8.78	8.97	9.43	11.45	11.53	11.51	11.55	11.67
	1h	7.71	9.03	9.42	9.67	10.15	11.78	11.88	11.89	11.86	11.93
	2h	8.11	9.62	10.14	10.51	11.13	11.99	12.09	12.15	12.23	12.28

		all sites' averages, 15 min					**all sites' averages, 2 hours**				
RMSE		delay measurement					delay measurement				
$P/P_{inst}[\%]$		0min	15min	30min	1h	2h	0min	15min	30min	1h	2h
delay CMV	0 min	0.67	0.85	1.03	1.28	1.51	2.50	2.57	2.62	2.67	3.29
	15min	0.71	0.88	1.09	1.39	1.62	2.72	2.79	2.84	2.93	3.35
	30min	0.72	0.90	1.15	1.50	1.78	2.64	2.73	2.79	2.89	3.38
	1h	0.92	1.10	1.36	1.76	2.07	2.63	2.75	2.85	3.00	3.36
	2h	1.31	1.49	1.73	2.20	3.33	2.54	2.72	2.87	3.11	3.54

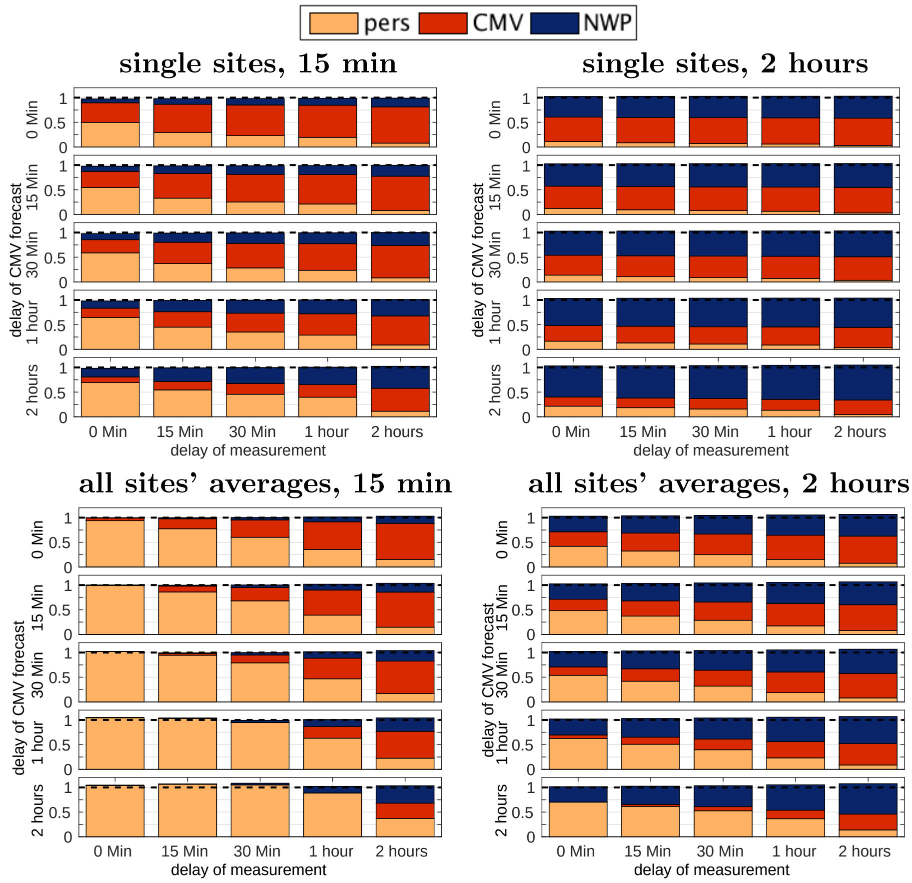

Figure 5.14.: Fit coefficients for delayed measurements or CMV forecasts for single sites (top) and all sites' averages (bottom) with a forecast horizon of 15 minutes (left) and 2 hours (right). Dataset: Apr–Nov 2013, 921 sites, 15 min resolution.

In an operational context, for forecasts of short lead times, the timely availability of data required for forecasting as well as a short computation times are essential. The value of the contribution of persistence or CMV forecasts within the combined forecasts rapidly decreases with delays in the availability of the corresponding forecasts. Especially, if unavoidable, delays in availability have to be considered in forecast weighting when computing the combined forecasts.

5.7. Conclusion

In this chapter, an approach for combining PV power forecasts from satellite data and numerical weather predictions with online measured PV power is introduced. These combined forecasts lead to a reduction of forecast rmse by e.g. 10% for single sites and 50% for all sites' averages with respect to forecast horizons of two hours ahead. The combination is achieved by a linear regression approach trained at measured PV power for the preceding days. The approach is optimized by rating the improvement through the combination approach for different configuration of parameters: best results are obtained when the individual methods are rated depending on the time of day. Measured PV power, CMV and NWP forecasts contribute to the combined forecasts to different extents with respect to the forecast horizon, time of day and season. In Wolff et al. (2015) [86], this approach is compared to an approach based on advanced statistical methods (Support Vector Regression): Similar results for both methods are observed.

6. Upscaling to regional forecasts

The assessment of the regional PV power feed-in of all PV plants is relevant for the control areas of the transmission system operators as well as for whole of Germany (see chapter 2). By end of 2014 in Germany around 1.5 million PV systems were registered. Computing PV power forecasts for all installed PV systems in these regions is associated with unfeasible and unnecessary efforts with respect to computational costs and availability of PV system information or measurements. Only information on the post code and installed capacity of every single system is included in the RES site-specific data. Information on the relevant system configurations such as tilt angle and orientation are lacking, essential for an accurate PV power simulation (see chapter 4). Regional forecasts are derived using an upscaling method, as proposed in Lorenz et al. (2014) [23] and Lorenz et al. (2011) [20]. Comparable methods are widely used also for wind power feed-in forecasts, see e.g. Ernst et al. (2007) [7]. The upscaling algorithm defers the feed-in for a whole region from a representative set of single PV plants with good knowledge about the systems' configuration. These single sites have to be representative with respect to the spatial distribution of all sites (longitude and latitude), to the system configuration (tilt and azimuth angle of the modules) and to the distribution of installed capacity. In this chapter a model is developed to find criteria for selecting representative sites for an optimized upscaling. This upscaling algorithm is applied to PV power forecasts, as well as to measured PV power to obtain projections of the actual PV power feed-in.

In section 6.1 the upscaling method is introduced. The datasets used and evaluation settings applied in this chapter are described in section 6.2. The model development for the upscaling algorithm matching the regional feed-in is described in section 6.3. Results from this are transferred to a validation with an external reference using the RES PV power feed-in time series in section 6.4. The forecast accuracy after applying the upscaling method is analyzed is section 6.5, giving an overview on the achievements by introducing different forecast methods for short-term intraday forecasts.

6.1. Upscaling approach

With the upscaling algorithm, the overall PV power feed-in P_{all} of all plants in a region is modeled. The upscaling of the PV power feed-in is performed by simulating the PV power for representative systems with the ratio f of overall installed capacity $P_{inst,all}$ for the region of interest and of the installed capacity of the representative dataset $P_{inst,rep}$. The overall upscaled power feed-in P_{scale} is thus derived as:

$$P_{scale} = f \cdot P_{rep} = \frac{P_{inst,all}}{P_{inst,rep}} \sum_i P_{rep,i} \tag{6.1}$$

Here, a good level of agreement between the spatial distribution of the representative and the overall dataset is essential [20]. As the representative set is dependent on the available monitored PV sites do not necessarily feature the same spatial distribution as the PV systems in the overall system, a detailed upscaling procedure was introduced in Lorenz et al. (2011) [20]. In this approach, the spatial distribution and variation of the installed capacity of the PV systems is considered with more detail by introducing an upscaling factor $f(\phi, \lambda)$ in dependence on the latitude φ and λ of a $1° \times 1°$ grid. Within each grid cell, all PV sites are pooled and their contribution to the overall feed-in is rated with a weighting factor depending on the installed capacity of all sites in this cell. This detailed upscaling has shown that the accuracy of the upscaling algorithm increases when the spatial distribution of the representative PV sites compared to all sites in the dataset is considered [20].

In this thesis, a further development of the presented method is performed, which takes information on the systems' tilt and azimuth angle into account. The consideration of tilt and azimuth angle not included in the RES data is performed by introducing different classes γ of PV system sizes. Each class shows a characteristic distribution of tilt and orientation of PV models, significantly influencing the power feed-in characteristics (see e.g. fig. 5.2 in section 5.1.1). For instance, large PV systems in Germany usually show tilt angles around 30° and an optimal south-faced orientation, small rooftop installations show a higher variety of both angles. As tilt and azimuth angle information is not included in the RES dataset, this characteristic information is deduced from the *meteocontrol* dataset for each chosen system class. Here, the assumption is made, that classes of system sizes have a similar distribution of tilt and azimuth angles. For the description of the regional distribution of the PV sites, post code area information is used. This information is the highest spatial resolution of the PV sites' location provided by the RES system specific information. Here, several post code areas close to each other are grouped to clusters ψ.

Each system class γ in each regional cluster ψ defines the subclass $C(\psi, \gamma)$. The normalized power feed-in of representative sites $P_{rep,i}(t)/P_{rep,i,inst}$ in each subclass is averaged and weighted with the sum of installed capacities $P_{inst,all}(\psi, \gamma)$ of all sites in this subclass. The upscaled power P'_{scale} is formulated as the sum of the power feed-in for all subclasses:

$$P'_{scale}(t) = \sum_{C(\psi_k,\gamma_k)} \left[P_{inst,all}(\psi_k, \gamma_k) \cdot \frac{1}{R_k} \sum_{\substack{i \in \\ C(\psi_k,\gamma_k)}}^{R_k} \frac{P_{rep,i}(t)}{P_{rep,i,inst}} \right] \tag{6.2}$$

with $P_{rep,i}$ measured or predicted power for a site in the representative dataset.

The following model development aims at the optimization of the subclass configuration: On the one hand, a highest possible resolution of system classes and regional cluster is intended. On the other hand, a sufficient amount of representative sites have to be available in each subclass as the representation dataset is limited.

This so defined upscaling algorithm is applied to the measured or predicted PV power: When applied to measured PV power, a projection of the PV power feed-in in the corresponding region is derived. For PV power forecasts, the regional PV power feed-in is predicted by this approach.

6.2. RES datasets

The installed capacity for all PV systems per subregion and system class is important information for the presented upscaling approach. By this data the correct system class dependent distribution of the PV sites is derived. For Germany, all PV (and other RE) sites have to be registered according to the RES (Renewable Energy Source Act, Erneuerbare Energien Gesetz EEG, [33]). There, installed capacity, the location with a post code resolution, and the date of initial operation are registered for each station. No further information such as the tilt or azimuth angles or any other technical specification are available. The RES datasets were published on a regular basis by the TSOs ([55, 56, 57, 58], after August 2014 by the Federal Network Agency (Bundesnetzagentur) [102]. From this **RES system specific information**, following information needed for the upscaling approach is derived:

1. The installed capacity $P_{inst}(\psi, \gamma)$ per subregion ψ and system class γ,
2. The overall installed capacity P_{inst} for each control area/Germany.

The development of the installed capacities P_{inst} for each TSO as derived from the RES system specific information is presented for January 2012 to December 2013 in fig. 6.1. Except for the TransnetBW dataset, the figures are given with a monthly resolution derived from the information on the installation date. For TransnetBW, only the end-of-year reports are available and the monthly installed capacities interpolated linearly from this. For all control areas, an increase of PV power capacities with some leaps in 2012 is visible.

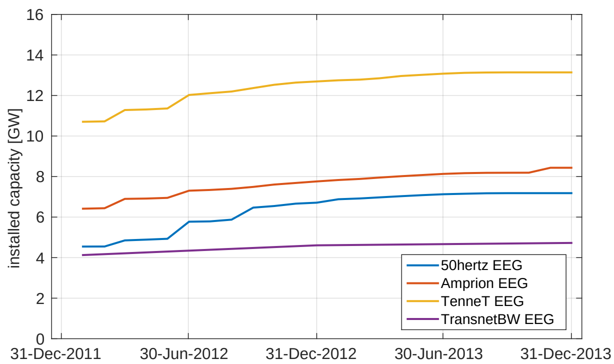

Figure 6.1.: Development of the installed capacity P_{inst} for each control area, from end of December 2011 to end of December 2013. Data source: RES datasets ([55, 56, 57, 58]).

The projections of power feed-in and VRE power forecasts for all control areas are mandatorily published [33] in regular intervals by the TSOs on the European Energy Exchange transparency portal [59] or at [103] (see also fig. 2.3) as **RES feed-in time series**. Among others, the expected and actual solar power generation is published with 15 minutes temporal resolution for each TSO seperately. This published data is based on projections by different providers: Each provider performs an upscaling procedure using measured PV power based on their individual models. As a consequence, this information does not necessarily reflect the actual power feed-in, but only represents the projection of feed-in based on different models.

6.3. Model development

The configuration of the upscaling algorithm according to equation 6.2 is derived in this section, addressing the representation of system classes and the regional distribution.

6.3.1. Dataset for model development

The RES feed-in time series introduced above is not suitable for model development as the models' accuracy would only be rated compared to the estimations of providers but not real feed-in data. For model development, a closed environment is therefore created, with best possible knowledge of the overall power feed-in. This overall power feed-in P_{all} can be the feed-in of all PV sites in a control area or Germany or any other system that has to be modeled by the upscaling algorithm. For upscaling, the overall feed-in of a number N of PV systems has to be modeled by referring to a subsystem with M systems. Or, in terms of installed capacities, the feed-in of sites with an overall $P_{inst,sum}$ has to be modeled by a subsystem of sites with $P_{inst,rep}$.

The overall feed-in of all $P_{sum} = \sum_i^N P_i$ sites has to be reproduced as good as possible by a subsystem of $M \ll N$ sites from the same dataset, with $P_{rep} = \sum_k^M P_k$. The advantage of this approach is the best knowledge of $P_{all}(t) = P_{sum}(t)$. Taking a smaller subsystem to model the feed-in of the whole set emulates the upscaling approach using representative sites to model the overall power production. The configuration of the upscaling approach is assumed to be transferable to other datasets, for example of modeling on the overall feed-in in Germany or the control areas. However, due to the limited amount of PV sites in the dataset with measurements available, results may not be transferable without restrictions: For example, for modeling the overall power for Germany according to the RES feed-in data, all representative sites in the *meteocontrol* dataset can be used; for model development referring to the sum of all sites in the same dataset, the subsystem has to be much smaller.

For model development, the dataset 'A' of measured PV power (see section 4.1) is used for modeling the upscaling approach, containing a total of 1348 sites, but with lower data availability than the datasets used above. This is done as a high spatial distribution is of more importance than temporal data availability. Time steps with more than 10% missing measured data points are rejected entirely from evaluations. The dataset from May to November 2012 is used.

6.3.2. Concept of model development

The upscaling rmse of modeling $P_{sum}(t)$ of all N sites in the dataset by $P_{scale}(t)$ of a subsystem with M stations is displayed in fig. 6.2 in dependence on the size of subsystem. In this case, the upscaling algorithm does not consider any regional or system size classification. The M sites are randomly selected and the median rmse as well as the standard deviation of the rmse for 100 different randomly generated realizations displayed in dependence on the subsystem size. Figure 6.2 contains two different realizations of the upscaling algorithm:

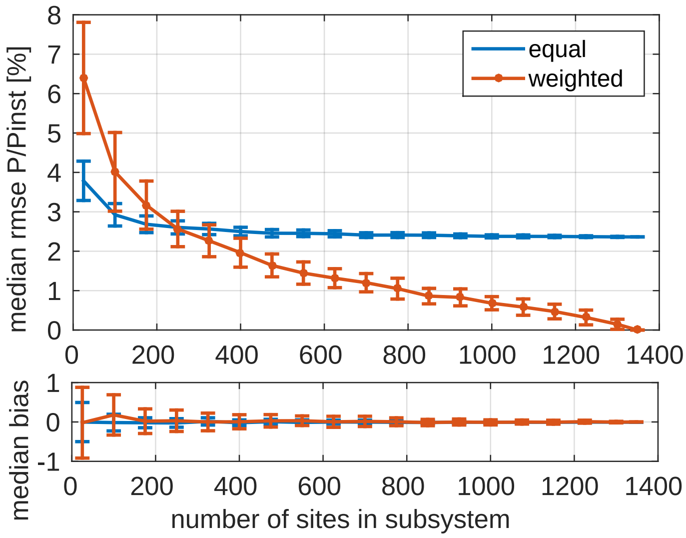

Figure 6.2.: Representation of the power feed-in of the overall system with N sites by subsystems of size M. Displayed is the median rmse and the standard deviation for 100 randomly generated realizations of the subsystem compilation. Dataset: May–Nov 2012, 1348 sites, 15 min resolution.

- Simple sum of each station in the subsystem (orange line)

$$P_{scale,weighted}(t) = P_{inst,sum}/P_{inst,rep} \sum_i^M P_i(t)$$
$$\text{with } P_{inst,rep} = \sum_k^M P_{inst,rep,i} \text{ and } P_{inst,sum} = \sum_i^N P_{inst,i}$$

  The median rmse decreases with increasing number of sites M in the subsystem. Also, the standard deviation follows the same trend: It is highest for small number of sites, as the accuracy for different realizations is strongly dependent on which specific sites are selected by the algorithm and their installed capacities. Naturally, for the subsystem with size $N = M$, the rmse and standard deviation both are 0, as the subsystem is equal to the overall system in this case.

- Equally weighting each station (blue line)

$$P_{scale}(t) = P_{inst,sum} \cdot 1/M \sum_i^M P_i(t)/P_{inst,i}$$

  In this case for $N = M$, the total $P_{sum}(t)$ is not modeled perfectly, as without weighting each site the distribution of the installed capacity and characteristic feed-in of the sites is not reflected in this upscaling approach. This approach leads to a better representation of $P_{sum}(t)$ for smaller subsystems, up to a subsystems' size of $M = 250$, being around 20% of all sites in the system N. The standard deviation between the different realizations is smaller than for the weighted approach: For weighting equally, the installed capacity of the randomly selected sites does not have an impact. In contrast to the weighted approach, adding more stations in the representative set does not further reduce the upscaling rmse above a certain threshold at around $M = 600$.

This approach of equally weighting all sites in a subclass is used in the following upscaling approach, as the ratio of number of sites in the representative set to the number of sites in the overall system is small: For the RES dataset, 1.5 million PV sites have to be modeled by typically a few thousand sites in the representative system: For the dataset 'A', the number of sites is 1348, making up not more than 1%; with respect to the installed capacity, the dataset contains 500 MWp which is about 1.6% of overall PV capacity in Germany. In this model development environment, using less than 1% of the sites would be not applicable at all, as not sufficient sites would be available for each system classes and subregion. A subsystem size of $M = 200$ (15% of the overall datasets' size) is used as reference value.

6.3.3. Representation of system classes and regional distribution

The amount of subclasses $C(\psi, \gamma)$ is defined by the amount of subregions ψ and system classes γ. On the one hand, a high resolution of both is beneficial for the upscaling process, but at the same time is limited by the number of sites in the representative dataset used. Building subclasses $C(\psi, \gamma)$ has to be done leaving a sufficient amount of representative systems in each subclass.

Considering the systems' configuration within the upscaling process enables a better description of the actual PV power feed-in. With respect to the tilt and azimuth angle of a PV system, the characteristics of power feed-in differs significantly. As information on the tilt and azimuth angles is not available from the RES dataset, this information has to be deduced from available information. From analysis of the *meteocontrol* dataset (see section 4.1) different system classes with respect to the installed capacity show characteristic distributions in tilt and azimuth angles. This dataset is assumed to match characteristics of different system classes which can be transferred to the RES dataset. Here, four classes with characteristic differences are distinguished (see fig. 6.3 and 6.4) and all possible combinations of these system classes are compared:

- $0 < P_{inst} \leq 30$ kWp small, presumably mainly rooftop installed systems, with high variation in tilt and orientation;
- 30 kWp $< P_{inst} \leq 1$ MWp medium sized systems, moderate variation in tilt, high variation in orientation, with a comparable high share of low tilt angles,
- 1 MWp $< P_{inst} \leq 5$ MWp large systems, with optimal south-facing orientation installed modules and various tilt angles,
- 5 MWp $< P_{inst}$ big solar parks with optimal south-facing orientation and tilt angles $\beta \approx 30°$.

For finding the best regional configuration, the resolution of the post code areas (left panel in fig. 6.5) is reduced to two-digit post code areas (dots in center and right panel of fig. 6.5). Clusters of regions are constructed by pooling post code areas close to each other. This is done for different numbers of clustered regions, from 1 to 50. In the centre panel of fig. 6.5, 5 different clustered regions, and in the right panel, 10 different clustered regions are exemplarily displayed.

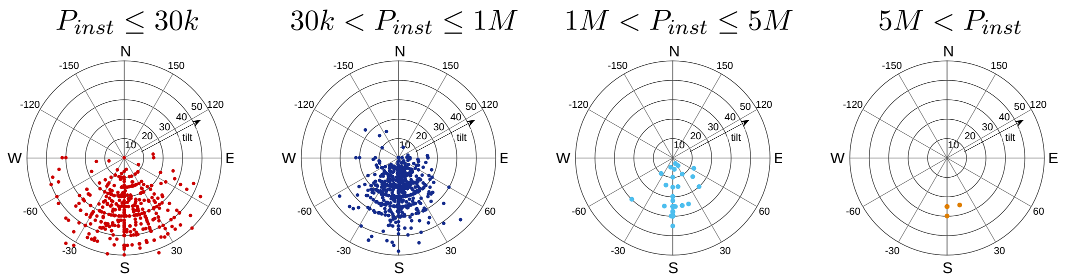

Figure 6.3.: Polar plots of the distribution of tilt angle β (represented by the radius, horizontally aligned corresponds to $\beta = 0$) and azimuth angle ϕ (displayed as angle, with $\phi = 0°$ corresponding to south), for classes of installed capacity in W_p.

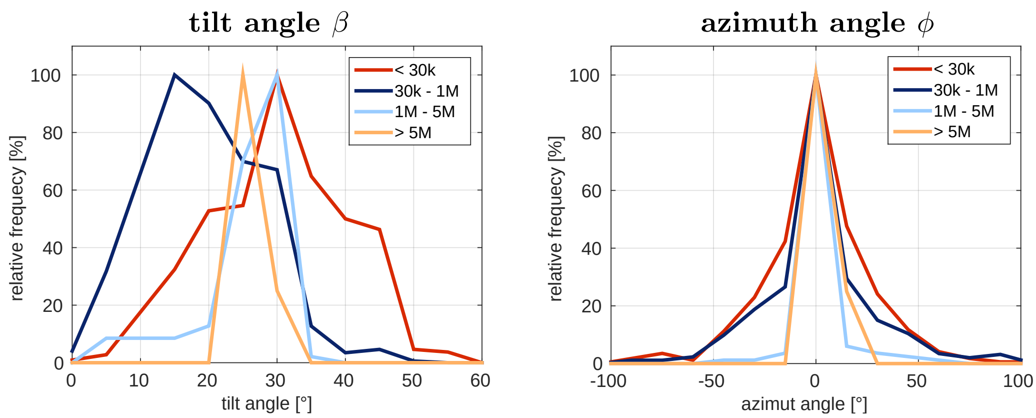

Figure 6.4.: Normalized frequency distribution of tilt (left) and azimuth angles (right) for the system classes of installed capacity in W_p, normalized to the maximum occurrence of each class. The bin size is 5°.

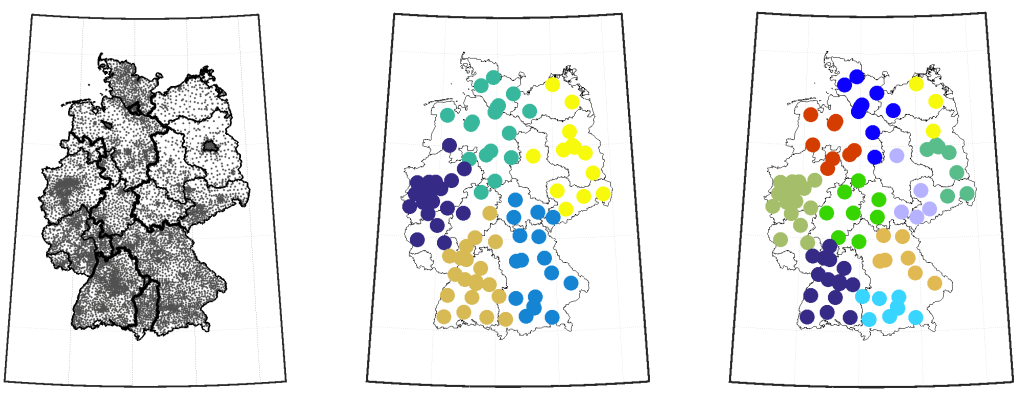

Figure 6.5.: Left: Spatial distribution of all post code areas in Germany, defining the maximum resolution of the RES dataset. Centre and right: Accumulation of post code areas to two-digit post code areas (each circle), clustered in 5 (centre) or 10 (right) areas for pooling the PV sites.

6.3.4. Configuration of the upscaling model

The best configuration is determined based on different system classes and region sizes, as introduced above. The analysis is performed based on measured PV power. For each possible configuration, the median rmse and the rmse's standard deviation for 100 different realizations according to stations selected per region and class are derived. These realizations are computed randomly as done in previous section 6.3.2. By this, the dependency of the upscaling rmse on which specific site is used in the representative dataset is considered.

For each number of clusters used, the optimal clustering is determined individually, see e.g. for 50 clusters in left panel in fig. 6.6:

1. Clusters are constructed with a 'k-mean' approach, minimizing the distance of all 2-digit post code areas within each cluster by latitude and longitude information.
2. This approach is repeated 100 times with random initial conditions of the k-mean algorithm, leading to different realizations of clustering (grey lines in fig. 6.6).
3. The realization with a minimal median rmse at the size of the representative set of $M = 200$ is chosen as best realization of clustering (black line in fig. 6.6).

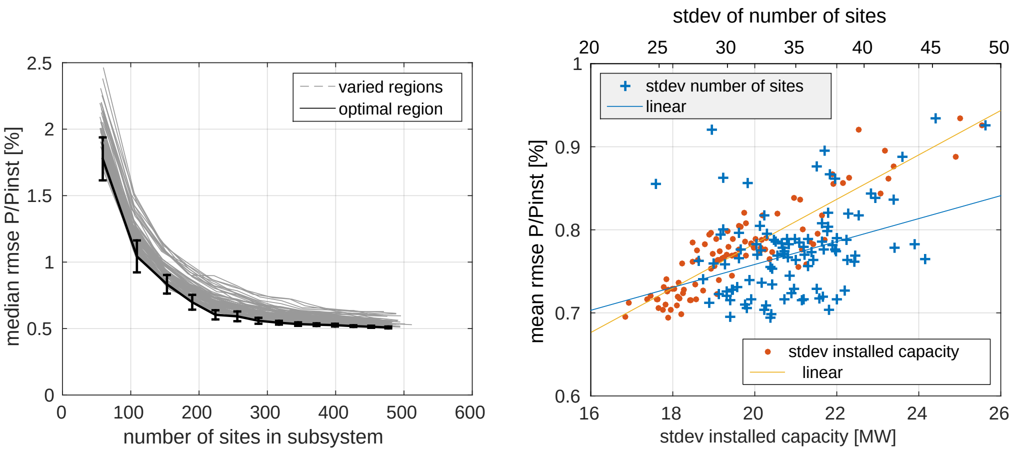

Figure 6.6.: Left: Median rmse of upscaling algorithm using 50 clustered regions in dependency on the size of the subsystem. The black line indicates the configuration with the minimum median rmse and its standard deviation, selected for following evaluations. Right: Dependency of the median rmse at $M \approx 200$ sites in the subsystem, for each of 50 clusters versus the standard deviation of installed capacities (lower x-axis) or of the number of sites (upper x-axis) per region. Dataset: May–Nov 2012, 15 min resolution.

The mean upscaling rmse of differently clustered regions are displayed in right panel of fig. 6.6 in dependency on the standard deviation of the amount of sites per region (upper x-axis) and the standard deviation of the sum of installed capacity per region (lower x-axis). This enables to derive criteria for selecting the best regional clustering: A low standard deviation of the corresponding feature indicates a more homogeneous distribution of number of sites or sum of installed capacity among the different regions. A linear fit of the upscaling rmse is shown for both cases, but with higher correlation in dependency on the sum of installed capacity: Choosing regional clusters of similar size with respect to the overall installed capacity is beneficial for the upscaling approach.

The impact of selecting different numbers of clustered regions on the upscaling rmse is displayed in fig. 6.7 for measured PV power. Here, the upscaling rmses for one to 50 clustered regions are compared, each with the best configuration as shown above (fig. 6.6). For one region an median upscaling rmse decreases from around 3.6% for 50 sites in the subsystem to around 2.5% for above 600 sites in the subsystem. For 5 regions, this decreases to between around 3% and 2%. Using more clustered regions further reduces the median rmse but with less relative improvement: For 50 regions the upscaling rmse is around 1.3% for 400 and more sites in the subsystem, whereas for 10 regions it already is around 1.5%. In the range of $M \leq 200$, increasing the number of regions is not beneficial and even shows higher upscaling rmse especially at $M \leq 100$: By increasing the amount of regions, the number of sites per region is significantly reduced (for $M = 50$ even to only one site per region). This leads to an increase in upscaling rmse when using multiple classes and regions but a small amount of sites within the representative dataset.

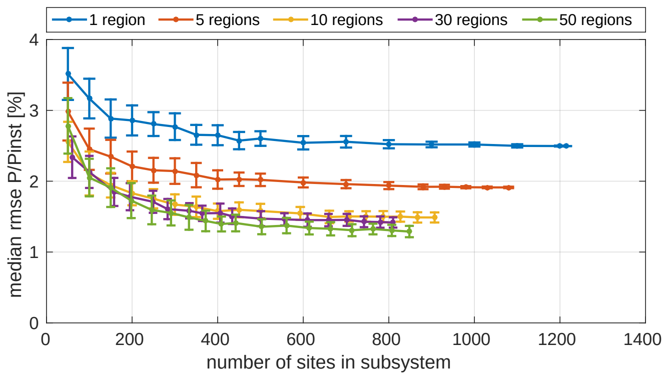

Figure 6.7.: Median and standard deviation of rmse of $P_{scale}/P_{inst,scale}$ compared to $P_{sum}/P_{inst,sum}$ for different amounts of clustered regions in dependency on the size M of the subsystem for 100 random realizations each. For each region size the best configuration of clustered regions is selected, see fig. 6.6, based on measured PV power. Dataset: May–Nov 2012, 15 min resolution.

The impact of selecting different system classes (see section 6.3.3) for 1 region is displayed in the left panel of fig. 6.8. For the dataset evaluated here, introducing two classes reduces the rmse, depending on the interval boundaries for these classes: The effect when applying a classes limit of 30 kWp is rather small (from a median rmse of around 2.9% to 2.8%, evaluated at $M = 200$). Significantly, for classes limits of 1 MWp ($\approx$ 2.15%) or 5 MWp ($\approx$ 1.35%), the reduction of the upscaling rmse is much higher. Lowest upscaling rmse is observed for three or four system classes configurations, with both a median upscaling rmse of $\approx$ 0.85%, favoring here configurations with interval boundary at 1 MWp and 5 MWp.

Same comparison but with taking 50 clustered regions into account is shown in the right panel of fig. 6.8. Similar behavior can be observed: Classes configurations with interval boundary of 1 MWp or 5 MWp show lowest upscaling rmse. However, due to the increased segmentation of the representative sites to regions and system classes, a high amount of system classes is not necessarily beneficial for the upscaling rmse: Taking no system classes into account (blue line, with $rmse \approx 1.6\%$ at $M = 200$ sites) shows lower rmse for the same amount of sites M in the subsystem than considering two classes

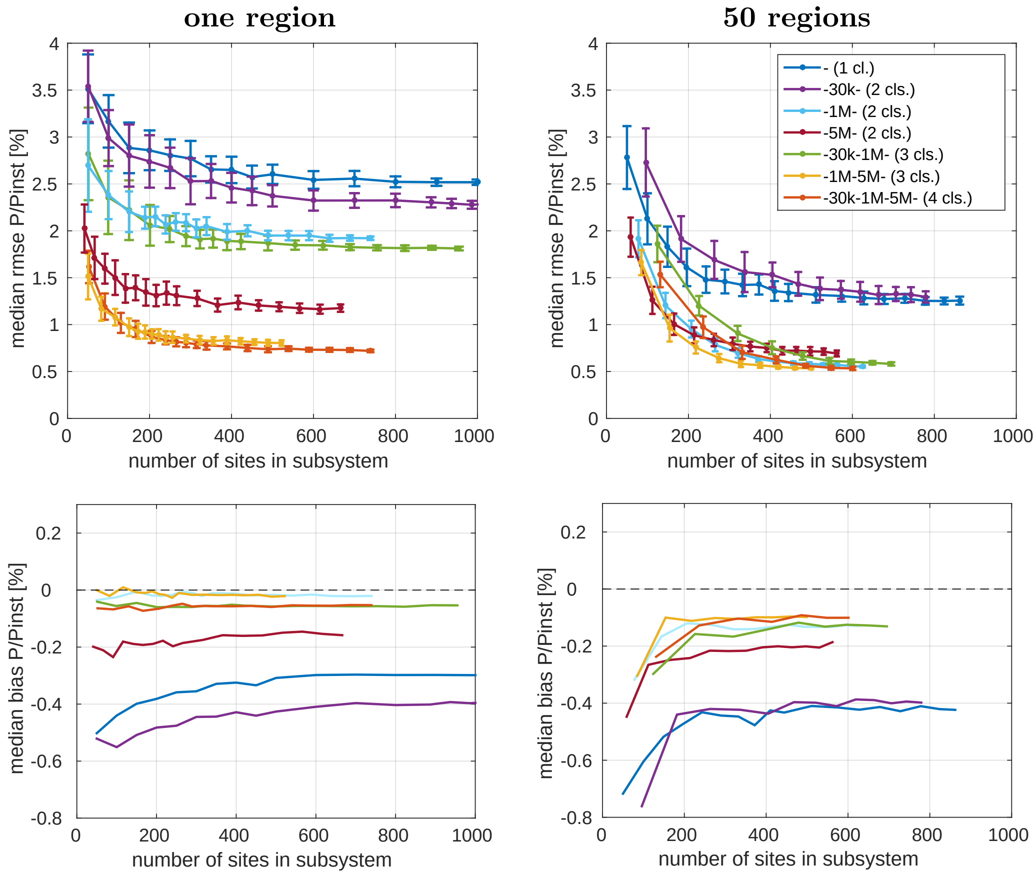

Figure 6.8.: Median rmse and standard deviation of rmse (top) and bias error (bottom) for 100 random realizations of the upscaling approach for different system classes, 1 region (left) and 50 clustered regions (right), in dependency on the size of the subsystem. Dataset: May–Nov 2012, 15 min resolution.

with interval boundary at 30 kWp (purple line, with ≈ 1.85%). Same is valid for the 3 and 4 classes configuration with one of the interval boundary at 30 kWp (green and orange lines, ≈ 1.4% and ≈ 1.2% respectively). Best results for this dataset can be observed for the 3 classes configuration with 1 MWp and 5 MWp interval boundaries.

In the bottom panels of fig. 6.8, the corresponding bias error is displayed: Here, all system class realizations are characterized with a negative bias error to different extents. Highest negative bias is found for realizations with only one or a few system classes involved. Not considering the differences between power feed-in depending on the system classes leads to an underestimation of power feed-in within the upscaling approach: For example, when weighting PV sites of all system classes equally, the contribution of larger PV plants with optimal south-facing orientation is not sufficiently represented.

6.3.5. Model configuration for PV power forecasts

In this section, the results of model development for measured PV are summarized for a fixed subsystem size and are transferred to PV power forecasts. The upscaling rmse applied to measured PV (left) and CMV 2h hour forecasts (right) is displayed in fig. 6.9, for a subsystem size of $M = 200$. The impact of different amounts of regions is emphasized and displayed for using one system class only and for the three system classes with boundaries at $P_{inst} = 1$ MWp and 5 MWp).

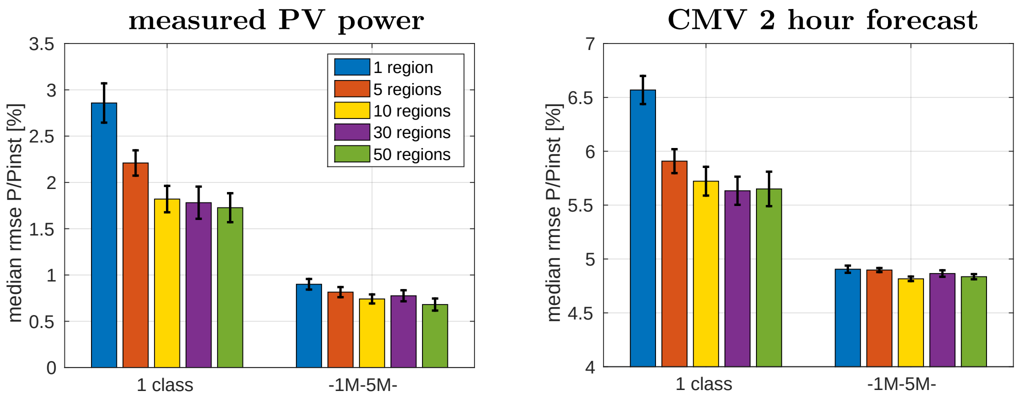

Figure 6.9.: Median upscaling rmse and standard deviation for different regions (1 to 50 clustered regions), for 1 system class (left columns) and 3 system classes (-1M-5M-, right columns) for a subsystem size of $M = 200$. Left for measured PV power, right for CMV 2h PV power forecasts. Dataset: May–Nov 2012, 15 min resolution.

The usage of multiple clustered regions and system classes reduces the upscaling rmse significantly, valid for both measured and predicted PV power. The impact of using multiple regions is largest for measured PV power when not differentiating between system classes. The differentiation of system classes further reduces the upscaling rmse: However, the impact of using multiple regions is smaller than in the case of one system class, contributing merely to an improvement of the rmse from 0.95% to 0.7% at $M = 200$, compared to 2.85% to 1.7% for 1 class only.

When based on forecasts (right panel in fig. 6.9), the overall rmse naturally increases as the forecast error is added to the upscaling error. Similar reduction of the rmse when using system classes and regional clustering is observed as for measured PV. However, the impact of using multiple regions is much less pronounced than for upscaling based on measured PV power. In this case, using 5 different regions or more leads to comparable results as for using one region only. Differences between best configuration with 10 regions and only one region are comparatively small (median upscaling rmse of 4.85% compared to 4.9%). This behavior can be a consequence of different interacting aspects: i) Using less regions leads to the averaging of feed-in over larger areas, which is beneficial for the application to predicted PV power, dominating the upscaling rmse. ii) The use of system classes already leads to an adequate representation of spatial distribution for the model development system used here, as the location of the few large sites within the subsystem are closely matched to the distribution in the overall system.

6.4. Application of upscaling to the RES datasets

The upscaling algorithm so far is developed and analyzed with respect to a closed system for model development with its own characteristic distribution of PV sites according to system classes and location. A transfer of the findings to the dataset valid for the situation in Germany is performed in this section. For this, a valid external reference for validation is hard to obtain, as the feed-in data available merely is based on projections by the TSO and forecast providers (see section 6.2).

6.4.1. Transfer of the upscaling configuration

The results shown up to this point are valid for the specific configuration within the dataset used for model development. Findings depend on the actual configuration of the overall dataset and its specific regional and system class composition.

Fig. 6.10 illustrates the differences between the distribution of the dataset used for model development (dark blue bars) and the RES dataset (see section 6.2, orange bars). Significant differences between both can be observed: The model development dataset contains a relatively high share of stations with $P_{inst} > 1$ MWp, whereas for the RES dataset only a minority of PV power sites can be found here, both valid in term of number of sites and overall installed capacity. The RES dataset shows a much higher share of small systems, which is not reflected within the model development dataset. For an optimal upscaling configuration, the model development dataset is artificially adapted to the RES dataset characteristics (light blue bars). This is done by reducing the amount of big systems with $P_{inst} > 1$ MWp and by increasing the amount of small systems with $P_{inst} \leq 1$ MWp, using existent systems of this size within the model development dataset multiple times.

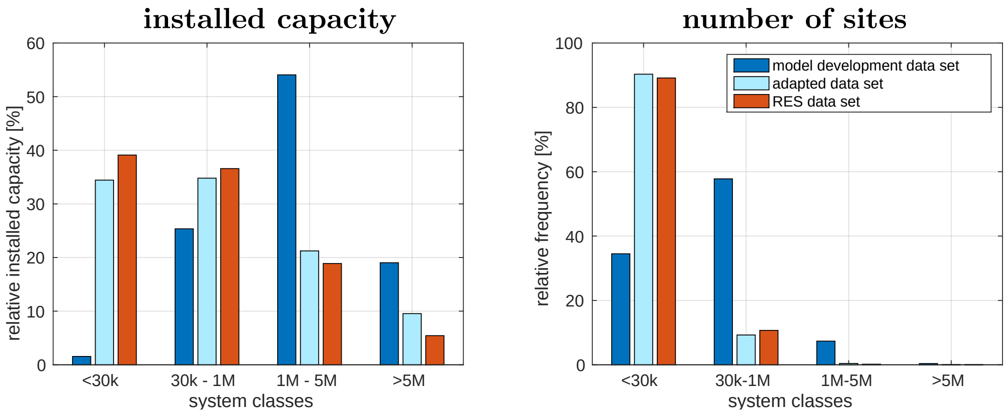

Figure 6.10.: Normalized relative frequency of installed capacities (left) and number of sites (right) for different system classes for the model development dataset (dark blue), for the RES dataset (orange) and an adapted model development dataset (light blue).

The resulting graphs with the upscaling rmse for the adapted model development dataset are displayed in fig. 6.11. In contrast to fig. 6.8, system classes featuring interval boundaries at 30 kWp show better performance than in the original model development dataset, where interval boundaries at 1 MWp and 5 MWp showed best performance. This is a direct consequence of the adaptation of the model development dataset, now showing a significantly higher share of smaller systems. For considering one regional cluster, best configuration is found using 4 classes with an upscaling rmse of around 1.1% at $M = 200$; for 50 clustered regions, using 2 or 3 system classes with 1 MWp being one of the interval boundaries show comparable results to the 4 classes configuration (around 0.80% to 0.85%). Here, the 3 system classes $-30k - 1M-$ configuration is chosen.

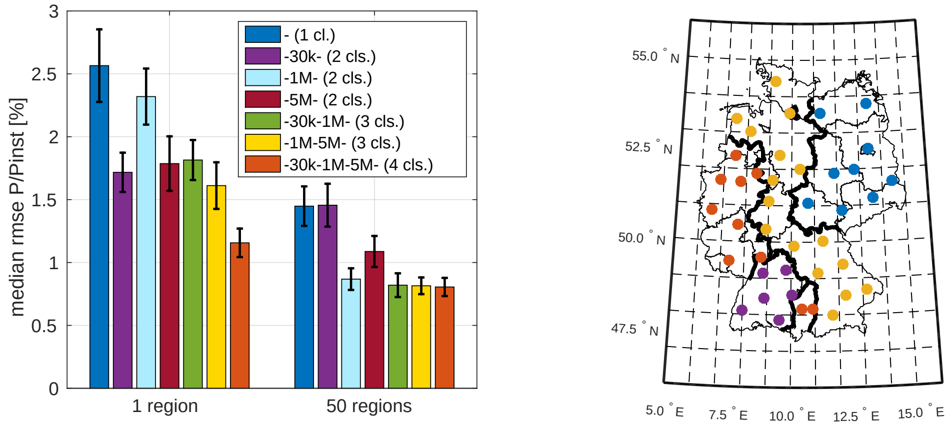

Figure 6.11.: Left: Median rmse and standard deviation of rmse for the upscaling approach for different system classes for subsystem size of $M = 200$, for 1 region (left set of columns) and 50 clustered regions (right set of columns), for the model development dataset adapted to the characteristics of the RES data (see fig. 6.10). Dataset: May–Nov 2012, 15 min resolution. Right: Regional distribution of 41 clustered subregions as derived for the RES dataset following the listed conditions.

When transferring the results on the RES dataset, following conditions to the regional clustering are resulting from the analysis above:

1. Including a sufficient amount of sites of each system class considered in each region,
2. at most homogeneous distribution of installed capacities among the regions (see right panel of fig. 6.6), determined by the standard deviation of installed capacity per region of the overall system.

For the definition of regional clusters for application, using an unambiguous assignment of regions and sites to one of the control areas is an additional constraint that has to be satisfied. According to these requirements, the resulting configuration for regional clustering is displayed in fig. 6.11, right panel.

6.4.2. Validation with RES feed-in time series

With this upscaling configuration adapted to the RES site specific information, the upscaling rmse is compared to the RES PV power feed-in time series in this section. This is done to give an evaluation of the upscaling algorithm with an external reference: The accuracy of the method in terms of rmse thus provides the comparison to the average projection from forecast providers and does not lead to valid statements concerning the quality of the upscaling method itself. The dataset has a temporal resolution of 15 minutes and is evaluated for the year 2013, the representative sites correspond to all 921 sites within the dataset 'C'.

The installed capacity $P_{inst,all}(\psi, \gamma)$ is derived for each subregion and system class using the information provided by the dataset of the RES system specific information, resolving the different post code areas and number of stations within the system classes. These factors are derived for the available data for June 2013. To consider the change in overall installed capacity for the control areas, these are factorized on a monthly basis with the corresponding data from fig. 6.1.

A frequency scatter plot is displayed in the left panel of fig. 6.12, comparing the upscaled power P_{scale} and the PV power feed-in based on the RES data for Germany, both normalized to the installed capacity. A good agreement of both is found, showing only a small scatter and a trend towards a slight overestimation of PV power feed-in.

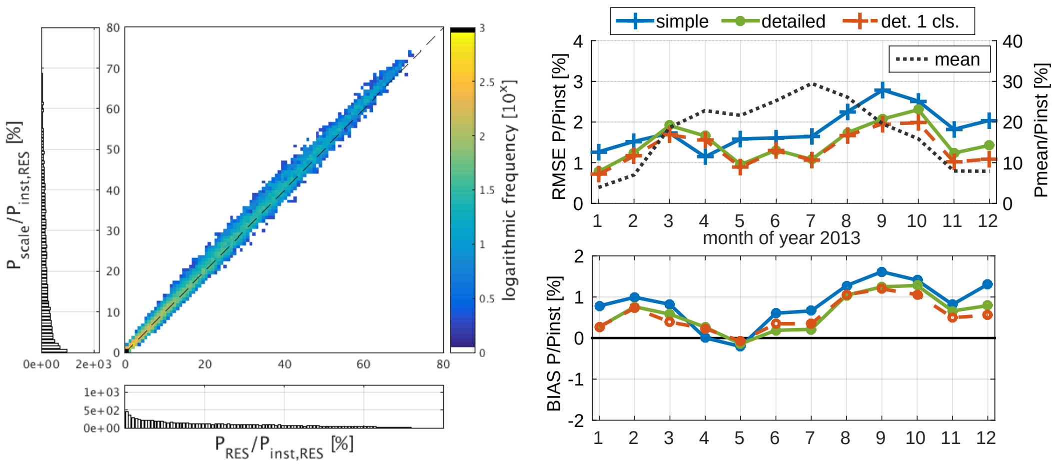

Figure 6.12.: Left: Frequency scatter plot for PV power feed-in for Germany from the RES dataset compared to feed-in derived from single site measurements using the upscaling algorithm introduced above. Right: Rmse of upscaling evaluated with respect to the PV power feed-in from RES data for all months in year 2013 and different upscaling configurations: 'simple', without considering system classes or subregions, 'detailed' with configuration of system classes and subregions as derived before, 'det 1 cls' same configuration but considering one system class only.

A quantification of the upscaling rmse in dependency on the month of the year 2013 is displayed in the right panel of fig. 6.12. In this figure, the 'detailed' upscaling configuration based on different system classes and regions is compared to the 'simple' approach without any distinction of system classes or regions and to the approach considering all regional clusters but one system class only. Apparently, the upscaling using system classes and regional clustering, as derived above, shows a lower overall rmse than the simple approach, but comparable results to the approach only distinguishing regional clusters. For the months March and April, even the simple upscaling approach shows lower rmse than the more detailed approaches. Analysis show, that this emerges from one single control area and is an effect of reducing the amount of sites per class and region by clustering with the detailed upscaling approach: In this specific control area, some subregions are poorly covered with representative sites.

The average rmse and bias of upscaled measured and predicted PV power are displayed in fig 6.13 and table 6.1 for each control area and for Germany. Here, all months January to December 2013 are included, and the upscaling rmse based on measured PV power and CMV 2h forecasts are compared. For the single control areas, the rmse is between 2% and 3% of installed capacity for measured PV power, and between 3.5% and 4.1% for CMV 2 hour forecasts. For overall Germany, the upscaling rmse is significantly smaller than for the single control areas (1.8% and 2.8% for measured and predicted PV power respectively). The bias error is between −0.35% and +1.6% for measured PV, and between −0.9% and +1.6% for predicted PV power, depending on the control area. Relative differences between the control areas are larger for upscaling based on measured PV without the additional forecast error.

Evaluations indicate a good performance of the detailed upscaling approach compared to RES feed-in time series. Some systematic deviations depending on the control area evaluated appeared, potentially a consequence of not well matched information with respect to the installed capacity per control area or subregion or the information on the distribution of the PV systems.

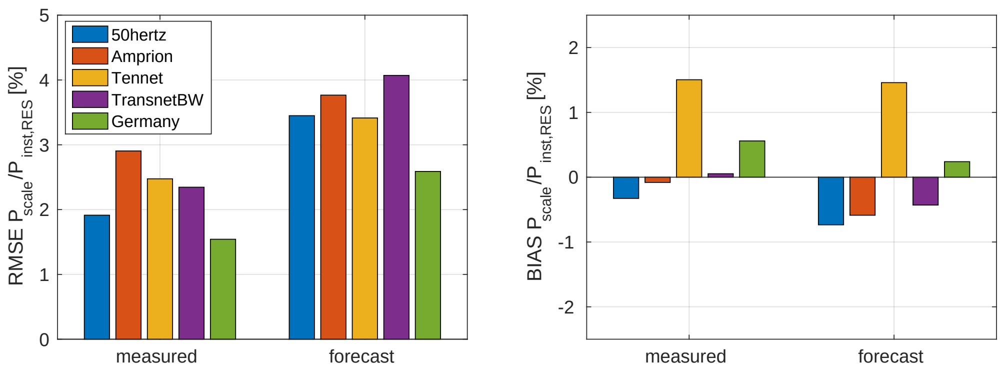

Figure 6.13.: Rmse (left) and bias (right) for the upscaling rmse for the different control areas and for Germany, based on measured PV power (left columns) and 2 hour CMV forecasts (right column) for the 'detailed' upscaling approach. Dataset: Jan to Dec 2013, upscaling based on 921 sites, 15 min. resolution, no restrictions with respect to solar zenith angles.

Table 6.1.: Mean PV power feed-in and upscaling rmse for the control areas and Germany with the detailed upscaling with respect to the RES feed-in time series as reference. Dataset: Jan–Dec 2013, 15 min resolution, no restrictions with respect to solar zenith angles.

Control Area	P_{mean} P/P_{inst}	P_{inst} [GW]	rmse meas. P/P_{inst}	bias meas. P/P_{inst}	rmse forec. P/P_{inst}	bias forec. P/P_{inst}
50 hertz	20.4 %	6.72	1.91 %	-0.33 %	3.45 %	-0.74 %
amprion	20.1 %	7.67	2.01 %	-0.08 %	3.77 %	-0.59 %
Tennet TSO	18.3 %	13.90	2.48 %	+1.50 %	3.41 %	+1.46 %
TransnetBW	21.4 %	4.73	2.34 %	+0.05 %	4.07 %	-0.43 %
Germany	19.0 %	33.03	1.54 %	+0.56 %	2.56 %	+0.24 %

6.5. Evaluation of regional PV power forecasts

In this section, the combination of PV power forecasts as developed in chapter 5 is applied to regional forecasts, derived with the upscaling algorithm as developed in section 6.4. In contrast to the section before, the forecast accuracy here is rated against the projections of the regional power feed-in based on measured PV power, and not to any external reference. To derive combined regional PV power forecasts, as a first step, the upscaling algorithm is applied to the PV power measurements on the one hand and individually on CMV, NWP and persistence forecasts on the other. The combination approach applied uses the configuration for regional forecasting according to section 5.2.2; the representative dataset here consists of all 921 sites in the *meteocontrol* dataset 'C'.

The rmse for the 2 hour forecast horizon of the combined forecasts for each control area and Germany is displayed in table 6.2. Is is given normalized to the installed capacity per region and in absolute values. For comparison, the average PV power feed-in for each control area is displayed. This average feed-in is in the range of 25.0% to 26.8% of the respective installed capacity per control area for the annual average in 2013. The regional forecast rmse is between 2.17% for Germany and 4.06% for the smallest control area of TransnetBW. The normalized rmse gets smaller as the control area gets larger with respect to the installed capacity. This is due to lower forecast rmse for larger areas averaged and a higher benefit for the combined approach with increasing region size, as stated in section 5.3. However, in absolute values, the forecast rmse increases with the absolute installed capacity per control area.

The 5th and 95th percentile in table 6.2 of the upscaled regional 2h combined forecasts indicates the magnitude of largest errors of the forecast approach shown. It enables an estimation on the balancing energy needed in events of large forecast errors. Here, values between 425 MW and 1.5 GW are found, depending on the magnitude of errors and the installed capacity per control area. It is differentiated between positive and negative errors, as over- or underestimations of the power affects the usage of control energy in different ways and leads to different costs.

The Improvement Score relating the rmse of the combined forecasts to the rmse of the NWP only-based forecasts is displayed in table 6.3. By this, the reduction of forecast rmse achieved by i) CMV forecasts, ii) online measured PV power, and iii) combining

Table 6.2.: Accuracy of regional combined 2 hour forecasts for the control areas and Germany, given in rmse normalized to the installed capacity and in absolute values. Dataset: Jan–Dec 2013, upscaling based on 921 sites, 15 min resolution, no restrictions to solar zenith angles.

Control Area	P_{mean}	P_{inst}	rmse 2h forecasts		percentiles [MW]	
	P/P_{inst}	[GW]	P/P_{inst}	[MW]	5th	95th
50 hertz	25.2 %	6.72	3.23 %	217	-450	437
amprion	25.5 %	7.67	3.13 %	240	-476	528
Tennet TSO	25.3 %	13.90	2.61 %	363	-747	796
TransnetBW	26.8 %	4.73	4.06 %	192	-425	447
Germany	25.0 %	33.03	2.17 %	717	-1507	1582

Table 6.3.: Impact of the forecast combination introduced in this thesis on the rmse, compared to the NWP-only forecasts. Evaluated are regional forecasts with the upscaling algorithm applied for each individual control area and Germany, for forecast horizons of 2 hours ahead. The forecast accuracy when using the combined forecasts with persistence, CMV and NWP forecasts is compared to the combined forecast accuracy using CMV and NWP forecasts only, or the persistence and NWP forecasts only. Dataset: Jan–Dec 2013, upscaling based on 921 sites, 15 min resolution.

Control Area	NWP	combined		(CMV,NWP)		(pers,NWP)	
	rmse	rmse	IS [%]	rmse	IS [%]	rmse	IS [%]
50 hertz	404 MW	217 MW	44.0	248 MW	38.5	246 MW	36.5
amprion	422 MW	240 MW	40.8	262 MW	38.1	281 MW	30.6
Tennet TSO	710 MW	363 MW	46.7	416 MW	41.4	457 MW	32.8
TransnetBW	317 MW	192 MW	36.7	209 MW	34.0	222 MW	26.7
Germany	1.58 GW	717 MW	52.6	866 MW	45.1	888 MW	41.3

these forecast approaches is quantified. The contributions of each individual method within the combined forecast approach on the overall accuracy of the regional combined forecasts are additionally displayed; for these figures, the combined forecasts are applied with using only two individual forecast approaches, as it was also shown in section 5.5.

The CMV forecast approach contributes a 34% to 45% improvement rated against the NWP forecasts, the introduction of online measured PV power an improvement between 26% and 41%. Combining all three forecast approaches, the IS is between 36% for the control area of TransnetBW and 52.6% for the area of Germany: Thus, an overall reduction of forecast rmse to less than half of the NWP-based forecast rmse is achieved by the methods introduced in this thesis.

6.6. Conclusion

In this chapter, an upscaling algorithm is introduced to derive regional projections from single site measured or predicted PV power. Lacking a valid external reference, the model development of the algorithm is done for a closed environment based on measured PV power from the dataset used throughout the thesis. The differentiation of system classes according to the installed capacity of the PV power plants and the clustering of regions to smaller subsystems is beneficial for the upscaling accuracy. In general, with the amount of sites in the representative dataset the upscaling error decreases, up to a certain threshold for the amount of representative sites used. The actual configuration of the classification depends on the dataset that has to be modeled and whether it is applied to measured or predicted PV power.

With the findings displayed for the model development dataset, a configuration of the upscaling approach applicable to the RES dataset is found. Evaluations against the published power feed-in according to the RES act are performed. The upscaling of measured PV power leads to a rmse of the power feed-in estimations between 1.7% and 3%, normalized to the installed capacity, depending on the control area evaluated. This error can arise from several sources in the upscaling process, from the upscaling process itself on the one hand, and from insufficient quality of datasets included on the other. Information like the regional distribution of PV sites or overall installed capacities in the control areas are of fundamental importance.

This chapter concludes with an overview on the achieved reduction of forecast rmse for regional forecasts by methods introduced in this thesis. Here the impact of using satellite- and measurement-based forecasts compared to NWP-based forecasts only is evaluated, based on predicted and measured PV feed-in for the different control areas. A reduction of the rmse of up to 53% for the forecast horizon of two hours ahead is observed, depending on the control area evaluated.

7. Conclusion and Outlook

Operation strategies of energy supply systems with a high share of photovoltaic (PV) power require precise forecasts of the PV power feed-in. The research done in context of this thesis contributes to an improvement of PV power forecasts for intraday market applications. Forecasts developed result in a reduction of regional PV power forecasts' root mean square error (rmse) of over 50% for 2 hours ahead in comparison to numerical weather prediction models. By analyzing all parts of the PV power prediction system, a detailed understanding of the processing steps is gained with respect to models involved and data required. Throughout the research presented, model development and analysis is done using 15 minute resolved measured PV power data for more than 1000 sites in Germany. These are complemented by meteorological measurements of irradiance and temperature. PV power forecasts investigated are based on solar irradiance forecasts, an explicit physical irradiance-to-power conversion model and an upscaling approach to derive regional projections based on single site forecasts.

It is shown that short-term irradiance forecasts of a few hours ahead are significantly improved by a satellite-based approach using cloud motion vectors (CMV), Kühnert et al. (2013) [60]. The CMV method leads to a reduction of forecast rmse up to four hours ahead, compared to established numerical weather predictions (NWP). In general, regionally averaged forecasts show significant lower rmse than forecasts for single sites. Evaluations of irradiance forecasts are provided with respect to single sites and with focus on all sites averages, dependent on different parameters such as the time of day or seasonal changes. Limitations of the CMV method are observed for solar zenith angles $> 80°$ at forecast base time as satellite images in the visible spectral range are used. An extension of the CMV algorithm to infrared satellite images is evaluated in context of a joint research paper, Hammer et al. (2015) [66]: Forecast quality and availability in the morning hours is improved.

The impact of PV power modeling on forecast accuracy is focused on in a next step. A detailed investigation of the irradiance-to-power conversion by explicit physical modeling is performed in Kühnert et al. (2015) [65] with respect to an optimization of models applied and to an assessment of the impact of different input data quality and models' configuration: PV power forecast accuracy is found to be rather insensitive to the use of different plane-of-array irradiance conversion models. Best performance of PV power simulation is found when using a parametric model adapted to historically measured PV power and utilizing NWP temperature forecasts. However, statistical training by a simple linear regression approach using measured PV power of a number of previous days can mitigate the impact on PV power forecast accuracy of the PV efficiency model's configuration and of temperature information utilized. PV power forecasts evaluated show similar characteristics to irradiance forecasts with respect to the performance of the CMV approach compared to NWP forecasts and with respect to spatially averaged compared to single-site forecasts.

To derive forecast of power feed-in of all PV sites in an area, an upscaling approach based on representative sites is developed and applied in this thesis. Lacking a valid external reference of regional PV power feed-in, a closed environment for model development is created. For an optimized projection of PV power feed-in, information on tilt and azimuth angles of all PV sites contributing are implicitly deduced from available datasets. Regional clustering of PV sites for regional forecasting has to be performed with respect to the availability of representative sites, size of the clustered regions and regional distribution of overall PV power capacities. To do so, information on the energy systems' configuration like distribution of PV sites and installed capacities is essential.

It is demonstrated in this thesis that the combination of PV power forecasts from NWP or satellite data with online measured PV power shows high potential for forecast improvement. A method for forecast combination is developed based on a linear regression approach trained with measured PV power from the previous days. This approach contributes to a significant improvement of regional PV power forecasts and shows equal or better performance compared to advanced pure statistical approaches, as shown in Wolff et al. (2015) [86]. In general, the rmse of PV power forecasts strongly decreases when PV power measurements are integrated directly or implicitly into forecasting. This is shown by the reduction of systematic deviations using historical data and by improvement of short-term forecast quality by the online integration of measured PV power.

Several topics for future research emerged from analysis in the context of this thesis: Special weather conditions such as e.g. persistent fog are not well matched by the irradiance forecasting approaches utilized. Here, potential is seen in the application of satellite images from the infrared or other channels and by an enhanced integration of PV power metering data. The presented satellite-based irradiance forecasting approach can further be improved by the use of auxiliary data e.g. from NWP models or other satellite-derived products. Irradiance forecasts in general can be enhanced by the application of statistical methods as was for example shown for numerical weather predictions in Brause (2015) [104]. Explicit physical PV power simulation used in this thesis can be consistently replaced with pure statistical approaches or by the combination of physical and statistical methods, see e.g. Wolff et al. (2015) [86]. Snow-covered PV modules add further complexity and are subject to ongoing research: A correct estimation of snow covering and melting is essential in winter months and strongly depends on the PV site characteristics.

The assessment of uncertainty information for PV power forecasts is relevant to forecast applicability: The risk of decisions based on forecasts can be assessed when information on the expected uncertainty is delivered with the forecast. Here, several strategies exist, like the use of ensemble forecasts from NWP providers or the application of analogue ensembles based on statistics of historical forecasts. Probabilistic forecasts for the application in PV power forecasting were initially analyzed in Przybilla (2015) [105]: From this, the need of calibration of these ensemble forecasts with measurement data arose, which will be focused on in following studies. The application of analogue ensembles for wind power forecasts was subject to recent research by Junk et al. (2014) [54], a transfer of methods developed to PV power forecasts is promising.

In general, all approaches presented rely on the availability of accurate information describing the energy system: Here, further development by improving e.g. system metering or data assessment of the energy grid characteristics can be beneficial and should be considered in future research. With the transition of the energy market and energy grid operations, e.g. by a shift towards a high share of own consumption from industries or private households and with the integration of decentralized storage capacities, fields of application of and requirements towards PV power forecasts changes. From this, single site forecasts for an optimization of demand-side-management systems or loading profiles of battery systems move into focus. Introducing these technologies changes the characteristics of power feed-in and load profiles: Own-consumption reduces and changes characteristics of PV power feed-in into the grid, storage capacities can contribute to reduce feed-in variability. For regional forecasts for energy market application, an adaption of existing forecasting methods may be a consequence. PV power forecasting will remain essential for grid operation strategies and gain relevance for future application and for managing the feed-in of extending PV power generation capacities.

Bibliography

[1] H. Wirth and K. Schneider. Recent facts about photovoltaics in Germany. Tech. rep. Freiburg, Germany: Fraunhofer ISE, 2015.

[2] S. Lüers and A. Wallasch. Status des Windenergieausbaus an Land in Deutschland. Tech. rep. Deutsche Windguard, 2015.

[3] J. Müller, M. Hildmann, A. Ulbig, and G. Andersson. Grid integration costs of fluctuating renewable energy sources. In: IEEE Conference on Technologies for Sustainability (SusTech). 2014, 15–21.

[4] L. Hirth and I. Ziegenhagen. Control power and variable renewables: a glimpse at german data. In: FEEM Working Paper 46 (2013).

[5] D. Ernst. Herausforderungen bei der Systemintegration von erneuerbaren Energien aus Sicht eines Übertragungsnetzbetreibers. In: Proc. 29. Symposium Photovoltaische Solarenergie. Bad Staffelstein, Mar. 2014.

[6] Monitoringbericht 2014 der Bundesnetzagentur. Tech. rep. 2014. URL: http://www.bundesnetzagentur.de/ (visited on 03/19/2015).

[7] B. Ernst, B. Oakleaf, M. Ahlstrom, M. Lange, C. Moehrlen, B. Lange, U. Focken, and K. Rohrig. Predicting the Wind. In: IEEE Power and Energy Magazine 5.6 (2007), 78–89. DOI: 10.1109/MPE.2007.906306.

[8] S. Pelland, J. Remund, J. Kleissl, T. Oozeki, and K. De Brabandere. Photovoltaic and Solar Forecasting: State of the Art. IEA PVPS Task 14, Subtask 3.1. 2013.

[9] R. Perez, E. Lorenz, S. Pelland, M. Beauharnois, G. van Knowe, K. Hemker Jr, D. Heinemann, J. Remund, S. C. Müller, W. Traunmüller, G. Steinmauer, D. Pozo, J. Ruiz-Arias, V. Lara-Fanego, L. Ramirez-Santigosa, M. Gaston-Romero, and L. Pomares. Comparison of numerical weather prediction solar irradiance forecasts in the US, Canada and Europe. In: Solar Energy 94 (2013), 305–326. DOI: 10.1016/j.solener.2013.05.005.

[10] R. Perez, S. Kivalov, J. Schlemmer, K. Hemker, D. Renné, and T. Hoff. Validation of short and medium term operational solar radiation forecasts in the US. In: Solar Energy 84.12 (2010), 2161–2172. DOI: 10.1016/J.SOLENER.2010.08.014.

[11] S. Müller and J. Remund. Satellite based shortest term solar energy forecast system for entire europe for the next hours. In: Proc. of 30. EU PVSEC. 2014.

[12] E. Lorenz, D. Heinemann, and A. Hammer. Short-term forecasting of solar radiation based on satellite data. In: Proceedings of EuroSun 2004, Freiburg, Germany. 2004, 841–848.

[13] C. W. Chow, B. Urquhart, M. Lave, A. Dominguez, J. Kleissl, J. Shields, and B. Washom. Intra-hour forecasting with a total sky imager at the UC San Diego solar energy testbed. In: Solar Energy 85.11 (2011), 2881–2893. DOI: 10.1016/j.solener.2011.08.025.

[14] E. Lorenz and D. Heinemann. Prediction of Solar Irradiance and Photovoltaic Power. In: Comprehensive Renewable Energy. Vol. 1. Elsevier Ltd., 2012, 239–292.

[15] P. Ineichen. Comparison and validation of three global-to-beam irradiance models against ground measurements. In: Solar Energy 82.6 (2008), 501–512. DOI: 10.1016/j.solener.2007.12.006.

[16] S. Pelland, G. Galanis, and G. Kallos. Solar and photovoltaic forecasting through post-processing of the Global Environmental Multiscale numerical weather prediction model: Solar and photovoltaic forecasting. In: Progress in Photovoltaics: Research and Applications 21.3 (2011), 284–296. DOI: 10.1002/pip.1180.

[17] P. Bacher, H. Madsen, and H. Nielsen. Online short-term solar power forecasting. In: Solar Energy 83.10 (2009), 1772–1783. DOI: 10.1016/j.solener.2009.05.016.

[18] C. Monteiro, T. Santos, L. Fernandez-Jimenez, I. Ramirez-Rosado, and M. Terreros-Olarte. Short-Term Power Forecasting Model for Photovoltaic Plants Based on Historical Similarity. en. In: Energies 6.5 (2013), 2624–2643. DOI: 10.3390/en6052624.

[19] N. Engerer and F. Mills. KPV: A Clear-Sky Index for Photovoltaics. In: Solar Energy 105 (2014), 679–693. DOI: 10.1016/j.solener.2014.04.019.

[20] E. Lorenz, T. Scheidsteger, J. Hurka, D. Heinemann, and C. Kurz. Regional PV power prediction for improved grid integration. In: Progress in Photovoltaics: Research and Applications 19 (2011), 757–771. DOI: 10.1002/pip.

[21] Meteocontrol GmbH. URL: http://www.meteocontrol.com/.

[22] E. Lorenz, D. Heinemann, and C. Kurz. Local and regional photovoltaic power prediction for large scale grid integration: Assessment of a new algorithm for snow detection. In: Progress in Photovoltaics: Research and Applications (2011). DOI: 10.1002/pip.1224.

[23] E. Lorenz, J. Hurka, D. Heinemann, and H. Beyer. Irradiance Forecasting for the Power Prediction of Grid-Connected Photovoltaic Systems. In: IEEE Journal of Selected Topics in Applied Earth Observations and Remote Sensing 2.1 (2009), 2–10. DOI: 10.1109/JSTARS.2009.2020300.

[24] C. Weber. Adequate intraday market design to enable the integration of wind energy into the European power systems. In: Energy Policy 38.7 (July 2010), 3155–3163. DOI: 10.1016/j.enpol.2009.07.040.

[25] Federal ministry for econonmic affairs and energy (BMWi). An electricity market for Germany's Energy Transition (Green Paper). Tech. rep. 2014.

[26] European Energy Exchange Leipzig. URL: https://www.eex.com/ (visited on 06/22/2015).

[27] European Power Exchange Paris. URL: http://www.epexspot.com/en/ (visited on 06/22/2015).

[28] M. Nicolosi. Leitstudie Strommarkt 2015. Tech. rep. 2015.

[29] S. von Roon. Auswirkungen von Prognosefehlern auf die Vermarktung von Windstrom. PhD thesis. München: Forschungsstelle für Energiewirtschaft eV (FfE), 2010.

[30] F. Sensfuß, M. Ragwitz, and M. Genoese. The merit-order effect: a detailed analysis of the price effect of renewable electricity generation on spot market prices in Germany. Tech. rep. 7. Karlsruhe: Fraunhofer ISI, 2007.

[31] M. Fürsch, R. Malischek, and D. Lindenberger. Der Merit-Order-Effekt der erneuerbaren Energien - Analyse der kurzen und langen Frist. In: EWI Working Papers 14 (2012).

[32] O. Feix, R. Obermann, M. Hermann, and S. Zeltner. Netzentwicklungsplan Strom 2012, Entwurf der Übertragungsnetzbetreiber. Tech. rep. 2012.

[33] RES act. Act on the Development of Renewable Energy Sources. 2014.

[34] A. Klemm. Der EEG-Belastungsausgleich. Tech. rep. Köln: Forum Contracting e.V., 2010.

[35] Bundesnetzagentur. Evaluierungsbericht zur Ausgleichsmechanismusverordnung. Tech. rep. Bonn, 2012.

[36] E. Hauser and M. Luxenburger. Systemintegration von Erneuerbaren Energien durch Nutzung von Marktmechanismen im Stromsektor. Tech. rep. Saarbrücken, 2011.

[37] next-kraftwerke.de. Direktvermarktung. URL: https://www.next-kraftwerke.de/wissen/direktvermarktung (visited on 06/22/2015).

[38] L. Hirth and I. Ziegenhagen. Wind, Sonne und Regelleistung. In: Energiewirtschaftliche Tagesfragen 63.10 (2013).

[39] E. Garnier and R. Madlener. Balancing forecast errors in continuous-trade intraday markets. In: Energy Systems (2014), 1–28.

[40] S. von Roon. Empirische Analyse über die Kosten des Ausgleichs von Prognosefehlern der Wind-und PV-Stromerzeugung. In: Internationale Energiewirtschaftstagung an der TU Wien (2011), 16–18.

[41] C. Möller, S. Rachev, and F. Fabozzi. Balancing energy strategies in electricity portfolio management. en. In: Energy Economics 33.1 (Jan. 2011), 2–11. DOI: 10.1016/j.eneco.2010.04.004.

[42] Amprion TSO. Procurement of control energy. 2015. URL: http://www.amprion.net/en/control-energy (visited on 06/22/2015).

[43] M. Sieg. Speicher regeln Netze. In: PV magazine (2014). URL: http://www.pv-magazine.de/.

[44] regelleistung.net. Common tendering for primary control reserve. URL: https://www.regelleistung.net/ (visited on 06/22/2015).

[45] regelleistung.net. Tender overview. URL: https://www.regelleistung.net/ip/action/ausschreibung/public (visited on 06/22/2015).

[46] Germanenergyblog.de. Today’s Solar Eclipse Secondary Control Reserve Power Tender. 2015. URL: http://www.germanenergyblog.de/ (visited on 03/18/2015).

[47] L. Hirth, F. Uekerdt, and O. Edenhoffer. Integration Costs Revisited. In: Renewable Energy 74 (2015).

[48] F. Borggrefe and C. Neuhoff. Balancing and Intraday Market Design: Options for Wind Integration. In: Discussion Papers Deutsches Institut für Wirtschaftsforschung (2011).

[49] Bundesnetzagentur. Positionspapier zur verbesserten Prognose und Bilanzierung von Solarstromeinspeisungen. Tech. rep. 2010.

[50] D. Lew, M. Milligan, G. Jordan, and R. Piwko. The value of wind power forecasting. In: 91st AMS Annual Meeting, 2nd Conference on Weather, Climate, and the New Energy Economy Proceedings, Washington, DC. 2011.

[51] G. Swinand and A. O'Mahoney. Estimating the impact of wind generation and wind forecast errors on energy prices and costs in Ireland. In: Renewable Energy 75 (2015), 468–473.

[52] Zeitung für kommunale Wirtschaft. Prognosefehler von 8800 MW. In: Zeitung für kommunale Wirtschaft (2013). URL: https://www.zfk.de/strom/artikel/prognosefehler-von-8800-mw.html (visited on 07/16/2013).

[53] P. Hirschberg, E. Abrams, A. Bleistein, W. Bua, L. Monache, T. Dulong, J. Gaynor, B. Glahn, T. Hamill, J. Hansen, et al. A weather and climate enterprise strategic implementation plan for generating and communicating forecast uncertainty information. In: Bulletin of the American Meteorological Society 92.12 (2011), 1651–1666.

[54] C. Junk, J. Monache, S. Alessandrini, G. Cervone, and L. von Bremen. Predictor-weighting strategies for probabilistic wind power forecasting with an analog ensemble. en. In: Meteorologische Zeitschrift (2014). DOI: 10.1127/metz/2015/0659.

[55] tennet TSO. Einspeisung und Anlagenregister. URL: http://www.tennet.eu/de/kunden/eegkwkg/erneuerbare-energien-gesetz/eeg-daten-nach-52/einspeisung-und-anlagenregister.html (visited on 07/18/2015).

[56] www.amprion.net. Aktuelle EEG-Anlagendaten. URL: http://www.amprion.net/eeg-anlagenstammdaten-aktuell (visited on 07/18/2015).

[57] 50Hertz Transmission GmbH. EEG-Anlagenstammdaten. URL: http://www.50hertz.com/de/EEG/Veroeffentlichung-EEG-Daten/EEG-Anlagenstammdaten (visited on 07/18/2015).

[58] TransnetBW. EEG-Anlagendaten. URL: https://www.transnetbw.de/de/eeg-kwk-g/eeg/eeg-anlagendaten (visited on 07/18/2015).

[59] EEX Transparency Platform. URL: http://www.eex-transparency.com/ (visited on 06/22/2015).

[60] J. Kühnert, E. Lorenz, and D. Heinemann. Satellite-Based Irradiance and Power Forecasting for the German Energy Market. In: Elsevier Book on Solar Energy Forecasting and Resource Assessment. Boston: Academic Press, 2013, 267–297.

[61] E. Lorenz, J. Kühnert, and D. Heinemann. Short Term Forecasting of Solar Irradiance by Combining Satellite Data and Numerical Weather Predictions. In: Proceedings of 27th EUPVSEC. Frankfurt, Germany., 2012.

[62] H. Beyer, J. Martinez, M. Suri, J. Torres, E. Lorenz, S. Müller, C. Hoyer-Klick, and P. Ineichen. Report on Benchmarking of Radiation Products. Tech. rep. 2009.

[63] D. Wilks. Statistical Methods in the Atmospheric Sciences. Elsevier Ltd., 2006.

[64] J. Zhang, B. Hodge, A. Florita, S. Lu, H. Hamann, and V. Banunarayanan. Metrics for evaluating the accuracy of solar power forecasting. In: 3rd International workshop on integration of solar power into power systems, London, England. 2013.

[65] J. Kühnert, E. Lorenz, and D. Heinemann. Impact of photovoltaic power simulation on regional PV power forecast. In: Progress in Photovoltaics: Research and Applications (submitted) (2015).

[66] A. Hammer, J. Kühnert, K. Weinreich, and E. Lorenz. Short-Term Forecasting of Surface Solar Irradiance Based on Meteosat-SEVIRI Data Using a Nighttime Cloud Index. In: Remote Sensing 7.7 (2015), 9070–9090. DOI: 10.3390/rs70709070.

[67] K. Liou. An Introduction to Atmospheric Radiation. Academic Press, 1980.

[68] M. Iqbal. An Introduction to Solar Radiation. Academic Press, 1983.

[69] D. Dumortier. Modelling global and diffuse horizontal irradiances under cloudless skies with different turbidities. Tech. rep. JOU2-CT92-0144. Vaulx-en-Velin, France, 1995.

[70] R. Mueller, K. Dagestad, P. Ineichen, S. Cros, D. Dumortier, R. Kuhlemann, J. Olseth, G. Piernavieja, C. Reise, L. Wald, and D. Heinemann. Rethinking satellite based solar irradiance modelling - The SOLIS clear-sky module -. In: Remote Sensing of Environment 91.2 (2004), 160–174.

[71] M. Fontoynont, D. Dumortier, D. Heinemann, A. Hammer, J. Olseth, A. Skarveit, P. Ineichen, C. Reise, J. Page, L. Roche, et al. Satellight: a WWW server which provides high quality daylight and solar radiation data for Western and Central Europe. In: 9th Conference on Satellite Meteorology and Oceanography. American Meteorological Society Ed., Boston, Massachusetts, USA, 1998, 434–437.

[72] J. Remund. Aerosol optical depth and Linke turbidity climatology. Tech. rep. 2009.

[73] B. Bourges. Yearly variations of the Linke turbidity factor. In: Dordrecht: Kluwer Academic Publishing, 1992, 61–64.

[74] J. Schmetz, P. Pili, S. Tjemkes, D. Just, J. Kerkmann, S. Rota, and A. Ratier. An Introduction to Meteosat Second Generation (MSG). In: American Meteorological Society (2002).

[75] EUMETSAT Webpage. URL: http://www.eumetsat.int/ (visited on 09/14/2015).

[76] D. Cano, J. Monget, M. Albuisson, H. Guillard, N. Regas, and L. Wald. A method for the determination of the global solar radiation from meteorological satellite data. In: Solar Energy 37.1 (1986), 31–39.

[77] H. Beyer, C. Costanzo, and D. Heinemann. Modifications of the heliosat procedure for irradiance estimates from satellite images. In: Solar Energy 56.3 (1996), 207–212. DOI: 10.1016/0038-092X(95)00092-6.

[78] A. Hammer, D. Heinemann, C. Hoyer, R. Kuhlemann, E. Lorenz, R. Müller, and H. Beyer. Solar energy assessment using remote sensing technologies. In: Remote Sensing of Environment 86.3 (2003), 423–432. DOI: 10.1016/S0034-4257(03)00083-X.

[79] A. Hammer, E. Lorenz, and S. Petrak. Fernerkundung der Solarstrahlung für Anwendungen in der Energietechnik. In: Proc. of DACH Conference. Hamburg, Germany, 2007.

[80] S. Heinicke. Schneeerkennung auf Basis von multispektralen und multitemporalen Metesat-8-Informationen - Einbettung in das bestehende Verfahren der Heliosat-Methode. diploma thesis. University of Oldenburg, 2006.

[81] H. Beyer, C. Costanzo, D. Heinemann, and C. Reise. Short range forecast of PV energy production using satellite image analysis. In: Proceedings of the 12th European Photovoltaic Solar Energy Conference and Exhibition. Amsterdam, The Netherlands, 1994, 1718–1721.

[82] A. Hammer, D. Heinemann, and E. Lorenz. Short-term forecasting of solar radiation: a statistical approach using satellite data. In: Solar Energy 67.1992 (1999), 139–150. DOI: 10.1016/S0038-092X(00)00038-4.

[83] Deutscher Wetterdienst, DWD. URL: http://www.dwd.de/.

[84] G. V. Rozenberg. Twilight A Study in Atmospheric Optics. New York, USA: Plenum Press., 1966.

[85] E. Lorenz. Qualitätskontrolle von PV Leistungsmesswerten. internal report. 2012.

[86] B. Wolff, J. Kühnert, E. Lorenz, O. Kramer, and D. Heinemann. Comparing Support Vector Regression for PV power forecasting to a physical modeling approach implementing measurement, numerical weather prediction, and cloud motion data. In: Solar Energy (submitted) (2015).

[87] A. Skartveit and J. Olseth. A Model for the Diffuse Fraction of Hourly Global Radiation. In: Solar Energy 38 (1987), 271–274. DOI: 10.1016/0038-092X(87)90049-1.

[88] A. Skartveit, J. Olseth, and M. Tuft. An hourly diffuse fraction model with correction for variability and surface albedo. In: Solar Energy 63 (1998), 173–183. DOI: 10.1016/S0038-092X(98)00067-X.

[89] R. Perez, P. Ineichen, E. Maxwell, R. Seals, and A. Zelenka. Dynamic Global-to-direct irradiance conversion models. In: ASHRAE Transactions 98.1 (1992), 354–369.

[90] R. Perez, P. Ineichen, K. Moore, M. Kmiecik, C. Chain, R. George, and F. Vignola. A new operational model for satellite-derived irradiances: description and validation. In: Solar Energy 73 (2002), 307–317.

[91] T. Klucher. Evaluation of models to predict insolation on tilted surfaces. In: Solar Energy 23 (1979), 111–114. DOI: 10.1016/0038-092X(79)90110-5.

[92] R. Perez, R. Seals, P. Ineichen, R. Stewart, and D. Menicucci. A new simplified version of the perez diffuse irradiance model for tilted surfaces. In: Solar Energy 39.3 (1987), 221–231.

[93] B. Liu and R. Jordan. The interrelationship and characteristic distribution of direct, diffuse and total solar radiation. In: Solar Energy 4.3 (1960), 1–19.

[94] PVPerformance Modlling Collaborative. URL: https://pvpmc.sandia.gov/.

[95] H. Beyer, J. Betcke, A. Drews, D. Heinemann, E. Lorenz, G. Heilscher, and S. Bofinger. Identification of a general model for the mpp performance of pv-modules for the application in a procedure for the performance check of grid connected systems. In: Proceedings of 19th EUPVSEC. 2004, 3073–3076.

[96] H. Schmidt and D. Sauer. Wechselrichter - Wirkungsgrade, Praxisgerechte Modellierung und Abschätzung. In: Sonnenenergie 21 (1996), 43–47.

[97] G. Müller-Westermeier, A. Walter, and E. Dittmann. Klimaatlas Bundesrepublik Deutschland, Teil 1-4. Tech. rep. Offenbach am Main, 2005.

[98] U. Maier and G. Müller-Westermeier. Berichte des Deutschen Wetterdienstes 235. Tech. rep. Offenbach am Main, 2010.

[99] P. Mathiesen. Advanced Numerical Weather Prediction Techniques for Solar Irradiance Forecasting: Statistical, Data-Assimilation, and Ensemble Forecasting. PhD thesis. UC San Diego, 2013.

[100] C. Marty and R. Philipona. The clear-sky index to separate clear-sky from cloudy-sky situations in climate research. In: Geophysical Research Letters 27.17 (2000), 2649–2652.

[101] J. Kühnert, E. Lorenz, J. Betcke, A. Hammer, and D. Heinemann. Regionale PV-Leistungsvorhersagen für den Kurzzeit-Bereich auf Basis von Satellitendaten, numerischen Wetterprognosen und PV-Leistungsmessungen. In: Tagungsband des 29. Symposiums Photovoltaische Solarenergie. Bad Staffelstein, 2014.

[102] Bundesnetzagentur. Meldung von Photovoltaikanlagen an die Bundesnetzagentur. URL: http://www.bundesnetzagentur.de/cln_1412/DE/Sachgebiete/ElektrizitaetundGas/Unternehmen_Institutionen/ErneuerbareEnergien/Photovoltaik/Photovoltaik_node.html (visited on 07/18/2015).

[103] http://www.netztransparenz.de. Veröffentlichungen zur Marktprämie nach § 33g in Verbindung mit Anlage 4 EEG. (Visited on 09/14/2015).

[104] C. Brause. Postprocessing von numerischen Solarleistungsprognosen mit Hilfe von Machine-Learning-Verfahren. Master thesis. University of Oldenburg, 2015.

[105] K. Przybilla. Analyse von ECMWF Ensemble-Vorhersagen. Master thesis. University of Oldenburg, 2014.

[106] G. Lohmann, J. Kühnert, E. Lorenz, A. Hammer, and D. Heinemann. Fluctuations in Large-scale Photovoltaic and Wind Power Feed-in. In: Proceedings of the 4th International Workshop on Integration of Solar Power into Power Systems. Berlin, Germany, 2014.

A. Additional figures

A.1. Ambient temperature

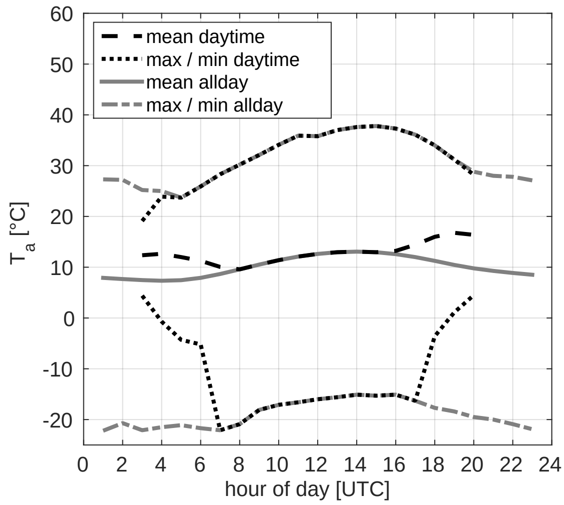

Figure A.1.: Comparison of mean, maximum and minimum ambient temperature as function of hour of day for daytime only and all-day temperatures. Dataset: Jan–Dec 2012, 35 sites, 1 hour resolution.

A.2. Diurnal variation of PV power clear sky index

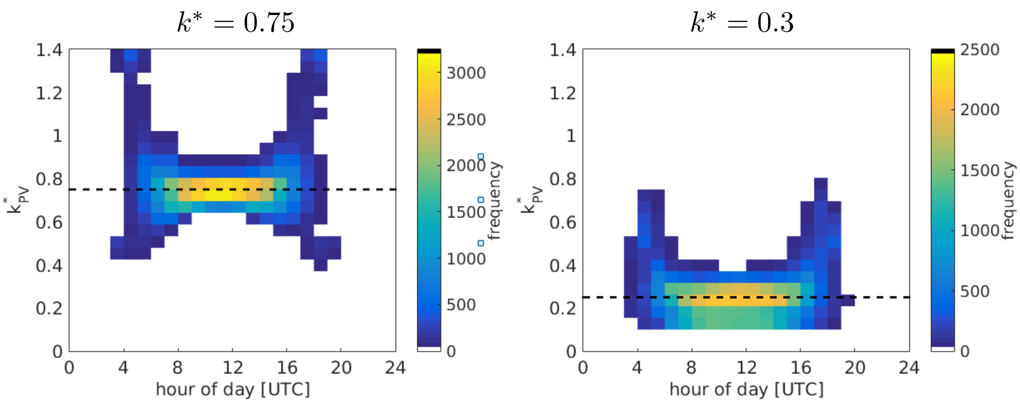

Figure A.2.: Modelled k^*_{PV} for fixed irradiance clear sky index k^* values in dependence on the hour (UTC) for the data set for 12 days a year (each 21st) and for 150 sites with $\phi < 30°$ and variating tilt angles β.

A.3. Validation of persistence approaches

Table A.1.: Variation of the persistence approach within the combined forecast, with different persistence configurations and variation of the ambient temperature input.

persistence for single sites' and averages with/without linear regression (fig. A.3)	
single	persistence for single sites
single + lr	persistence for single sites with linear regression ('lr') applied
averaged(single)	spatially averaged single sites' persistence
averaged(single+lr)	spatially averaged single sites' persistence with ('lr') applied
averaged(single)+lr	spatially averaged single sites' persistence with ('lr') applied afterwards
input variation for persistence forecast (fig. A.4 left)	
persistence	according to section 5.1.2, with k^*_{PV} from last measurement
1 hour average	with k^*_{PV} averaged over preceding hour at forecast origin
smart persistence	smart persistence approach with averaged k^*_{PV} over same preceding period as forecast horizon
without clear sky	persistence not calculated with clear sky model, P_{meas} at forecast origin adapted by combination
regional pers.	persistence calculated based on all sites' averages for P_{meas} and P_{clear}
smart regional pers.	smart persistence based on all sites' averages of P_{meas} and P_{clear}
input variation for persistence forecast (fig. A.4 right)	
pers $P_{clear}(T_{NWP})$	Persistence with P_{clear} based on NWP temperature forecast T_{NWP}
pers $P_{clear}(T_{clim})$	Persistence with P_{clear} based on climatology temperature T_{clim}
pers $P_{clear}(T_{clear})$	Persistence with P_{clear} based on clear sky temperature T_{clear} [106]
pers $P_{clear,fit}(T_{clim})$	Persistence with $P_{clear,fit}$ with fitted system parameters and T_{NWP}
input variation for combined forecast (fig. A.5)	
(pers,CMV,NWP)	Combination of persistence, CMV and DWD-ECMWF-combined forecasts
(pers,[CMV,NWP])	Combination of persistence and CMV-DWD-ECMWF-combined forecasts
(pers,CMV,NWP)+lr	same as (pers,CMV,NWP) with lr applied individually beforehand
(pers,NWP)	persistence and DWD-ECMWF-combined forecast without CMV forecasts

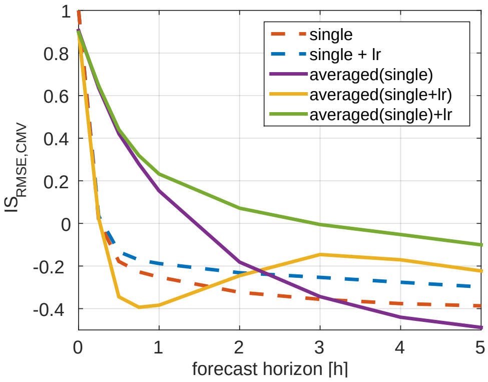

Figure A.3.: Improvement Score $IS(pers, CMV)$ referring to single site (dashed lines) and spatial averages (solid lines), in reference to CMV forecasts; Dataset: May–Nov 2013, 921 sites, 15 min resolution.

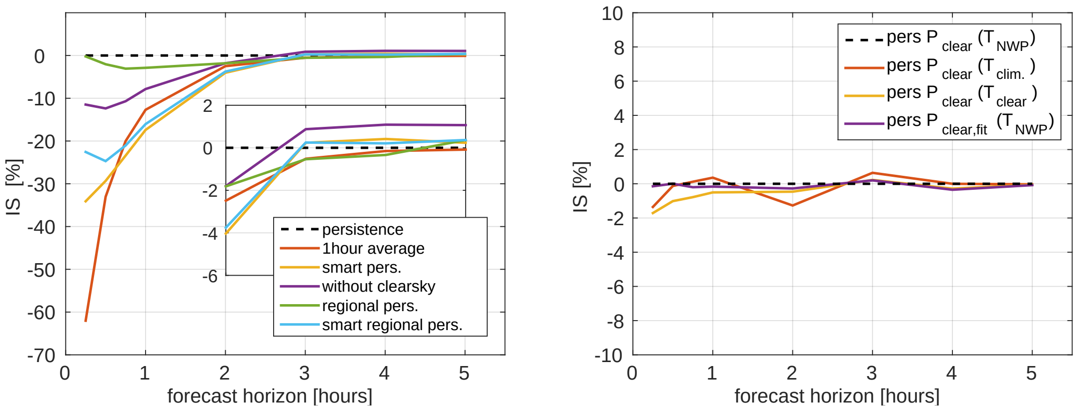

Figure A.4.: Variation of the persistence approach as included in the combined forecast regarding the persistence approach (left) and the ambient temperature impact in $P_{clearsky}$ (right), referring to table A.1 Displayed is the IS(combi,CMV) of the combined forecast with variations compared to the CMV forecast for forecast horizons from one to five hours ahead. Dataset: May–Nov 2013, 921 sites, 15 min resolution.

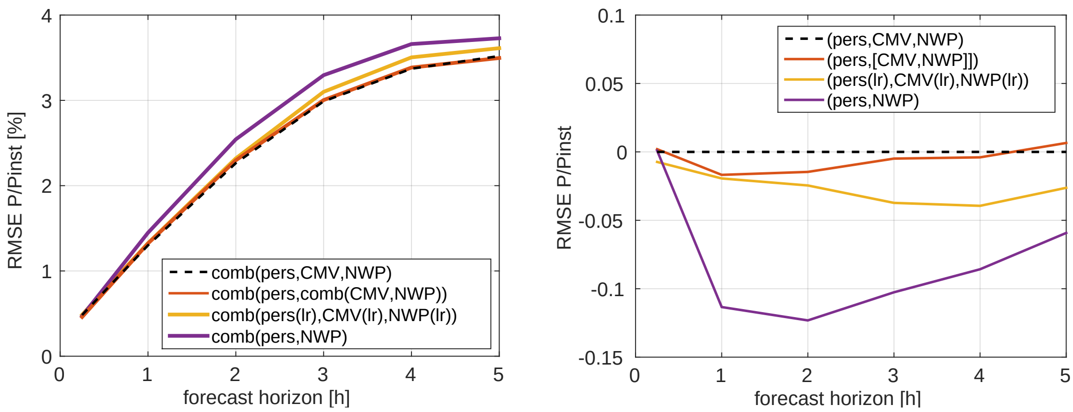

Figure A.5.: Different realizations of the combined forecast with respect to the input data (see table A.1), forecast rmse (left) and IS compared to the original combined forecast (right). Dataset: May–Nov 2013, 921 sites, 15 min resolution.

Erklärung

Hiermit erkläre ich, dass ich die vorliegende Dissertation selbstständig verfasst und nur die angegebenen Hilfsmittel benutzt habe. Die Dissertation hat weder in ihrer Gesamtheit noch in Teilen einer anderen Hochschule zur Begutachtung in einem Promotionsverfahren vorgelegen.

Oldenburg, 21. September 2015